2022

Kinematics and Preliminary FEMA P-695 Evaluation of the NewZ-BREAKSS Steel Boundary Frame with Buckling Restrained Brace Structural Fuses

Alexander M. Baker
Michigan Technological University, ambaker1@mtu.edu

KINEMATICS AND PRELIMINARY FEMA P-695 EVALUATION OF THE NEWZ-BREAKSS STEEL BOUNDARY FRAME WITH BUCKLING RESTRAINED BRACE STRUCTURAL FUSES

By

Alexander M. Baker

A THESIS

Submitted in partial fulfillment of the requirements for the degree of

MASTER OF SCIENCE

In Civil Engineering

MICHIGAN TECHNOLOGICAL UNIVERSITY

2022

This thesis has been approved in partial fulfillment of the requirements for the Degree of MASTER OF SCIENCE in Civil Engineering.

Department of Civil, Environmental, and Geospatial Engineering

Thesis Advisor:	*Dr. Daniel M. Dowden, PE, SE*
Committee Member:	*Dr. William M. Bulleit, PE*
Committee Member:	*Dr. R. Andrew Swartz, PE*
Department Chair:	*Dr. Audra Morse, PE, BCEE, F.ASCE*

Table of Contents

List of Figures

List of Tables

Acknowledgments

I would like to thank my family for supporting me in this journey. In specific, my dad for always believing in me, my mom for always showing me kindness, my younger sister for brightening my day and my older sister for always listening to me.

I also want to thank the community at Michigan Tech, which was my home away from home. At Michigan Tech, I met some amazing people who inspired me to be a better person, and also made some great memories along the way.

Abstract

Buckling Restrained Braced Frames (BRBFs) have become a popular seismic force resisting system (SFRS) due to their high ductility and energy dissipation. However, BRBFs are also susceptible to large residual drifts, which can make repair difficult. Efforts to reduce the residual drift of BRBFs typically involve special self-centering braces, or by using a dual system in tandem with the BRBF. This study proposes an alternative approach, in which a self-centering steel rocking frame is used as the boundary frame for the BRBF. The proposed system, called the NewZ-BREAKSS Buckling Restrained Braced Frame (NZ-BRBF) utilizes the recently proposed NewZ-BREAKSS (NZ) boundary frame to increase the post-yield stiffness of the system while concentrating all damage to the BRBs. The NZ-BRBF system is expected to behave similarly to conventional BRBF, but with smaller residual drifts and a boundary frame that remains essentially elastic, simplifying repair. This study presents a numerical investigation of the proposed low-damage SFRS, using the FEMA P-695 methodology as a guiding framework. The results suggest that the NZ-BRBF can exhibit better performance than conventional BRBFs and can be designed with the same response modification factor (R factor) as conventional BRBFs.

Chapter 1

Introduction

This study presents the results of a numerical investigation into a newly proposed seismic-force resisting system (SFRS), the NewZ-BREAKSS Buckling Restrained Braced Frame (NZ-BRBF). The NZ-BRBF system is a type of Buckling Restrained Braced Frame (BRBF) with a boundary frame detailed such that damage is concentrated in the Buckling Restrained Braces (BRBs). The results presented in this study suggest that the NZ-BRBF system can be designed for a seismic response modification factor (R factor) of 8, same as BRBFs, and that the detailing of the NZ-BRBF boundary frame can help to reduce residual deformations and increase the repairability of the system after a design-level event.

1.1 Motivation

Modern building codes require that seismic-force resisting systems (SFRSs) be designed for life-safety for typical buildings. Designing only to the performance objective of life-safety, however, can lead to severe structural damage after a design level event,

likely requiring demolition of the building. This design paradigm has left urbanized regions vulnerable to significant economic and socio-economic losses. Alternatively, a new design paradigm in which SFRSs are designed to be low-damage and easily repaired could facilitate rapid recovery. Low-damage SFRSs are typically comprised of self-centering systems that isolate energy dissipation to replaceable elements (i.e. structural fuses) and typically provide frame self-centering through post-tensioned (PT) rocking joint details. Towards this alternative design paradigm, this research investigates the newly proposed NZ-BRBF system, which, while not self-centering, utilizes a post-tensioned low-damage boundary frame to reduce residual drift.

1.2 Proposed System

The NZ-BRBF system provides resistance and ductility through buckling-restrained braces (BRBs), and provides resilience and repairability through utilizing the recently proposed NewZ-BREAKSS boundary frame [1]. NewZ-BREAKSS stands for "**New Z**ealand-inspired-**B**uffalo **R**esilient **E**arthquake-resistant **A**uto-centering while **K**eeping **S**lab **S**ound", and for brevity will be referred to as the NZ boundary frame. A schematic of the proposed SFRS, with a "Lightning-Bolt" (LB) brace configuration, is presented in Figure 1.1. For the condition shown in the figure, the post-tensioning (PT) elements are located at the horizontal boundary element (HBE) centroid with anchorages at the column and at 1/3 points along the beam span.

In this configuration, all structural damage is designed to be concentrated in the BRBs; the NZ rocking joint detail provides damage-free boundary frame stiffness, and the column hinge at the first floor midpoint prevents the formation of a plastic hinge at the column base. The column hinge is located at the midpoint of the first floor rather than the base of the column to mitigate potential soft-story effects arising from a pinned column base detail. Additionally, the BRBs are connected to the frame with

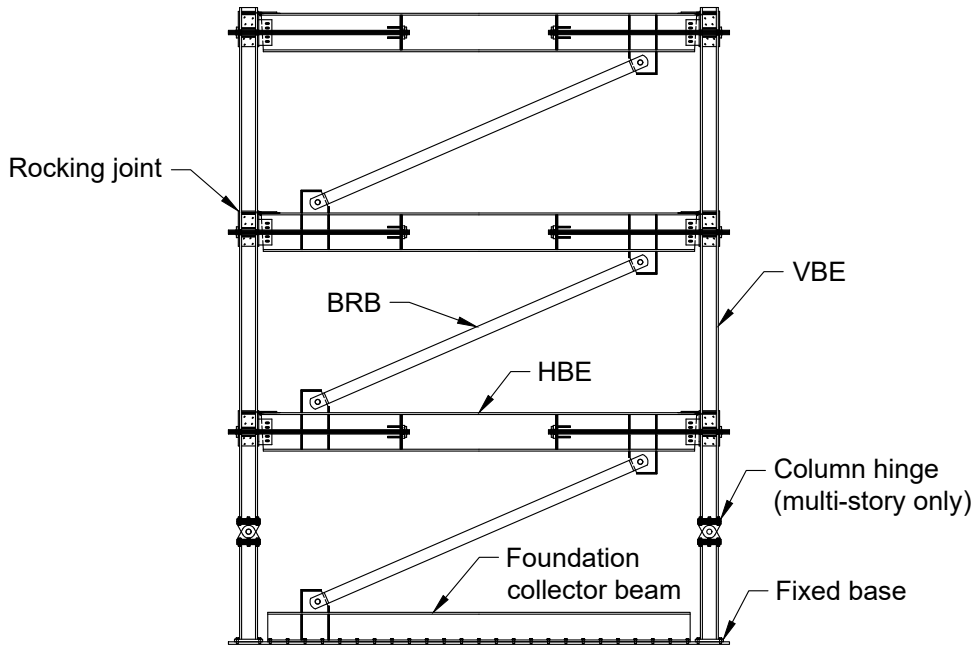

Figure 1.1: Elevation schematic of 3-story NZ-BRBF system with Lightning-Bolt (LB) brace configuration

pinned connections separate from the beam-column joint, accommodating rocking joint gap opening and closing. See Figure 1.2 for connection details.

The top-flange rocking joint detail accommodates large drifts while maintaining the same center-to-center distance between columns, keeping the floor slab sound. This differs from other rocking joints, such as flange rocking joints, where the beam rocks about both the top and bottom flanges, leading to "beam growth", where the distance between columns increases with story drift [2]. See Figure 1.3 for illustration of a 4% drift condition.

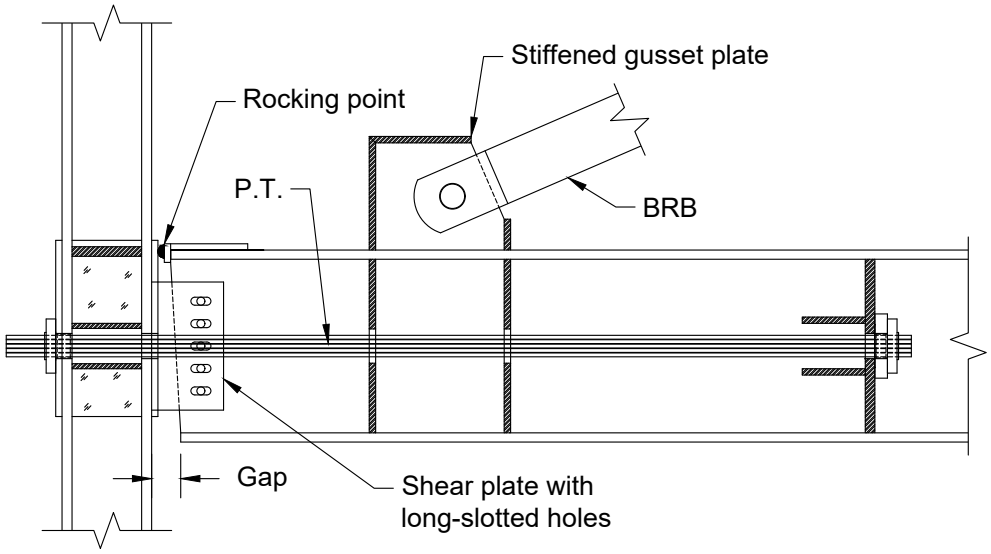

Figure 1.2: NZ-BRBF beam-column connection

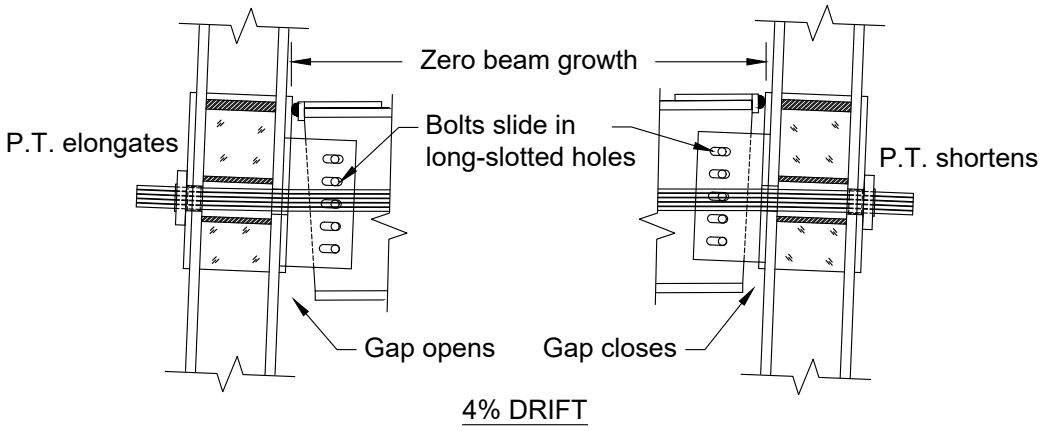

Figure 1.3: Drift detail

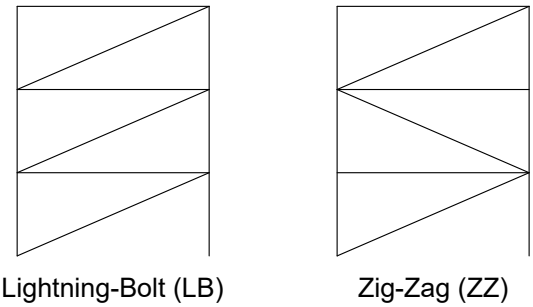

Figure 1.4: NZ-BRBF brace configurations

The NZ-BRBF system was investigated for the LB brace configuration and an alternative "Zig-Zag" (ZZ) configuration, where brace orientation alternates at every other floor, as illustrated in Figure 1.4.

1.3 Methodology

This study follows the methodology outlined in the *"Quantification of Building Seismic Performance"*, FEMA P-695, hereafter referred to as the P-695 [3]. The P-695 methodology is a quantitative, statistical approach to what has otherwise been an arbitrary process of determining ASCE 7 seismic performance factors (SPFs) for seismic-force resisting systems (SFRSs). This methodology can be used both to check existing SFRSs [4], [5] and to evaluate proposed systems [6], thus hastening validation and adoption of new SFRSs.

Validating a new system using the P-695 methodology is a rigorous, peer-reviewed process, comprised of archetype development, nonlinear model development, nonlinear analysis, and performance evaluation. For archetype development, a range of building configurations representing the design space of the system must be developed. The design space includes ranges in structural configuration, gravity loading,

seismic loads, and fundamental period (building heights). Archetype buildings must then be designed in accordance with applicable design standards, assuming trial SPFs. Once archetypes are designed, nonlinear models must be developed representing the median behavior of the designed structures. Failure modes must be accounted for in the numerical models, either directly simulated or indirectly accounted for by non-simulated collapse conditions. Collapse evaluation of the nonlinear models is then compared to acceptance criteria. Acceptance criteria are based off of structural fragility curves, adjusted for uncertainties, and a target conditional probability of collapse at the Maximum Considered Earthquake (MCE) intensity. If the system does not meet acceptance criteria, new trial SPFs are selected. Then, the process repeats until acceptable SPFs are validated.

This research loosely follows the P-695 methodology, with a limited archetype design space, limited test data and peer-review. To reflect the limitations of the study, penalties are imposed on performance evaluation. Therefore, this study should be regarded as preliminary results showing promise of the NZ-BRBF system and insight into its seismic behavior, but not validation of the system. Further study, especially experimental studies, would have to be conducted to fully validate the system.

1.4 Research objectives

The objectives of this research are as follows:

1. Characterize the mechanical behavior of the NZ-BRBF system through development of simple mathematical equations.
2. Create numerical models that accurately represent the kinematics of the NZ-BRBF system.

3. Establish design requirements for the NZ-BRBF system and design a set of index archetype models that represent a wide range of possible design configurations.

4. Quantify the seismic performance of the NZ-BRBF system through nonlinear static and dynamic analyses.

5. Assess the collapse performance of the NZ-BRBF system by conducting Incremental Dynamic Analyses.

6. Establish preliminary seismic performance factors for the NZ-BRBF system in accordance with the P-695 methodology.

1.5 Thesis organization

The organization of the remaining chapters in this thesis are as follows:

- Chapter 2 reviews the relevant literature on BRBs and self-centering systems.
- Chapter 3 defines the kinematics of the proposed system.
- Chapter 4 describes the development and design of the index archetype buildings.
- Chapter 5 describes the nonlinear modeling details of the index archetype models.
- Chapter 6 presents the results of nonlinear static (pushover) analyses.
- Chapter 7 presents the ground motion suite used for nonlinear dynamic analyses, and the system responses at design-basis and maximum considered earthquake intensities.

- Chapter 8 presents the methodology and results of the Incremental Dynamic Analyses conducted for collapse assessment.
- Chapter 9 presents the P-695 performance evaluation of the proposed system.
- Chapter 10 summarizes the results and discusses the findings.

Chapter 2

Background

This chapter reviews the literature on Buckling Restrained Braced Frames (BRBFs), efforts to reduce their residual drift response at both local and global levels, and the NewZ-BREAKSS (NZ) boundary frame.

2.1 Buckling Restrained Braced Frames

Buckling Restrained Braced Frames (BRBFs) are a special type of Concentrically Braced Frame (CBF) which utilize Buckling Restrained Braces (BRBs) in place of conventional braces. In contrast to conventional braces, which have asymmetric hysteretic response and buckle in compression, BRBs are capable of developing stable hysteresis loops, yielding nearly symmetrically in both tension and compression, without buckling [7]. This is typically accomplished by restraining the yielding core of the brace by encasing it in an an unbonded concrete sleeve, as shown in Figure 2.1.

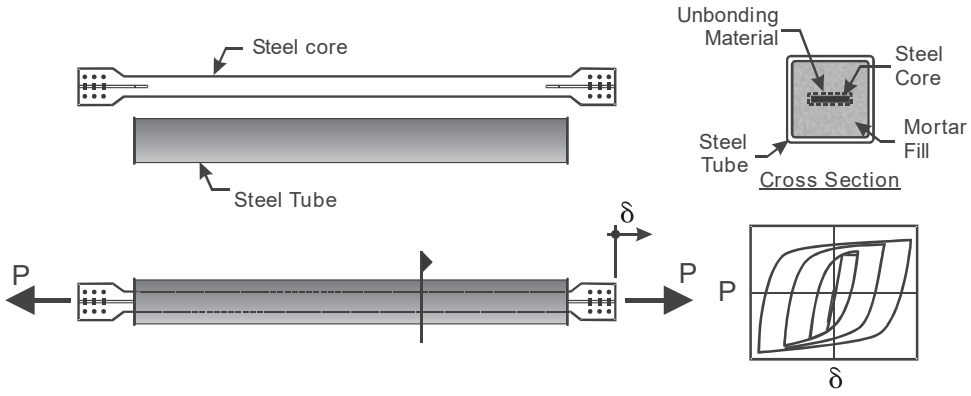

Figure 2.1: Schematic of a buckling restrained brace (BRB) [8]

Early studies with BRBs and BRBFs demonstrated that BRBFs exhibit better seismic performance than than conventional CBFs [9], [10]. Because of this, since their introduction, BRBs have grown in popularity, first codified for structural use in the USA in 2005, with provisions added to ASCE-7 & AISC 341 [11], [12]. However, because they dissipate energy through large yielding hysteresis loops, BRBFs do not exhibit self-centering properties, and have been shown to be susceptible to large residual drifts, similar to comparable Special Moment Resisting Frames (SMRFs) [13]. How large is too large? A study done on the repair of structures after the Hyogoken-Nanbu earthquake in Japan suggested a economic repairability limit of 0.5% roof and 1.0% inter-story residual drift [14]. Additionally, there are other factors, such as safety and construction tolerances, that have led to a proposed permissible drift level of 0.5%, or 0.005 rad [15]. Because ordinary BRBFs often exceed residual drift levels of 0.5%, numerous methods have been proposed to reduce or eliminate the residual drift response of BRBFs.

2.1.1 Efforts to Reduce Residual Drift

In general, there have been two approaches utilized to reduce the residual drift response of BRBFs. The first approach is to modify the brace itself to achieve better

performance, typically through use of post-tensioning rods configured such that they are engaged in both tension and compression of the brace. The second approach is to add a secondary system that increases the post-yield stiffness of the system and therefore reduces the residual drift responses. The NZ-BRBF system utilizes this second approach, with the NZ boundary frame providing secondary elastic stiffness.

2.1.1.1 Self-Centering Buckling Restrained Braces

One common approach to reduce the residual drift response of BRBFs is to utilize special self-centering BRBs as proposed by Christopoulos et al. 2008 [16]. This approach utilizes post-tensioning rods attached to the brace in a specific configuration that engages the post-tensioning when the brace is in tension and compression, as shown in Figure 2.2.

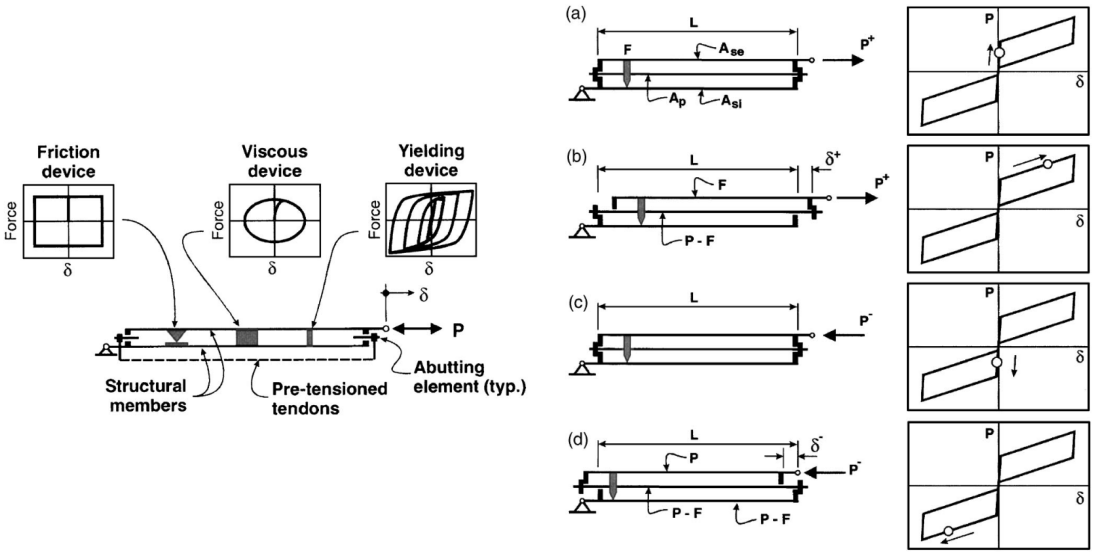

Figure 2.2: Schematic and mechanics of generalized self-centering energy dissipative brace (SCED) [16]

This concept was also employed by Eatherton et al. 2014, fitting a BRB with with pretensioned shape memory alloy (SMA) rods designed to nearly eliminate the residual deformation of the brace, as shown in Figure 2.3.

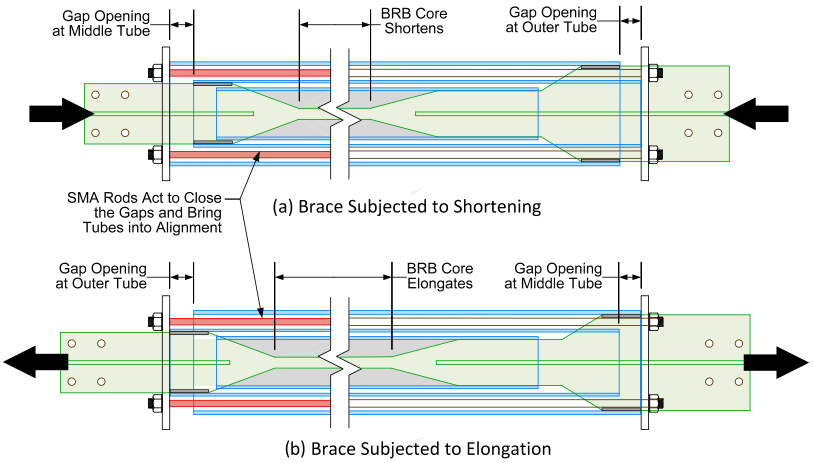

Figure 2.3: Schematic of self-centering buckling restrained brace (SC-BRB) [17]

Similarly, Atasever et al. 2020 proposed a special BRB with externally post-tensioned carbon fiber composite cables, as shown in Figure 2.4, with experimental results demonstrating its effectiveness in reducing residual drift response.

Another similar brace was proposed by Xie et al. 2020, additionally incorporating a friction fuse to prevent fracture of the post-tensioned carbon fiber composite cables, increasing its maximum deformation while sacrificing some of its self-centering capability.

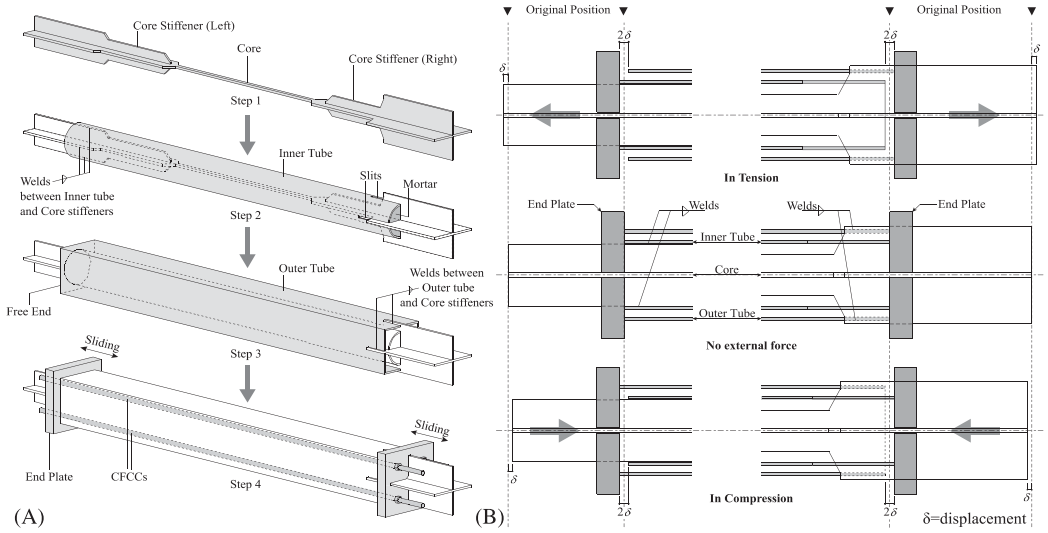

Figure 2.4: Schematic of externally post-tensioned buckling restrained brace (PT-BRB) [18]

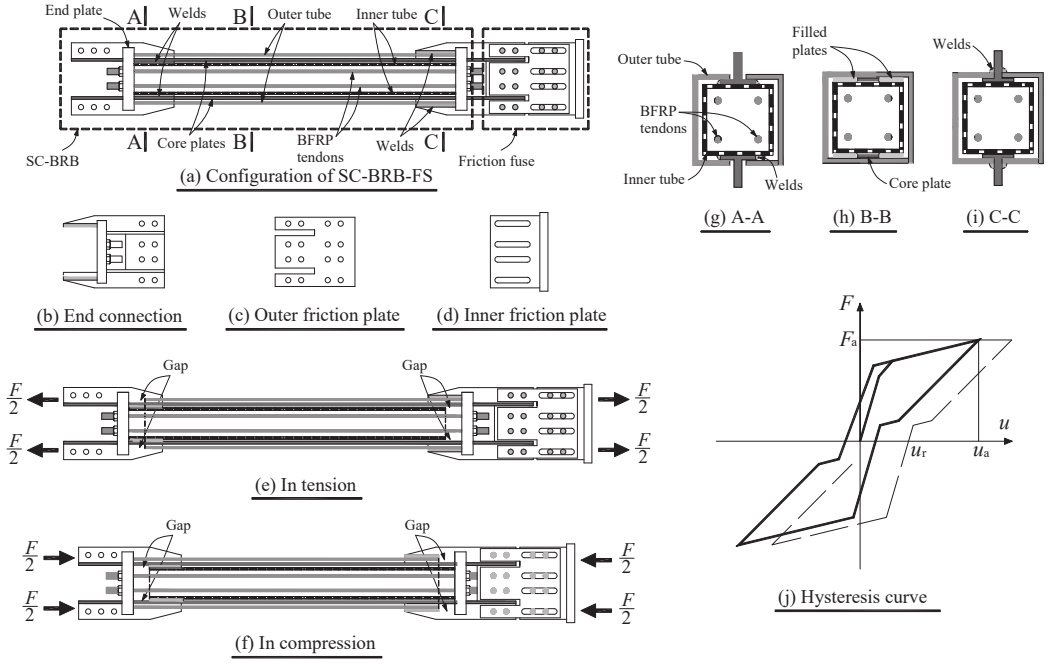

Figure 2.5: Schematic of self-centering buckling-restrained brace with friction fuse (SC-BRB-FS) [19]

2.1.1.2 BRBF Combined with Secondary System

Another common approach that has been studied for reducing residual drift of BRBFs is to utilize a secondary system in parallel with the BRBF to increase its post-yield stiffness. The benefit of this approach over using self-centering BRBs is that it can be easily implemented with conventional structural components.

As an example of the effectiveness of this approach, Kiggens and Uang 2006 combined a BRBF system with a SMRF in parallel, and effectively reduced the residual interstory drift, as shown in Figure 2.6.

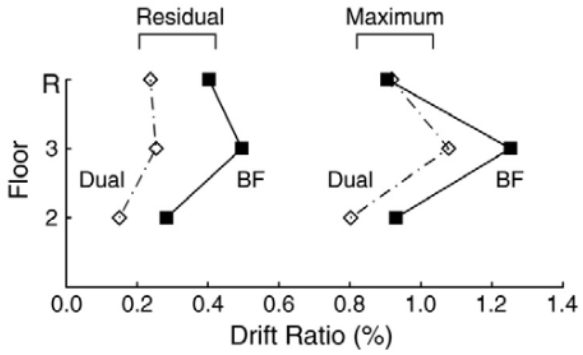

(a) 3-story frames.

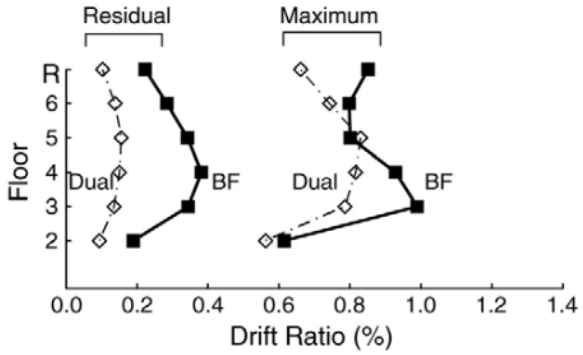

(b) 6-story frames.

Figure 2.6: Peak and residual drift profiles, comparing BRBF alone (BF) with a dual BRBF-SMRF frame [20]

Another study combined a self-centering concentrically braced frame (SCCBF) in parallel with a BRBF, and similarly found that the residual drift response was significantly reduced.

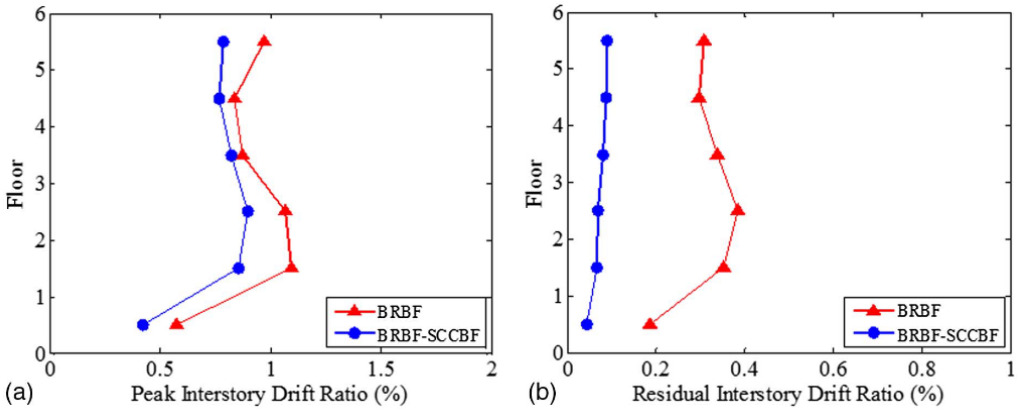

Figure 2.7: Peak and residual drift profiles, comparing BRBF alone with a dual BRBF-SCBRBF frame [21]

2.2 Post-Tensioned Steel Rocking Frames

The NZ-BRBF system utilizes the NewZ-BREAKSS (NZ) boundary frame, a type of post-tensioned steel rocking frame proposed by Dowden and Bruneau 2011 [2], to provide secondary elastic stiffness, which is expected to reduce the residual drift response of the system. The NZ boundary frame is a special type of post-tensioned steel rocking connection, which is an alternative connection detail to conventional moment resisting connections. Post-tensioned steel rocking connections were first developed as a solution to the problem that traditional moment resisting connections had low plastic rotation capacity and were susceptible to failure [22].

One of the first post-tensioned steel rocking connections was proposed by Christopoulos et al. 2002: the post-tensioned energy dissipating (PTED) steel connection [22]. The PTED is a beam-column connection detailed such that the beam is allowed to

rock about its top and bottom flanges. This rocking behavior causes "beam growth" that engages post-tensioning cables anchored at both ends of the boundary frame. In addition, small yielding elements at the top and bottom beam flanges yield in tension and compression, providing energy dissipation. The resulting hysteresis of the post-tensioning response and the yielding element response is flag-shaped, providing energy dissipation with no residual drift. A schematic of the PTED system is shown in Figure 2.8.

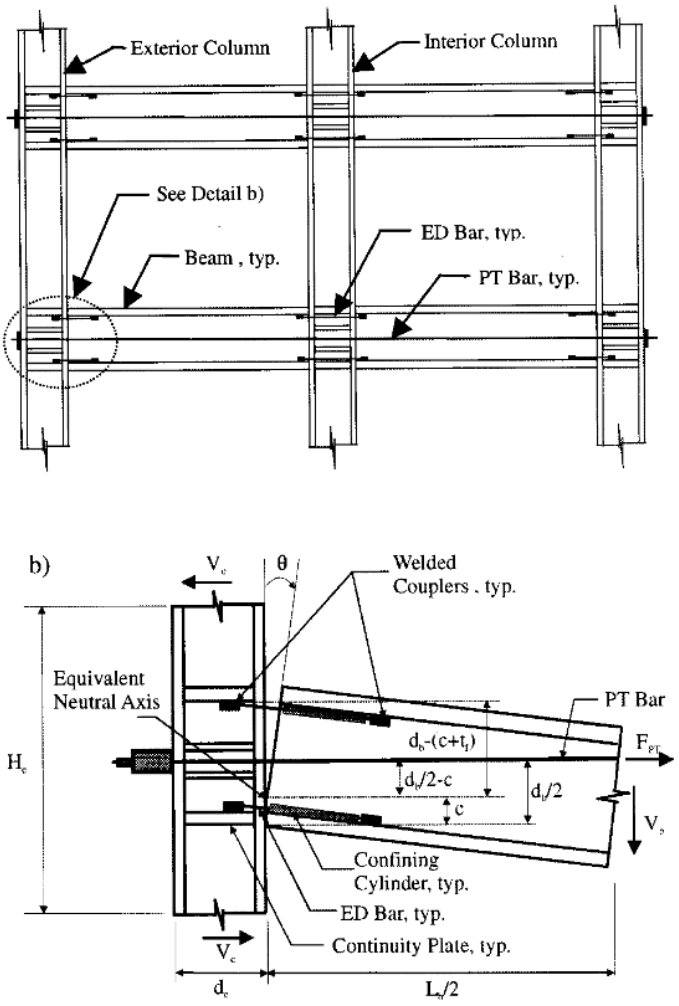

Figure 2.8: Schematic of post-tensioned energy dissipating (PTED) steel connection [22]

However, this "beam growth" can cause damage to the floor diaphragm, which is counter-productive to the goal of seismic resiliency. This problem was the motivation behind development of the NZ boundary frame, which rocks only about the top-flange of the beam, resulting in effectively zero beam growth. In order to engage the post-tensioning in this configuration, two separate post-tensioning elements are required, anchored independently on the beam, as shown in Figure 2.9.

The resulting system exhibits low-damage self-centering behavior without beam growth, and was validated experimentally with Self-Centering Steel Plate Shear Walls (SC-SPSWs) by Dowden et al. 2016. Experimental results on the SC-SPSWs established that the boundary frame remained essentially elastic and the residual drift of the system was less than the 0.5% limit at the MCE level intensity [23].

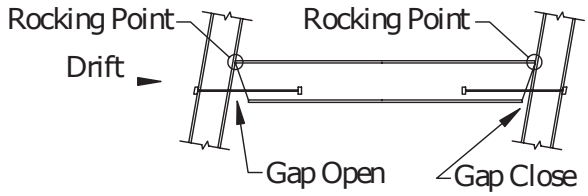

Figure 2.9: Schematic of NewZ-BREAKSS (NZ) steel connection [1]

2.3 Summary of Relevant Research

Since their introduction, Buckling Restrained Braces (BRBs) have been increasingly used in seismic applications for their substantial energy dissipation in tension and compression. Buckling Restrained Braced Frames (BRBFs), have been shown to have better seismic performance than conventional Concentrically Braced Frames (CBFs). However, while BRBFs have excellent energy dissipation, they have low post-yield stiffness, and are susceptible to large residual drifts, similar to Special Moment Resisting Frames (SMRFs).

Two main methods have been proposed to reduce or eliminate the residual drift of BRBF systems. One method is to modify the BRBs directly, adding post-tensioning in a configuration that increases the post-yield stiffness of the brace. The other method is to externally increase the post-yield stiffness of the system through the use of a secondary system. Both methods have been shown to be effective in reducing residual drifts.

This study focuses on externally increasing the post-yield stiffness of the system, through use of the NewZ-BREAKSS (NZ) boundary frame. The NZ boundary frame is a type of post-tensioned steel rocking frame, developed as an alternative to conventional welded moment connections. Studies have shown that the NZ boundary frame is effective in reducing residual drift of Steel Plate Shear Walls (SPSWs), while remaining essentially elastic. While BRBFs are not the same system as SPSWs, it is expected, based on the literature, that incorporating it in parallel with BRBs will reduce the overall residual drift response.

Chapter 3

Kinematics of NZ-BRBFs

The NZ-BRBF system acts like a dual system, with BRBs acting as the main energy dissipating seismic-force resisting elements, and the NZ boundary frame providing elastic secondary stiffness and damage free-detailing. Combined, the system is expected to behave similarly to conventional BRB frames, but with smaller residual drifts and increased repairability. This benefit of using the NZ boundary frame was previously demonstrated by work on self-centering steel plate shear walls (SC-SPSWs) [23].

This chapter presents analytical equations characterizing the kinematics of both components of the NZ-BRBF system, as well as development of axial, shear, and moment diagrams for the horizontal boundary frame elements. Some of the dimensions and variables used in this chapter are illustrated in Figure 3.1.

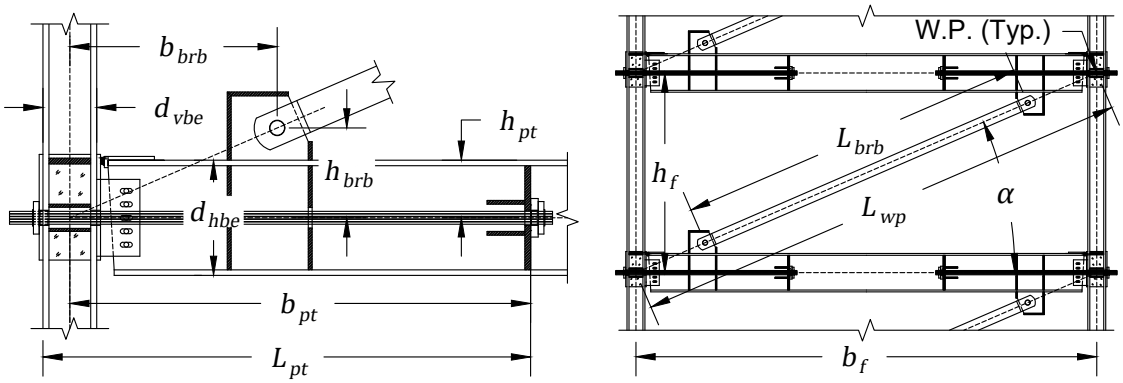

(a) Rocking joint (b) Brace and bay

Figure 3.1: NZ-BRBF dimensions (LB configuration)

where,

b_{brb}	=	Horizontal offset to BRB connection
b_f	=	Frame bay width
b_{pt}	=	Horizontal offset to PT anchor
d_{vbe}	=	Depth of vertical boundary element (VBE)
d_{hbe}	=	Depth of horizontal boundary element (HBE)
h_{brb}	=	Vertical offset to BRB connection
h_f	=	Frame story height
h_{pt}	=	Vertical offset from top flange of HBE to PT
L_{brb}	=	Length of the BRB, from pin to pin.
L_{pt}	=	PT length
L_{wp}	=	Diagonal length from workpoint to workpoint.
	=	$\sqrt{{h_f}^2 + {b_f}^2}$
α	=	Brace angle from the horizontal
	=	$\tan^{-1}(h_f/b_f)$
W.P.	=	Work point (intersection of HBE & VBE centerlines)

3.1 Buckling Restrained Brace (BRB)

The NZ-BRBF system utilizes buckling restrained braces (BRBs) as its primary seismic force resisting component. A free-body diagram of the equivalent seismic forces acting on the frame and the yielding mechanism of the BRBs is shown in Figure 3.2.

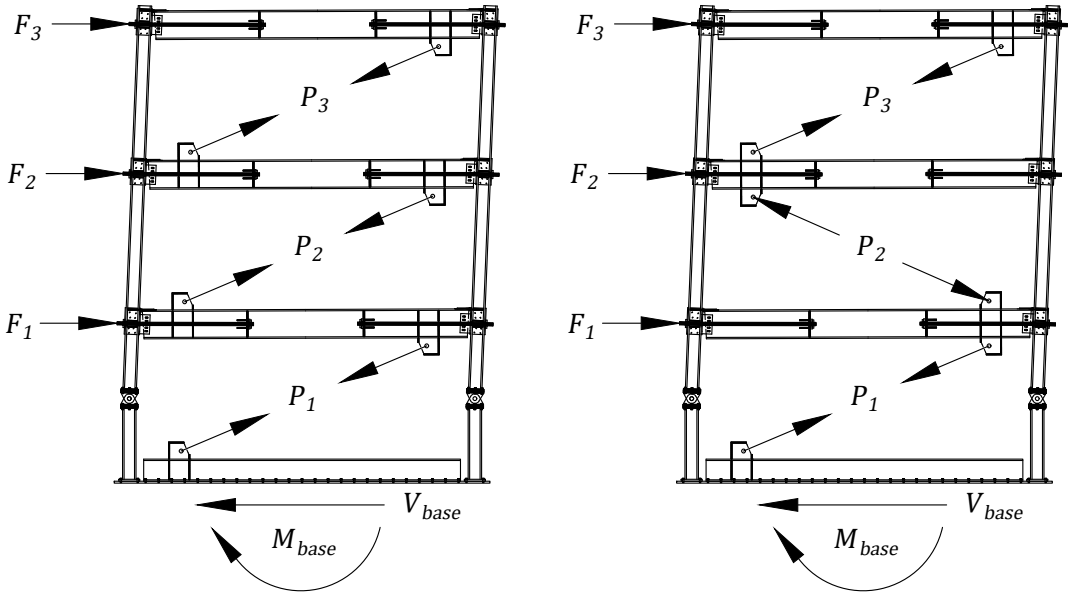

(a) LB configuration (b) ZZ configuration

Figure 3.2: NZ-BRBF yielding mechanism

where,

F_i	=	Equivalent lateral force acting at level i
P_i	=	BRB axial force at floor i
V_{base}	=	Base shear
M_{base}	=	Overturning resisting moment at base

The benefit to using BRBs as the inelastic energy dissipation element in the NZ-BRBF system is that BRBs exhibit stable hysteresis and substantial energy dissipation in

both tension and compression. This property of BRBs is achieved by utilizing a reduced-section yielding core, which is braced against buckling, often through use of a restraining steel tube filled with concrete fill. However, because BRBs are a manufactured structural element, detailing can vary between manufacturers [24]. This complex and uncertain geometry of BRBs can be a challenge for modeling and analysis. Therefore, generalized equations were developed for this study which characterize a wide range of BRB geometries.

For this study, typical BRB geometry was assumed, shown in Figure 3.3. The typical BRBs has three zones: the restrained yielding core, the stiffened connections and the transition zone between the core and connections. The stiffened connections are assumed to behave elastically, and the transition zones are assumed to remain essentially elastic. However, in lieu of specific detailing from a manufacturer, and

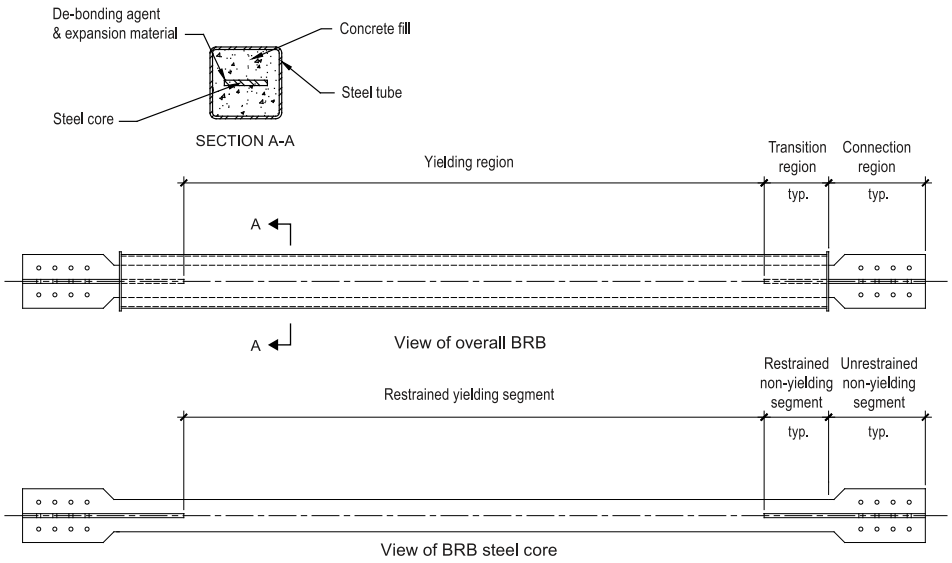

Figure 3.3: Common BRB assembly [25]

to simplify analytical and numerical modeling, the connection and transition zones were lumped into one linear-elastic end-zone (this combined end zone must have an effective area larger than the yielding core area in order to maintain the linear-elastic

assumption). The simplified representation of the brace, with yielding core and elastic end zones labeled, is shown in Figure 3.4.

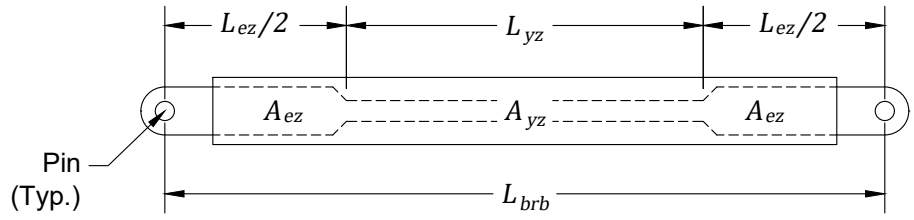

Figure 3.4: Simplified representation of a BRB

where,

A_{yz} = Cross-sectional area of yielding zone/core.

L_{yz} = Length of the yielding zone/core.

A_{ez} = Cross-sectional area of the elastic zone of the brace.

L_{ez} = Total length of the elastic zones of the brace.

= $L_{brb} - L_{yz}$

3.1.1 Effective Prismatic Truss

Because BRBs are non-prismatic, numerical modeling is typically done by either using actual dimensions and material properties, applied to multiple elements representing the different zones, or by using one prismatic truss element with effective dimensions and material properties that capture the response of the brace. For simplicity in modeling and analysis, the effective prismatic truss is desirable, and therefore was used in this study.

3.1.1.1 Effective Stiffness and Area

In order to determine the stiffness of the BRBs required for the effective prismatic truss, the braces were idealized as springs in series, as is shown in Figure 3.5. Individual spring stiffnesses are shown in Eqs. (3.1-1) & (3.1-2), where E_{brb} is the elastic modulus of the BRB material.

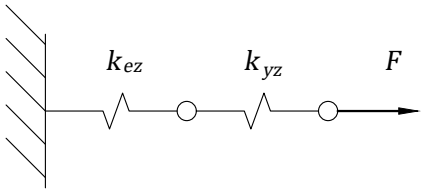

Figure 3.5: Springs in series

$$k_{yz} = \frac{A_{yz}E_{brb}}{L_{yz}} \tag{3.1-1}$$

$$k_{ez} = \frac{A_{ez}E_{brb}}{L_{ez}} \tag{3.1-2}$$

Accordingly, the stiffness of the brace, k_{brb}, can then be determined using the equation for the stiffness of springs in series as shown in Eq. (3.1-3).

$$k_{brb} = \frac{1}{\frac{1}{k_{yz}} + \frac{1}{k_{ez}}} \tag{3.1-3}$$

In order to model this stiffness in a single truss element extending from pin-to-pin, the area and/or the elastic modulus must be modified. For this study, the elastic modulus was kept constant, and an effective area was determined. The effective area,

A^*_{brb}, required to achieve the same stiffness is presented in Eq. (3.1-4), where L_{brb} is as defined in Figure 3.4:

$$A^*_{brb} = \frac{k_{brb} L_{brb}}{E_{brb}} \tag{3.1-4}$$

3.1.1.2 Stiffness Modification Factor and Detailing Ratios

Because the end elastic zone areas are assumed to be larger than the yielding zone core areas, the effective area, A^*_{brb}, of the brace will also be larger than the core area. Additionally, assuming a rigid boundary frame from the BRB pin connections to the frame workpoints, the effective prismatic truss stiffness will be larger than if the yielding core area was extended to the workpoints. The ratio between the brace stiffness and the stiffness of the core extended to the workpoints is a common measure of the relative stiffness of a BRB [25]. This ratio, hereafter referred to as the stiffness modification factor, f_{SM}, is defined in Eq. (3.1-5)

$$f_{SM} = k_{brb} \Big/ \frac{A_{yz} E_{brb}}{L_{wp}} \tag{3.1-5}$$

Substituting Eq. (3.1-3) into Eq. (3.1-5) and simplifying, the stiffness modification factor can be expressed solely in terms of the BRB geometry.

$$f_{SM} = \frac{1}{\dfrac{L_{yz}}{L_{wp}} + \dfrac{A_{yz} L_{ez}}{A_{ez} L_{wp}}} \tag{3.1-6}$$

For further simplification of Eq. (3.1-5), and referencing Figures 3.1 & 3.4, three detailing ratios can be defined: the ratio of yielding to elastic zone area, λ_A, the ratio

of brace length to work-point length, λ_B, and the ratio of yielding core length to brace length, λ_C.

$$\lambda_A = A_{yz}/A_{ez} \tag{3.1-7}$$

$$\lambda_B = L_{brb}/L_{wp} \tag{3.1-8}$$

$$\lambda_C = L_{yz}/L_{brb} \tag{3.1-9}$$

With these relationships defined, f_{SM} can be expressed solely in terms of dimensionless detailing ratios, as shown in Eq. (3.1-10).

$$f_{SM} = \frac{1}{\lambda_A\lambda_B + \lambda_B\lambda_C - \lambda_A\lambda_B\lambda_C} \tag{3.1-10}$$

Additionally, using the stiffness modification factor and detailing ratios presented above, Eq. (3.1-4) for effective area of the truss can be re-written to be in terms of the yielding core area, A_{yz}, the stiffness modification factor, f_{SM}, and the brace length ratio, λ_B, as shown in Eq. (3.1-11).

$$A^*_{brb} = (f_{SM}\lambda_B)A_{yz} \tag{3.1-11}$$

3.1.1.3 Effective Yield Point and Stress Conversion

Using the effective brace area, A^*_{brb}, the elastic response of the effective truss will match that of the actual brace. However, in order to maintain the same yield force, P_y, an effective yield stress, σ^*_y, rather than the yield stress of the core material, σ_y,

must be used. Equating axial force of the yielding core to that of the effective truss at the yield point condition, an expression for effective yield stress can be obtained.

$$P_y = \begin{cases} \sigma_y A_{yz} & \text{(Yielding Core)} \\ \sigma_y^* A_{brb}^* & \text{(Effective Truss)} \end{cases} \tag{3.1-12}$$

Substituting Eq. (3.1-11) for A_{brb}^* into Eq. (3.1-12) , the effective yield stress can be expressed in terms of the yield stress of the core material, the stiffness ratio, and the brace length ratio, leading to Eq. (3.1-13).

$$\sigma_y^* = \frac{\sigma_y}{f_{SM}\lambda_B} \tag{3.1-13}$$

Additionally, the effective yield strain is as follows, where ε_y is the yield strain of the yielding core material.

$$\varepsilon_y^* = \frac{\sigma_y^*}{E_{brb}} = \frac{\varepsilon_y}{f_{SM}\lambda_B} \tag{3.1-14}$$

Using the effective yield stress σ_y^* and yield strain ε_y^*, the effective truss will not only represent the elastic BRB behavior, but will also capture the yield point of the actual brace. Additionally, because the components of the BRB are in series, the stress conversion in Eq. (3.1-13) is valid for all stress values, not just the yield stress. Accordingly, re-expressing Eq. (3.1-13) for any stress, the component axial stress, σ_{brb}^*, can be converted to yielding zone stress, σ_{yz}, with equation Eq. (3.1-15).

$$\sigma_{yz} = (f_{SM}\lambda_B)\sigma_{brb}^* \tag{3.1-15}$$

In addition to converting stresses, it is also of interest to convert effective truss model strains to yielding core strains. However, unlike the generalization of the stress conversion in Eq. (3.1-15), the strain conversion in Eq. (3.1-14) cannot be applied to all strain values. This is due to the concentration of plastic strain in the yielding core.

Therefore, relationships between effective truss model strain and yielding core strain were developed for both elastic and plastic strains and are addressed subsequently.

3.1.1.4 Elastic and Plastic Strain Conversion

Assuming elastic-plastic with kinematic strain hardening behavior in the BRB, the elongation of the brace and its individual regions can be separated into their elastic and plastic components, as shown in Figure 3.6.

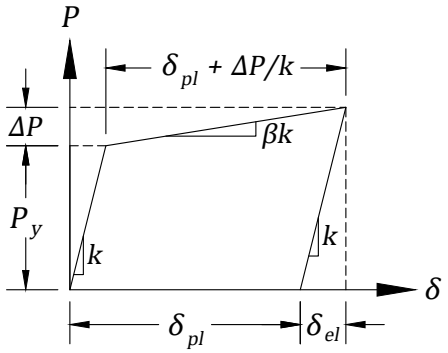

Figure 3.6: Components of brace elongation

where,

δ	=	Total elongation.
	=	$\delta_{el} + \delta_{pl}$
δ_{el}	=	Elastic elongation.
δ_{pl}	=	Plastic elongation.
P	=	Axial force.
P_y	=	Axial force at yield.
ΔP	=	Axial force increment due to strain hardening.
β	=	Strain hardening ratio.
k	=	Elastic stiffness.

Because the axial force in the brace is the same in all parts of the brace, the yielding core and brace (i.e., effective truss) elastic elongations are proportional to each other, as is shown in Eq. (3.1-16).

$$P = \begin{cases} k_{yz}(\delta_{yz})_{el} & \text{(Yielding Core)} \\ k_{brb}(\delta_{brb})_{el} & \text{(Effective Truss)} \end{cases} \tag{3.1-16}$$

The elastic strains of the yielding core and effective truss can then be determined by dividing by the yielding core and brace lengths, respectively.

$$(\varepsilon_{yz})_{el} = (\delta_{yz})_{el}/L_{yz} \tag{3.1-17}$$

$$(\varepsilon^*_{brb})_{el} = (\delta_{brb})_{el}/L_{brb} \tag{3.1-18}$$

Combining Eqs. (3.1-16), (3.1-17) & (3.1-18), a conversion between effective truss and yielding core elastic strains, shown in Eq. (3.1-19), can be obtained.

$$(\varepsilon_{yz})_{el} = \frac{k_{brb}L_{brb}}{k_{yz}L_{yz}}(\varepsilon^*_{brb})_{el} \tag{3.1-19}$$

Substituting in expressions for k_{brb} and k_{yz} from Eqs. (3.1-5) & (3.1-1), Eq. (3.1-19) can be simplified as shown in Eq. (3.1-20). Note the similarity to Eq. (3.1-15).

$$(\varepsilon_{yz})_{el} = f_{SM}\lambda_B(\varepsilon^*_{brb})_{el} \tag{3.1-20}$$

While the elastic strains of the brace and core are related by axial force, the plastic strains are related by plastic elongation, which is concentrated in the yielding core, due to the design of the BRBs. Therefore, the plastic elongation of the brace, $(\delta_{brb})_{pl}$, is equivalent to the plastic elongation of the yielding core $(\delta_{yz})_{pl}$. So, because the yielding core is shorter than the BRB brace, the plastic core strain will be larger than

the effective plastic strain of the brace.

$$(\delta_{brb})_{pl} = \begin{cases} (\varepsilon_{yz})_{pl} L_{yz} & \text{(Yielding Core)} \\ (\varepsilon^*_{brb})_{pl} L_{brb} & \text{(Effective Truss)} \end{cases} \tag{3.1-21}$$

Equating the yielding core and effective truss cases in Eq. (3.1-21) and substituting in Eq. (3.1-9), a conversion between plastic strains, shown in Eq. (3.1-22), can be obtained. This conversion is useful for understanding how detailing ratios can affect the fatigue life of a BRB; smaller yield length ratios, λ_C, cause higher core plastic strain demands.

$$(\varepsilon_{yz})_{pl} = \frac{(\varepsilon^*_{brb})_{pl}}{\lambda_C} \tag{3.1-22}$$

Finally, because strain is the sum of elastic and plastic strains, Eqs. (3.1-20) & (3.1-22) can be combined to obtain a conversion from effective truss stress and strain to yielding core strain as is shown in Eq. (3.1-23).

$$\varepsilon_{yz} = \overbrace{f_{SM}\lambda_B \frac{\sigma^*_{brb}}{E_{brb}}}^{\text{Elastic}} + \overbrace{\frac{1}{\lambda_C}\left(\varepsilon^*_{brb} - \frac{\sigma^*_{brb}}{E_{brb}}\right)}^{\text{Plastic}} \tag{3.1-23}$$

3.1.1.5 Effective Strain Hardening

Because the core plastic and effective truss plastic strains are not equal, a strain hardening ratio, β, appropriate for the yielding core material, is not appropriate for the effective truss material. So, in absence of component testing and calibration, an effective strain hardening ratio, β^*, can be determined based on kinematics, using relationships established in Figure 3.6. In both the yielding core and the effective truss, the increment in axial force after yielding is identical, and can be expressed as a function of both the core material and the effective strain hardening ratios, as can

be seen in Eq. (3.1-24).

$$\Delta P = \begin{cases} \beta k_{yz} \left[(\delta_{brb})_{pl} + \Delta P / k_{yz} \right] & \text{(Yielding Core)} \\ \beta^* k_{brb} \left[(\delta_{brb})_{pl} + \Delta P / k_{brb} \right] & \text{(Effective Truss)} \end{cases} \tag{3.1-24}$$

Solving for ΔP and equating both sides, Eq. (3.1-24) can be rewritten as:

$$\frac{\beta k_{yz}}{1-\beta} = \frac{\beta^* k_{brb}}{1-\beta^*} \tag{3.1-25}$$

Solving for β^* and substituting in the stiffness modification factor, f_{SM}, and detailing ratios, the following expression for the effective strain hardening ratio is acquired:

$$\beta^* = \frac{\beta}{f_{SM} \lambda_B \lambda_C (1-\beta) + \beta} \tag{3.1-26}$$

For detailing ratios (λ_A, λ_B, and λ_C) between zero and one, Eq. (3.1-26) will provide an effective strain hardening ratio larger than the core material strain hardening ratio. In other words, the post-yield stiffness of a BRB is larger than the post-yield stiffness of a traditional brace with the same material and elastic stiffness as the BRB, due to the higher plastic strain demands in the BRB core.

3.1.1.6 Example Application

To demonstrate use of the effective BRB equations, consider a BRB with the following detailing ratios and dimensions, shown in Figure 3.7.

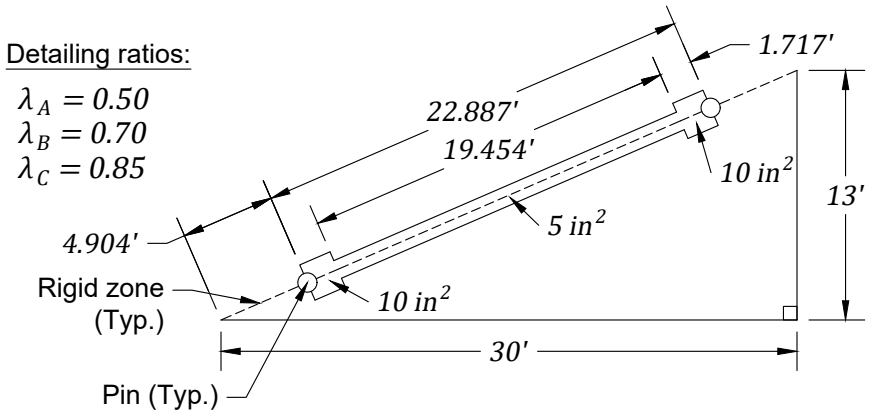

Figure 3.7: Dimensions of example BRB in frame

With the dimensions shown in the figure, the stiffness modification factor, f_{SM}, is approximately 1.544, and the effective truss area, A^*_{brb}, is approximately 5.405 in^2. To validate the kinematic equations, two separate models were built in *OpenSees*, one with components in series, and one with the effective truss, as shown in Figure 3.8.

The material in the core was assumed to have a yield stress of 42 ksi, an elastic modulus of 29,000 ksi, and a kinematic strain hardening ratio of 0.02. With these material properties and the dimensions established in Figure 3.7, the effective yield stress was determined to be 38.85 ksi, and the effective strain hardening ratio was determined to be about 0.0217. Both the "components in series" model and the "effective truss" model were subjected to the same cyclic deformation history, and the force-deformation response of the two models is presented in Figure 3.9.

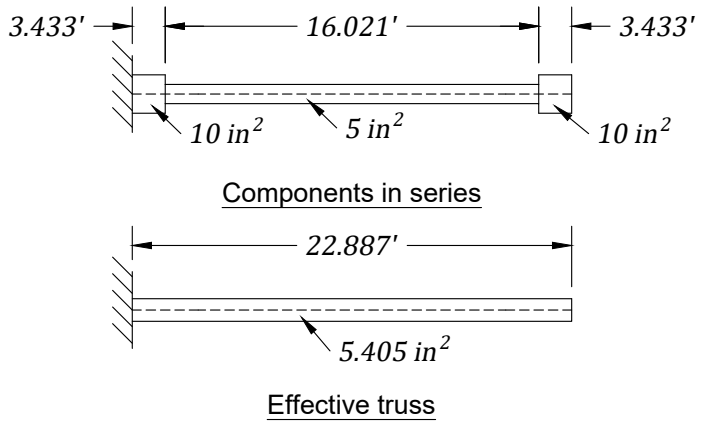

Figure 3.8: Comparison of example BRB dimensions to effective truss

As can be seen in the figure, the global force-deformation responses of the two models are identical. However, the stress-strain response of the yielding core component vs. the effective truss are different, as shown in Figure 3.10. Both the yielding core and effective truss have the same loading and unloading stiffness, but different yield points. Additionally, the plastic strain demand on the core is significantly larger than the plastic strain demand of the effective brace. This highlights the importance of conversion equations between effective stress & strain to yielding core stress & strain. Eqs. (3.1-15) & (3.1-23) were used to back-calculate the yielding core stresses and strains from the effective stresses and strains, and the results are over-plotted in Figure 3.10. As can be seen in the figure, the back-calculated stress-strain values are identical to the values from the "components in series" model. Therefore, the BRB can be modeled as an effective prismatic truss without losing the yielding core stress-strain response.

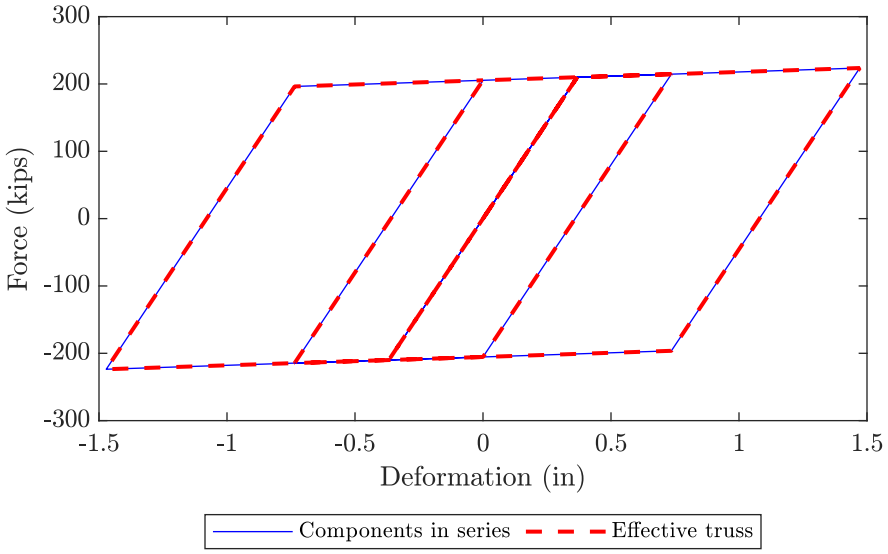

Figure 3.9: Global force-displacement response of brace components in series vs effective prismatic truss

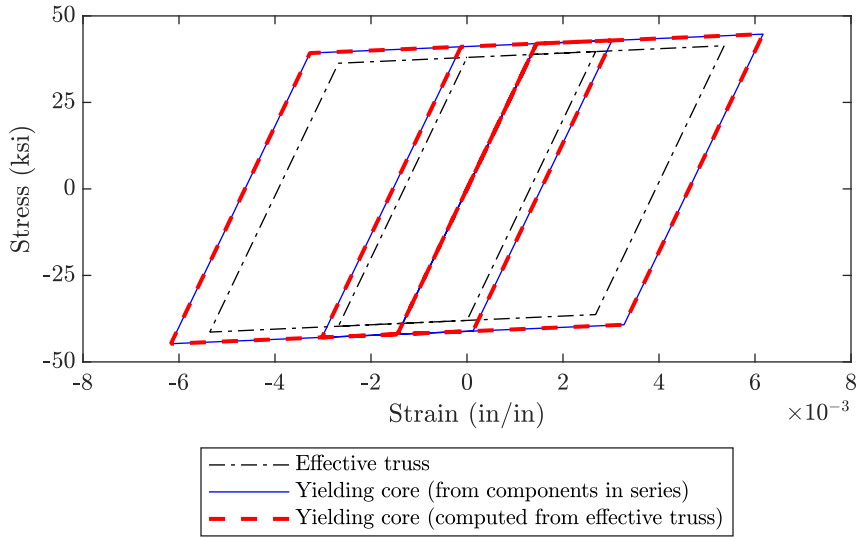

Figure 3.10: Local stress-strain response of yielding core component vs effective prismatic truss

3.1.2 Frame Stiffness

Because the BRBs are the primary seismic force resisting component, the frame kinematics of the NZ-BRBF system are similar to those of conventional diagonally braced BRB frames. A schematic of a diagonally braced BRB frame under frame action is shown in Figure 3.11.

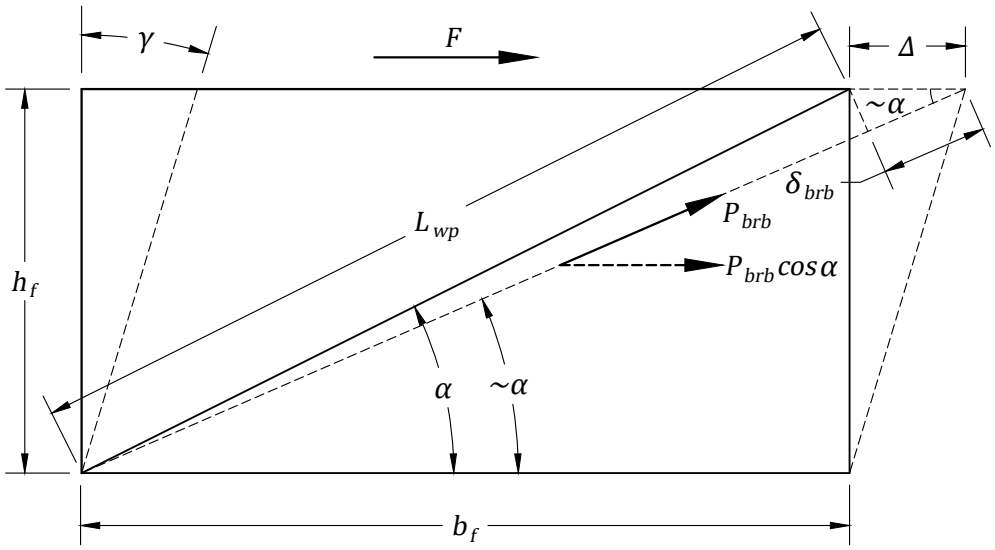

Figure 3.11: Elongation of brace under frame drift

where,

Δ	=	Lateral deflection of frame
γ	=	Story drift
	=	Δ/h_f
δ_{brb}	=	Brace elongation
P_{brb}	=	Axial force in brace
F	=	Lateral force on frame

Assuming a rigid frame and small drift angles, the elongation of the brace (δ_{brb}) is equal to:

$$\delta_{brb} = \Delta \cos\alpha \tag{3.1-27}$$

$$\delta_{brb} = \gamma h_f \cos\alpha \tag{3.1-28}$$

Using an effective stiffness of the brace, k_{brb}, the axial force in the brace in respect to Δ is equal to:

$$P_{brb} = k_{brb}\delta_{brb} = k_{brb}\Delta\cos\alpha \tag{3.1-29}$$

Therefore, the lateral force on the frame in respect to Δ is

$$F = P_{brb}\cos\alpha = k_{brb}\Delta\cos^2\alpha \tag{3.1-30}$$

and the lateral stiffness of the story due the BRB, K_{brb}, is equal to:

$$K_{brb} = F/\Delta = k_{brb}\cos^2\alpha \tag{3.1-31}$$

Substituting Eq. (3.1-5) for k_{brb} in Eq. (3.1-31), the lateral stiffness due to the BRB can be expressed as follows:

$$K_{brb} = f_{SM}\frac{A_{yz}E_{brb}}{L_{wp}}\cos^2\alpha \tag{3.1-32}$$

3.1.3 Peak brace ductility

Peak brace ductility, expressed as μ_{max}, is measured as the ratio of ultimate brace deformation to brace yield deformation, as is shown in Eq. (3.1-33), where δ_{max} represents the absolute maximum value of δ_{brb}.

$$\mu_{max} = \frac{\delta_{max}}{\delta_y} \tag{3.1-33}$$

Brace ductility demand is an important measure of damage, because ductility demand exceeding the capacity of a BRB component may cause component or connection failure [26]. So, to better understand this important quantity in relation to the system response, an alternate form of Eq. (3.1-33) was determined in respect to story drift. Substituting Eq. (3.1-28) for δ_{max} and $\varepsilon_y^* L_{brb}$ for δ_y, the following is obtained, where γ_{max} represents the absolute maximum value of γ.

$$\mu_{max} = \left(\frac{h_f \cos\alpha}{\varepsilon_y^* L_{brb}} \right) \gamma_{max} \tag{3.1-34}$$

Then, substituting Eq. (3.1-14) for ε_y^* and $\sin\alpha$ for h_f/L_{wp}, brace ductility can be expressed in terms of the stiffness modification factor f_{SM}, the brace angle α, the material yield strain ε_y, and the peak story drift γ_{max}, as shown in Eq. (3.1-35).

$$\mu_{max} = \left(\frac{f_{SM} \sin\alpha \cos\alpha}{\varepsilon_y} \right) \gamma_{max} \tag{3.1-35}$$

3.2 NewZ-BREAKSS (NZ) Boundary Frame

The NZ-BRBF system utilizes the NewZ-BREAKSS (NZ) boundary frame to enhance the post-yield stiffness of the system and provide damage-free detailing. The enhanced post-yield stiffness of the system provided by the PT components, while the damage-free detailing is provided by the NZ frame's unique top-flange HBE-to-VBE rocking connection, which is designed to eliminate undesirable "beam growth" present in other rocking frame configurations [2]. A representation of the NZ boundary frame in a rightward drift condition with dimensions and variables labeled is shown in Figure 3.12.

While some kinematic equations have been developed for the NZ boundary frame, no closed-form expression for the contribution to lateral stiffness provided by the NZ boundary frame has been developed [1]. Additionally, while rationale has been provided for selecting the PT parameters, the rationale was limited in application to steel plate shear walls (SPSWs) [27]. Therefore, in pursuit of greater understanding of the NZ boundary frame global behavior and to establish a more generalized basis for design, kinematic equations were developed to characterize the forces in the PT elements and the contribution to lateral stiffness provided by the NZ boundary frame.

Although previous work on the kinematics of the NZ boundary frame accounted for a flexible boundary frame, the assumption of a rigid boundary frame was adopted in developing the kinematic equations. This simplification was made because the intent of the work is simply to provide design guidance and insights into system behavior.

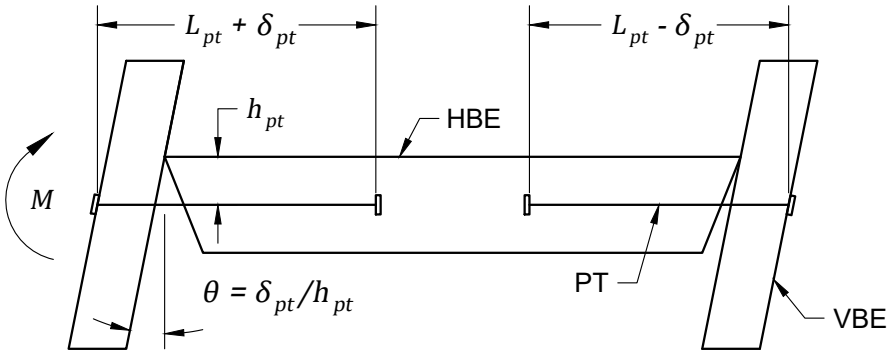

Figure 3.12: Idealized representation of the NZ boundary frame

where,

M	=	Moment resisted by NZ rocking connection.
θ	=	Column angle at PT anchor (assumed equal at both sides).
δ_{pt}	=	PT elongation/shortening for left/right PT due to column rotation
L_{pt}	=	Length of PT (Modeled)
h_{pt}	=	Offset of PT from HBE top flange
	=	$d_{hbe}/2$

3.2.1 PT Component Forces

In order to compute the NZ boundary frame stiffness, an expression for PT component force must be established. The elastic axial force in the left and right PT components, F_{ptl} and F_{ptr}, can be expressed as shown in Eqs. (3.2-1) & (3.2-2),

$$F_{ptl} = \frac{A_{pt}E_{pt}}{L_{pt}}(\delta_{pto} + \delta_{pt}) \geq 0 \tag{3.2-1}$$

$$F_{ptr} = \frac{A_{pt}E_{pt}}{L_{pt}}(\delta_{pto} - \delta_{pt}) \geq 0 \tag{3.2-2}$$

where A_{pt} is the area of the PT component, E_{pt} is the elastic modulus of the PT material, L_{pt} is the modeled length of the PT component, and δ_{pto} is the effective initial elongation of the PT component, as shown in Eq. (3.2-3),

$$\delta_{pto} = \varepsilon_{pto}L_{pt} \tag{3.2-3}$$

where ε_{pto} is the effective initial PT strain, as shown in Eq. (3.2-4),

$$\varepsilon_{pto} = \frac{F_{pto}}{A_{pt}E_{pt}} \tag{3.2-4}$$

where F_{pto} is the initial post-tensioning force of the PT components.

3.2.2 NZ Boundary Frame Stiffness

Previous experimental and numerical studies have shown that the NZ boundary frame exhibits a bilinear elastic force-displacement response [1], [27], but analytical equations for the stiffness have not yet been developed. So, because the effects of the

PT parameters on the frame stiffness are of interest for design purposes, analytical equations for the NZ boundary frame stiffness were developed and are presented below.

The stiffness of the NZ boundary frame was developed using Castigliano's first theorem (stiffness approach), which derives the stiffness as the second derivative of the internal energy of the system in respect to displacement [28]. Consider a single-bay NZ boundary frame in a rightward drift condition, shown in Figure 3.12. In this condition, the left PT elongates and the right PT relaxes (i.e., loss in PT forces). Assuming rigid boundary frame behavior, the internal energy of the frame can be expressed entirely in terms of the PT elastic elongation.

The internal energy of the PT elements can be calculated as the internal elastic energy of springs in tension (the area under the elastic force-displacement curve equal to one half the stiffness times the displacement squared). Then, modeling the PT elements as tension-only springs, the internal strain energy of the system is equal to:

$$U_{pt} = \begin{cases} U_{pt1} & \text{if } \delta_{pt} \leq \delta_{pto} \\ U_{pt2} & \text{if } \delta_{pt} > \delta_{pto} \end{cases} \tag{3.2-5}$$

where,

$$U_{pt1} = \overbrace{\frac{1}{2}\frac{A_{pt}E_{pt}}{L_{pt}}(\delta_{pto} + \delta_{pt})^2}^{\text{Left PT}} + \overbrace{\frac{1}{2}\frac{A_{pt}E_{pt}}{L_{pt}}(\delta_{pto} - \delta_{pt})^2}^{\text{Right PT}} \tag{3.2-6}$$

$$U_{pt2} = \frac{1}{2}\frac{A_{pt}E_{pt}}{L_{pt}}(\delta_{pto} + \delta_{pt})^2 + 0 \tag{3.2-7}$$

Note that the "Right PT" portion of the internal energy goes to zero when $\delta_{pt} > \delta_{pto}$. Simplifying and substituting the relationship between δ_{pt} and θ from Figure 3.12 into

Eqs. (3.2-6) & (3.2-7), the internal energy with respect to θ is obtained:

$$U_{pt1} = \frac{A_{pt}E_{pt}}{L_{pt}}\left({\delta_{pto}}^2 + {h_{pt}}^2\theta^2\right) \tag{3.2-8}$$

$$U_{pt2} = \frac{1}{2}\frac{A_{pt}E_{pt}}{L_{pt}}\left({\delta_{pto}}^2 + 2\delta_{pto}h_{pt}\theta + {h_{pt}}^2\theta^2\right) \tag{3.2-9}$$

Because stiffness is derived from internal energy and the expression for internal energy is in two parts, the NZ boundary frame stiffness K_{nz} is also divided into two parts: K_{nz1} and K_{nz2}.

$$K_{nz} = \begin{cases} K_{nz1} & \text{if } \delta_{pt} \leq \delta_{pto} \\ K_{nz2} & \text{if } \delta_{pt} > \delta_{pto} \end{cases} \tag{3.2-10}$$

where,

$$K_{nz1} = \frac{d^2}{d\theta^2}U_{pt1} \tag{3.2-11}$$

$$K_{nz2} = \frac{d^2}{d\theta^2}U_{pt2} \tag{3.2-12}$$

Solving for the second derivative of Eqs. (3.2-8) & (3.2-9) with respect to θ, the following is obtained:

$$K_{nz1} = 2\frac{A_{pt}E_{pt}}{L_{pt}}{h_{pt}}^2 \tag{3.2-13}$$

$$K_{nz2} = \frac{A_{pt}E_{pt}}{L_{pt}}{h_{pt}}^2 = \frac{1}{2}K_{nz1} \tag{3.2-14}$$

Therefore, the NZ boundary frame has a bilinear stiffness response, with a secondary stiffness equal to half the initial stiffness. Both the initial and secondary stiffnesses

are increased by increasing the PT area, reducing the strand length, and/or increasing the eccentricity depth.

3.2.3 Softening Point

The softening point occurs when the right PT element (for a rightward drift condition) becomes slack, or when the elongation of the PT due to column rotation, δ_{pt}, equals the initial elongation of the PT, δ_{pto}. From a design-standpoint, it is advantageous to delay the softening point, so that the full stiffness of the PT boundary frame is realized for a larger range of column rotation angles. A representation of the PT boundary frame stiffness and the softening point is shown in Figure 3.13. This softening point, expressed as column rotation in terms of effective initial PT elongation, is shown in Eq. (3.2-15).

$$\theta_{pto} = \frac{\delta_{pto}}{h_{pt}} = \frac{\varepsilon_{pto} L_{pt}}{h_{pt}} \tag{3.2-15}$$

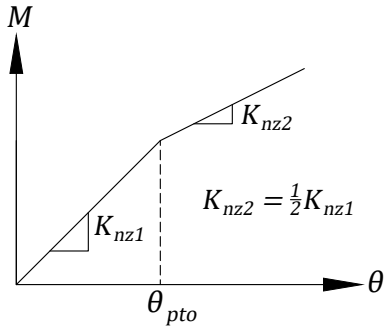

Figure 3.13: NZ boundary frame bilinear stiffness

From Eq. (3.2-15), it is clear that the softening point is pushed back by increasing the initial PT strain, increasing the length of the strands, and/or decreasing the eccentricity depth to the PT. Thus, comparing to Eqs. (3.2-13) & (3.2-14), the

parameters depth and length have opposite effects on the stiffness and softening point. In contrast, increasing the number of PT strands, or the area of PT, has the benefit of increasing the PT boundary frame stiffness without negatively affecting the softening point. Additionally, increased initial strain delays the softening point without negatively affecting the boundary frame stiffness. Therefore, from a design stand-point, it is more advantageous to modify the number of PT strands and initial strain, rather than the PT depth or length, to increase the initial stiffness and delay the softening point.

3.3 Horizontal Boundary Frame Elements (HBE)

Due to the utilization of the NZ boundary frame and atypical BRB anchor details, the kinematic equations governing the demands on the horizontal boundary elements (HBE) of the NZ-BRBF system are unique. Therefore, free-body diagrams and closed-form equations for the axial, shear, and moment along the HBE were developed to better understand the system and inform HBE design.

3.3.1 Complete Free-body Diagrams

For development of free-body diagrams and kinematic equations, an idealized beam was assumed, with five general regions (A-B, B-C, C-D, D-E & E-F), divided by six control points (A, B, C, D, E & F), as shown in Figure 3.14. This is needed for the reason that the HBE axial force, shear, and moment demands along the HBE are not continuous functions. As can be seen in the figure, the beam is idealized to extend to the inside face of the vertical boundary element (VBE), represented by control points A & F. Shear plate and rocking point reactions are assumed to act at control points A & F, BRB resultant forces are assumed to act at control points B & E, and PT

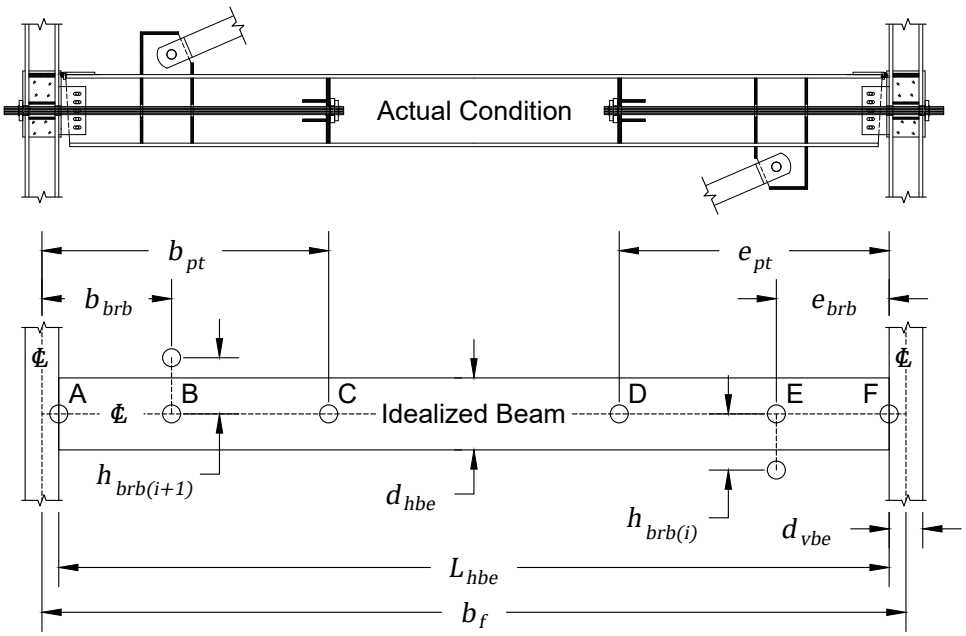

Figure 3.14: Dimensions of idealized HBE (LB configuration)

where,

$L_{hbe} = b_f - d_{vbe}$: Length of HBE

$e_{pt} = b_{pt} - d_{vbe}/2$: Horizontal offset from VBE face to PT anchor on HBE

$e_{brb} = b_{brb} - d_{vbe}/2$: Horizontal offset from VBE face to BRB connection

anchor forces are assumed to act at control points C & D. Using this idealization, the complete resultant force NZ-BRBF HBE free-body diagrams were developed and are shown in Figure 3.15.

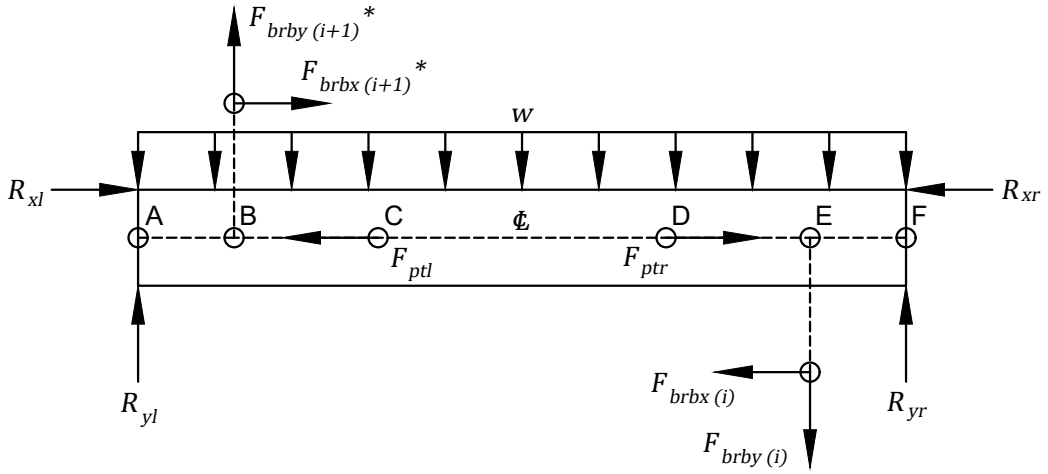

(a) LB configuration

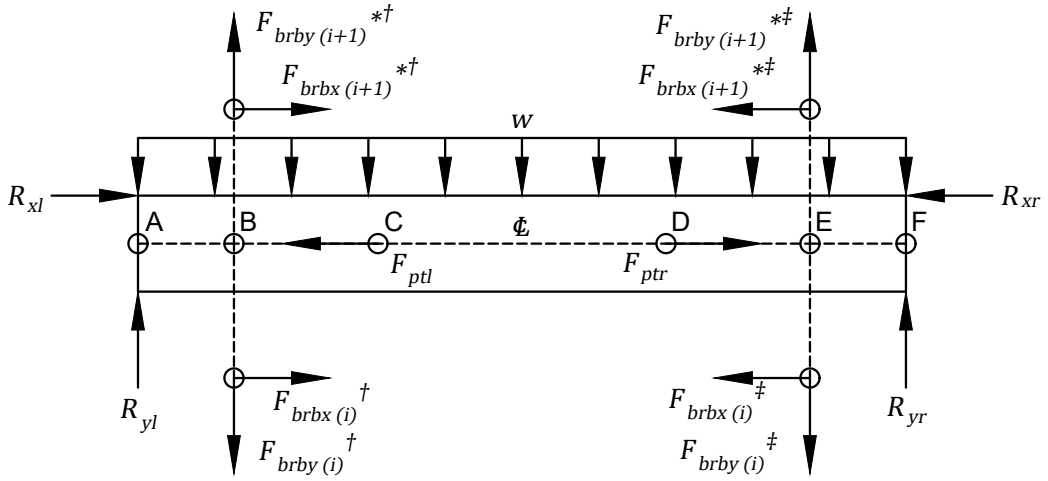

(b) ZZ configuration

Figure 3.15: Complete HBE free-body diagrams

* Not included on roof level
† Not included on odd numbered levels (ZZ configuration)
‡ Not included on even numbered levels (ZZ configuration)

In the free-body diagrams, the distributed dead and live load acting on the beam is represented by the variable w. The BRB axial force, P_{brb}, is separated into its x & y components by the brace angle α referenced from the horizontal, and is represented by F_{brbx} and F_{brby}, as is shown in Eqs. (3.3-1) & (3.3-2). Positive brace force values are taken to indicate tension, and subscripts (i) and $(i+1)$ indicate the floor number of the brace.

$$F_{brbx} = P_{brb} \cos \alpha \tag{3.3-1}$$

$$F_{brby} = P_{brb} \sin \alpha \tag{3.3-2}$$

The tension forces in the PT elements are represented by variables F_{ptl} and F_{ptr}, for the left and right PT, respectively, and are calculated as expressed in Eqs. (3.2-1) & (3.2-2), and are assumed to act at the HBE centerline. Horizontal reaction forces at the top-flange rocking point are represented by variables R_{xl} and R_{xr}, for the left and right reactions, respectively. Because the reaction acts at the top flange, a moment due to eccentricity is introduced at the ends. Vertical reaction forces at the shear plate are represented by variables R_{yl} and R_{yr}, for the left and right reactions, respectively.

3.3.2 Horizontal End Reactions

Although the PT boundary frame does exhibit some lateral stiffness, for design of the HBE, the story force at each level is assumed to be completely resisted by the BRBs, and the amount of shear carried by the columns is assumed to be zero. A free-body diagram of one story with the assumed load path for rightward drift is illustrated in Figure 3.16. Note that the story forces are shown to act completely on the left side of the frame. For leftward drift, the story forces act completely on the right side of the frame. This is an important distinction, and is a result of the unique loadpath of the NZ-BRBF system. With the NZ-BRBF system, the braces are only connected to the

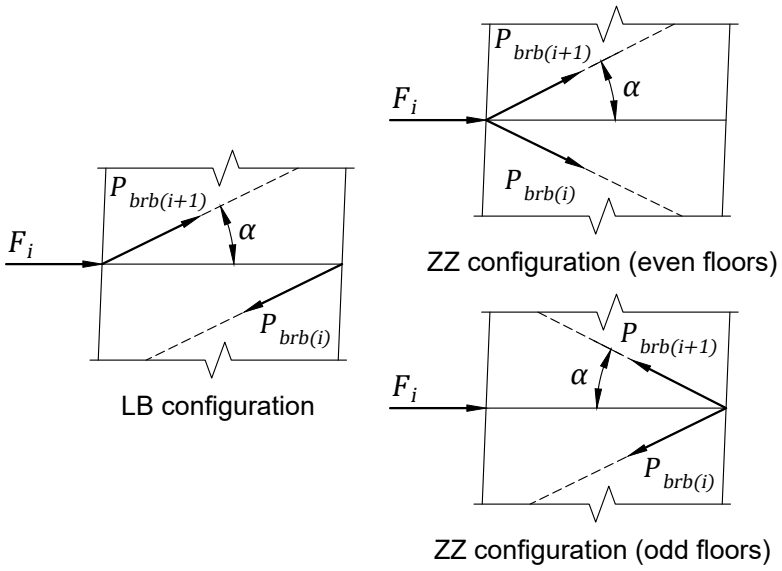

Figure 3.16: Assumed load path of lateral forces under rightward drift

beam, and the beam-column connections are compression only. Any load that would act on the closing gap side of the NZ-BRBF system is assumed to be redistributed to the opening gap side through a rigid diaphragm or similar mechanism.

Summing the lateral forces, the story force F_i is equal to the difference between the x-component of the brace forces in the floor below from the floor above, shown in Eq. (3.3-3). Note that typically, brace force signs will be equivalent in the LB configuration and alternating in the ZZ configuration.

$$F_i = \begin{cases} F_{brbx(i)} - F^*_{brbx(i+1)} & \text{(LB configuration)} \\ F_{brbx(i)} + F^*_{brbx(i+1)} & \text{(ZZ configuration, odd floors)} \\ -F_{brbx(i)} - F^*_{brbx(i+1)} & \text{(ZZ configuration, even floors)} \end{cases} \tag{3.3-3}$$

* Not included on roof level

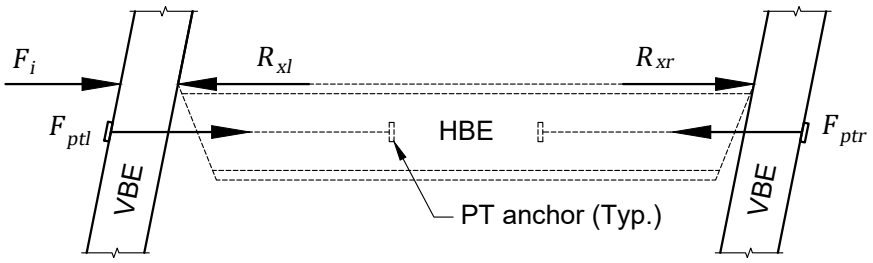

Figure 3.17: VBE horizontal free-body diagram, neglecting column shear

With the same assumption that the columns carry no shear, the horizontal end reactions on the HBE, R_{xl} & R_{xr}, can be expressed in terms of the story force, F_i, and the PT tension forces, F_{ptl} & F_{ptr}. This is illustrated in Figure 3.17 by a horizontal force free-body diagram of the VBE at the rocking connection in rightward drift condition.

Summing the lateral forces for the left and right VBE, the HBE reactions are as shown in Eqs. (3.3-4) & (3.3-5), where F_i is determined based on Eq. (3.3-3). Note that for positive story force (rightward drift), the left reaction carries the story force, while for negative story force (leftward drift), the right side of the beam carries the load. This is accomplished in the equations with simple maximum and minimum functions.

$$R_{xl} = F_{ptl} + \max(F_i, 0) \tag{3.3-4}$$

$$R_{xr} = F_{ptr} - \min(F_i, 0) \tag{3.3-5}$$

It is worth noting that due to the eccentricity of the PT from the top flange of the HBE, the summation of moments in Figure 3.17 are not equal to zero. Therefore, the assumption that the columns carry no shear is not entirely correct. A previous study on the NZ boundary frame accounted for this by assuming that the shear in the column at the base of the column balanced the eccentric PT moment [1]. This led to a reduction in the contribution of the PT to the HBE end reaction. However,

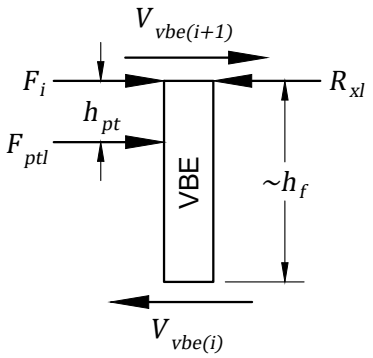

Figure 3.18: Left VBE horizontal free-body diagram, including column shear

the study only considered a single-story structure, with no shear due to PT effects acting in the VBE above the connection. If the shear from the story above, $V_{vbe(i+1)}$, is considered, the supposed reduction of end reaction is minimized, as is shown in Figure 3.18.

Summing the lateral forces in Figure 3.18, the following expression for end reaction is obtained:

$$R_{xl} = F_i + F_{ptl} - (V_{vbe(i)} - V_{vbe(i+1)}) \tag{3.3-6}$$

The shear from the floor above acts in the direction of the story drift, thus minimizing the aforementioned reduction of HBE end reaction for multi-story structures.

Therefore, with the exception of the roof level, in which there is no column shear above, the reduction in PT contribution to HBE end reaction as described in the previous study diminishes for multi-story frames. However, it should be noted that the free-body diagram in Figure 3.18 does not include the VBE end-moments, which would further complicate the determination of the horizontal HBE end reactions. Nevertheless, it can be shown that even for a continuous column, the reduction of PT contribution to end reactions still diminishes for multi-story structures.

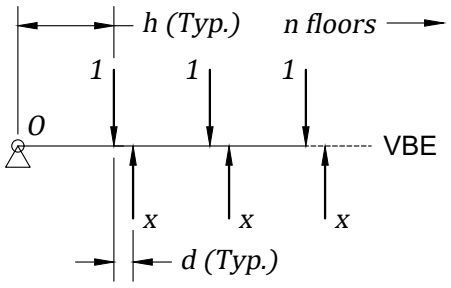

Figure 3.19: Proportion of PT force resisted by HBE end reaction

To demonstrate this, consider a continuous beam, representing the VBE, with unit loads evenly spaced by h, shown in Figure 3.19. These unit loads represent the PT forces acting on the HBE. Consider then, evenly spaced loads, x, offset from the unit loads by an eccentricity of d. These represent the contribution of the PT forces to the end reaction between the HBE-to-VBE rocking point. Assuming a pinned end condition and summing the moments about O in Eq. (3.3-7), the proportion of the PT force carried by the HBE horizontal end reactions, x, can be determined by Eq. (3.3-8).

$$\Sigma M_O = \sum_{i=1}^{n} x(ih + d) - \sum_{i=1}^{n} ih = 0 \tag{3.3-7}$$

$$x = \frac{\sum_{i=1}^{n} ih}{\sum_{i=1}^{n} (ih + d)} \tag{3.3-8}$$

For a 1-story structure, Eq. (3.3-8) reduces to $x = h/(h + d)$, and as $n \to \infty$, $x \to 1$. For example, consider a story height, h, of 13 ft and a PT eccentricity, d, of 1 ft. For $n = 1$, the proportion of the PT force carried by the HBE end reactions, x, is about 0.93. For $n = 3$, $x = 0.96$. At 15 stories, the reduction becomes less than 1%. So, the reduction in PT force on the HBE is only slightly significant for short structures. Even in its most extreme case $n = 1$, the reduction is small. Therefore, for design purposes in this study, the entirety of the PT forces was assumed to contribute to the HBE end reactions.

3.3.3 Vertical End Reactions

Determination of left and right vertical end reactions, R_{yl} & R_{yr}, is presented here for both LB and ZZ configurations.

3.3.3.1 Left Vertical End Reaction

Summing the vertical forces in Figures 3.15a & 3.15b , the left vertical end reaction, R_{yl}, is equal to a combination of the distributed gravity load, the vertical brace force components, and the right vertical end reaction.

$$R_{yl} = -R_{yr} + wL_{hbe} + F_{brby(i)} - (F_{brby(i+1)})^{*} \tag{3.3-9}$$

This expression works for both LB and ZZ configurations. The right vertical end reaction, however, requires different equations for the different configurations.

3.3.3.2 Right Vertical End Reaction (LB Configuration)

Summing the moments in Figure 3.15a about point A, the right vertical end reaction, R_{yr}, is equal to:

$$R_{yr} = \frac{1}{L_{hbe}}\Bigg((R_{xl} - R_{xr})\frac{d_{hbe}}{2} + \frac{wL_{hbe}{}^{2}}{2} + F_{brbx(i)}h_{brb(i)} + ... \\ F_{brby(i)}(L_{hbe} - e_{brb}) + \Big(F_{brbx(i+1)}h_{brb(i+1)} - F_{brby(i+1)}e_{brb}\Big)^{*}\Bigg) \tag{3.3-10}$$

* Not included on roof level

3.3.3.3 Right Vertical End Reaction (ZZ Configuration, Odd Floors)

Summing the moments in Figure 3.15b about point A, where the braces are anchored to the right side of the HBE, the right vertical end reaction, R_{yr}, is equal to:

$$R_{yr} = \frac{1}{L_{hbe}}\Bigg((R_{xl} - R_{xr})\frac{d_{hbe}}{2} + \frac{wL_{hbe}{}^2}{2} + F_{brbx(i)}h_{brb(i)} + ... \\ F_{brby(i)}(L_{hbe} - e_{brb}) - \Big(F_{brbx(i+1)}h_{brb(i+1)} + F_{brby(i+1)}(L_{hbe} - e_{brb})\Big)^*\Bigg) \quad (3.3\text{-}11)$$

3.3.3.4 Right Vertical End Reaction (ZZ Configuration, Even Floors)

Summing the moments in Figure 3.15b about point A, where the braces are anchored to the left side of the HBE, the right vertical end reaction, R_{yr}, is equal to:

$$R_{yr} = \frac{1}{L_{hbe}}\Bigg((R_{xl} - R_{xr})\frac{d_{hbe}}{2} + \frac{wL_{hbe}{}^2}{2} - F_{brbx(i)}h_{brb(i)} + ... \\ F_{brby(i)}e_{brb} + \Big(F_{brbx(i+1)}h_{brb(i+1)} - F_{brby(i+1)}e_{brb}\Big)^*\Bigg) \quad (3.3\text{-}12)$$

* Not included on roof level

3.3.4 Axial, Shear and Moment Distribution

In order to determine the internal force distribution along the HBE, section free-body diagrams were cut, and piece-wise axial, shear, and moment equations were developed for the HBE, using the HBE end reactions R_{xl}, R_{xr}, R_{yr}, and R_{yl} established in the previous sections.

3.3.4.1 Region A-B

The section free-body diagram for region A-B, between the left rocking connection and left BRB connection, is shown in Figure 3.20. In this region, the axial force is simply equal to the end reaction, and the shear and moment are typical of a simply supported beam with a distributed load.

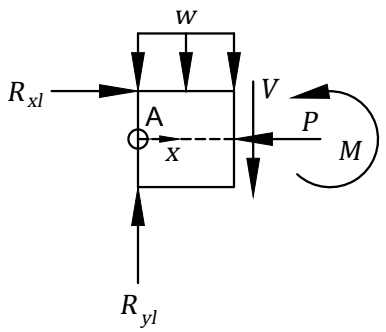

Figure 3.20: Free-body diagram of HBE region A-B

$$P_{AB}(x) = R_{xl} \tag{3.3-13}$$

$$V_{AB}(x) = R_{yl} - wx \tag{3.3-14}$$

$$M_{AB}(x) = \frac{R_{xl} d_{hbe}}{2} + R_{yl} x - \frac{wx^2}{2} \tag{3.3-15}$$

3.3.4.2 Region B-C (LB Configuration)

Region B-C, between the left BRB connection and PT anchor, is shown in Figure 3.21 for an LB configuration frame. Note that for the roof level, the free-body diagrams and kinematic equations are the same as for region A-B.

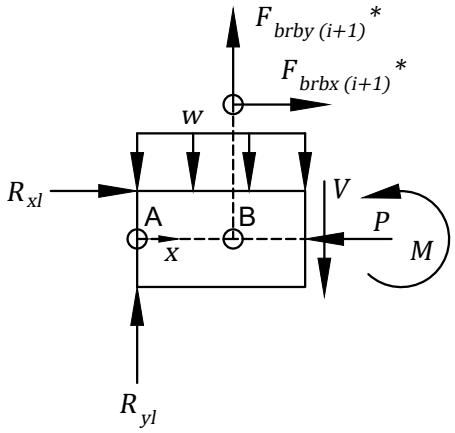

Figure 3.21: Free-body diagram of HBE region B-C (LB configuration)

$$P_{BC}(x) = R_{xl} + F_{brbx(i+1)}{}^{*} \tag{3.3-16}$$

$$V_{BC}(x) = R_{yl} - wx + F_{brby(i+1)}{}^{*} \tag{3.3-17}$$

$$M_{BC}(x) = \frac{R_{xl} d_{hbe}}{2} + R_{yl} x - \frac{wx^2}{2} + ... \left(F_{brbx(i+1)} h_{brb(i+1)} + F_{brby(i+1)}(x - e_{brb})\right)^{*} \tag{3.3-18}$$

* Not included on roof level

3.3.4.3 Region B-C (ZZ Configuration)

Region B-C, between the left BRB connection and PT anchor, is shown in Figure 3.22 for a ZZ configuration frame. Note that for odd-numbered floors, the free-body diagrams and kinematic equations are the same as for region A-B.

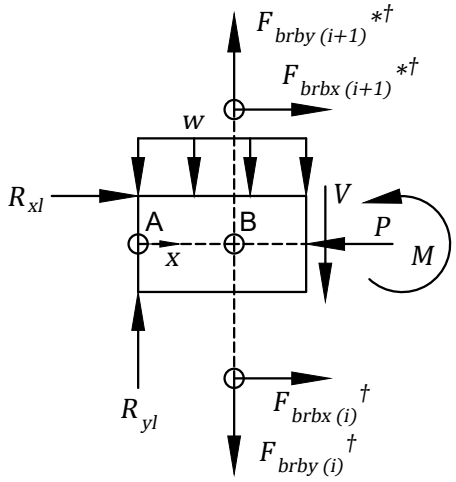

Figure 3.22: Free-body diagram of HBE region B-C (ZZ configuration)

$$P_{BC}(x) = R_{xl} + {F_{brbx(i)}}^{\dagger} + {F_{brbx(i+1)}}^{*\dagger} \tag{3.3-19}$$

$$V_{BC}(x) = R_{yl} - wx - {F_{brby(i)}}^{\dagger} + {F_{brby(i+1)}}^{*\dagger} \tag{3.3-20}$$

$$\begin{aligned} M_{BC}(x) = {} & \frac{R_{xl} d_{hbe}}{2} + R_{yl} x - \frac{wx^2}{2} + ... \\ & - \left(F_{brbx(i)} h_{brb(i)} + F_{brby(i)}(x - e_{brb})\right)^{\dagger} + ... \\ & \left(F_{brbx(i+1)} h_{brb(i+1)} + F_{brby(i+1)}(x - e_{brb})\right)^{*\dagger} \end{aligned} \tag{3.3-21}$$

* Not included on roof level
† Not included on odd numbered levels

3.3.4.4 Region C-D (LB Configuration)

Region C-D, between PT anchors, is shown in Figure 3.23 for an LB configuration frame. The left PT force, F_{ptl}, is introduced to the equation for axial force. Otherwise, the shear and moment equations are identical to those in region B-C.

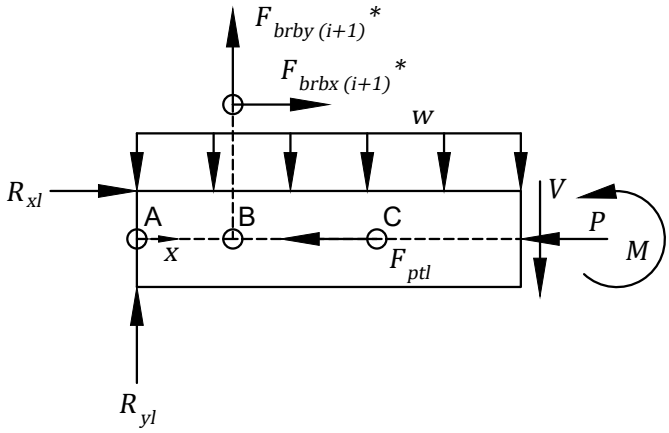

Figure 3.23: Free-body diagram of HBE region C-D (LB configuration)

$$P_{CD}(x) = R_{xl} + F_{brbx(i+1)}{}^{*} - F_{ptl} \tag{3.3-22}$$

$$V_{CD}(x) = V_{BC}(x) \tag{3.3-23}$$

$$M_{CD}(x) = M_{BC}(x) \tag{3.3-24}$$

* Not included on roof level

3.3.4.5 Region C-D (ZZ Configuration)

Region C-D, between PT anchors, is shown in Figure 3.24 for a ZZ configuration frame. The left PT force, F_{ptl}, is introduced to the equation for axial force. Otherwise, the shear and moment equations are identical to those in region B-C.

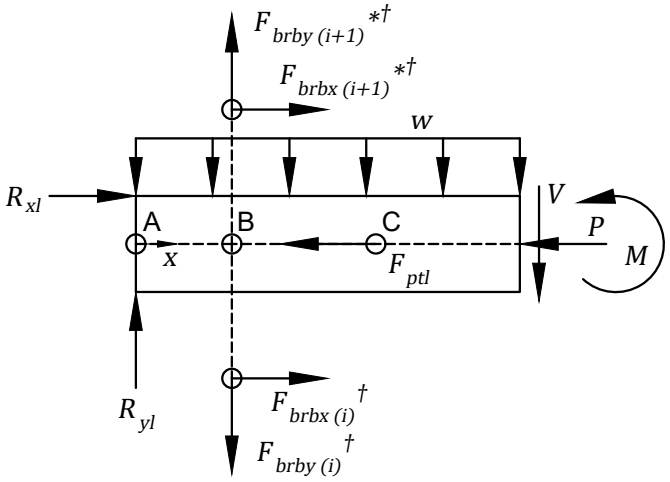

Figure 3.24: Free-body diagram of HBE region C-D (ZZ configuration)

$$P_{CD}(x) = R_{xl} + {F_{brbx(i)}}^{\dagger} + {F_{brbx(i+1)}}^{*\dagger} - F_{ptl} \tag{3.3-25}$$

$$V_{CD}(x) = V_{BC}(x) \tag{3.3-26}$$

$$M_{CD}(x) = M_{BC}(x) \tag{3.3-27}$$

* Not included on roof level
† Not included on odd numbered levels

3.3.4.6 Region D-E (LB Configuration)

Region D-E, between the right PT anchor and right BRB connection, is shown in Figure 3.25 for an LB configuration frame. The right PT force, F_{ptr}, is introduced to the equation for axial force. Otherwise, the shear and moment equations are identical to those in region B-C.

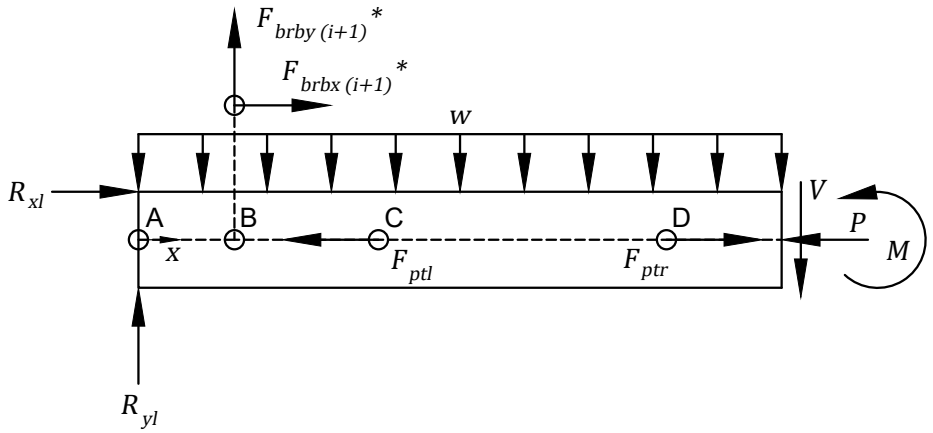

Figure 3.25: Free-body diagram of HBE region D-E (LB configuration)

$$P_{DE}(x) = R_{xr} + F_{brbx(i+1)}{}^{*} - F_{ptl} + F_{ptr} \tag{3.3-28}$$

$$V_{DE}(x) = V_{BC}(x) \tag{3.3-29}$$

$$M_{DE}(x) = M_{BC}(x) \tag{3.3-30}$$

3.3.4.7 Region D-E (ZZ Configuration)

Region D-E, between the right PT anchor and right BRB connection, is shown in Figure 3.26 for a ZZ configuration frame. The right PT force, F_{ptr}, is introduced to the equation for axial force. Otherwise, the shear and moment equations are identical to those in region B-C.

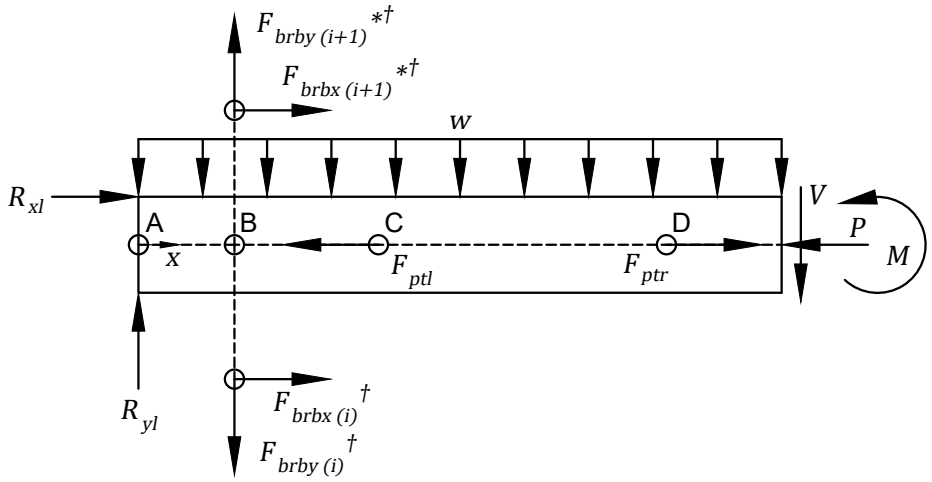

Figure 3.26: Free-body diagram of HBE region D-E (ZZ configuration)

$$P_{DE}(x) = R_{xr} + F_{brbx(i)}{}^{\dagger} + F_{brbx(i+1)}{}^{*\dagger} - F_{ptl} + F_{ptr} \tag{3.3-31}$$

$$V_{DE}(x) = V_{BC}(x) \tag{3.3-32}$$

$$M_{DE}(x) = M_{BC}(x) \tag{3.3-33}$$

* Not included on roof level
† Not included on odd numbered levels

3.3.4.8 Region E-F

The last region, region E-F, between the right BRB connection and the right end connection, is shown in Figure 3.27. The equations for axial, shear and moment in this region are similar in form to those for region A-B.

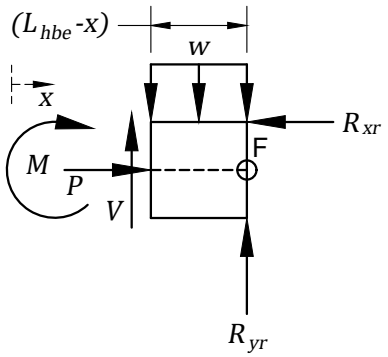

Figure 3.27: Free-body diagram of HBE region E-F

$$P_{EF}(x) = R_{xr} \tag{3.3-34}$$

$$V_{EF}(x) = -R_{yr} + w(L_{hbe} - x) \tag{3.3-35}$$

$$M_{EF}(x) = \frac{R_{xr} d_{hbe}}{2} + R_{yr}(L_{hbe} - x) - \frac{w(L_{hbe} - x)^2}{2} \tag{3.3-36}$$

3.4 Vertical Boundary Frame Elements (VBE)

The vertical boundary frame elements (VBEs) are continuous between floors, so closed form equations for VBE demands are dependent on building height and configuration. Therefore, closed form equations for VBE demand are not presented here, but it is important to discuss the impact of column base detailing on overall system response.

Typically, BRBFs have fixed column bases [4], [29], [30]. However, this means that the column bases are susceptible to permanent damage during a seismic event. The typical alternative is to use a pinned base. However, this is undesirable for multi-story braced structures, for two reasons. First of all, a pinned column base results in a single-curvature drift profile, concentrating demand on the first floor. Second, the pinned fixity on the first floor results in a significantly lower boundary frame stiffness, resulting in a soft-story mechanism after the first floor brace yields. This combination of effects results in a fragile system with little redundancy, which goes against the objectives of collapse prevention and life-safety.

To address both of these issues while minimizing damage to the column base, the first floor column is fixed at the base and has a moment release hinge at the midpoint. The detail greatly increases the elastic boundary frame stiffness of the first floor, while allowing for the column base to remain essentially elastic. Additionally, because the moment release is located at the first floor column midpoint, the column angle θ at the first level is half that of the first floor drift γ (assuming a rigid VBE), as shown in Figure 3.28. This greatly reduces strain demand on the first floor brace, practically ensuring that the second floor brace will fail before the first floor. The combination of these two effects greatly improves the collapse capacity of the NZ-BRBF system, while maintaining the performance objective of seismic resiliency.

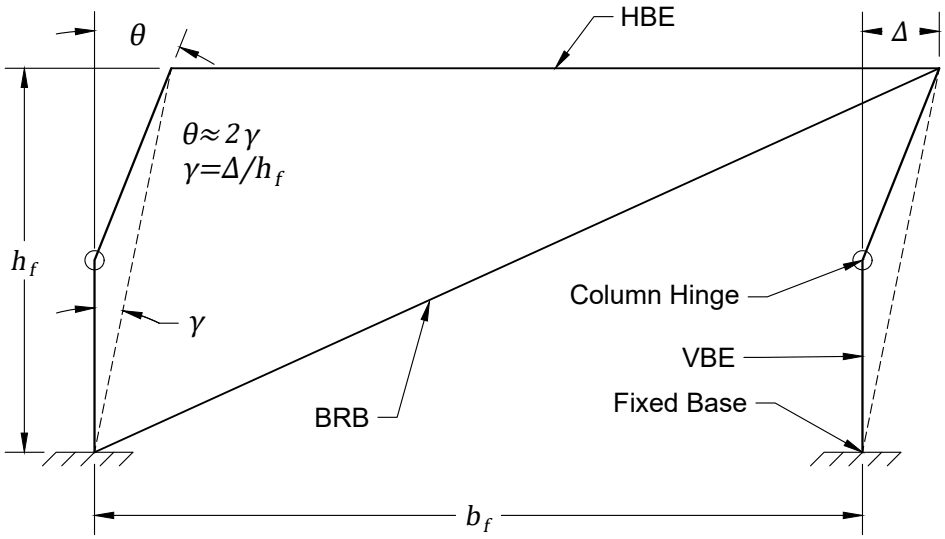

Figure 3.28: Column angle and story drift for first floor with column hinge at midpoint

3.5 Summary

In this chapter, equations were established for determining effective BRB brace sizes and material properties, which are used for numerical modeling of the NZ-BRBF system in this study. Then, frame stiffness equations were developed for both the BRB component and the NZ boundary frame, which help to understand the system and inform design. To further inform design, closed-form equations were developed for the axial, shear, and moment HBE demands, which can be used for the preliminary sizing of boundary frame members. Finally, the effects of and rationale behind using the unique column base detail (midpoint hinge) were discussed.

Chapter 4

Index Archetype Design

This chapter presents the development and design of the NZ-BRBF index archetype configurations. The resulting designs are used in subsequent chapters for evaluation of the proposed seismic performance factors (SPFs).

4.1 Archetype Configurations

For this study, a total of 10 index archetype buildings were studied, spanning a design space of four building heights (1, 3, 6, and 9 stories), and two brace configurations (LB and ZZ), and two levels of post-tensioning (14 and 22 strands). The ZZ brace configuration was only investigated for 3-story archetypes, and was determined to not have a significant impact on results, and to not be the controlling brace configuration. Variation in gravity loading was not considered, because the design of the main seismic force resisting elements (BRBs) is not dependent on gravity loads. The archetype IDs with their corresponding brace configurations and building heights are shown in Table 4.1.

Table 4.1: Building archetypes

Archetype ID	Stories	Brace Configuration	PT Strands
1S-LB-14	1	LB	14
1S-LB-22	1	LB	22
3S-LB-14	3	LB	14
3S-LB-22	3	LB	22
3S-ZZ-14	3	ZZ	14
3S-ZZ-22	3	ZZ	22
6S-LB-14	6	LB	14
6S-LB-22	6	LB	22
9S-LB-14	9	LB	14
9S-LB-22	9	LB	22

The archetype buildings for this study were developed based on SAC Steel Project model buildings [31]. These model buildings were developed to be typical of office buildings, and have been widely used as benchmark buildings for other SFRSs [10], [23], [32]. Building plan and elevations for the archetype buildings are shown in Figure 4.1.

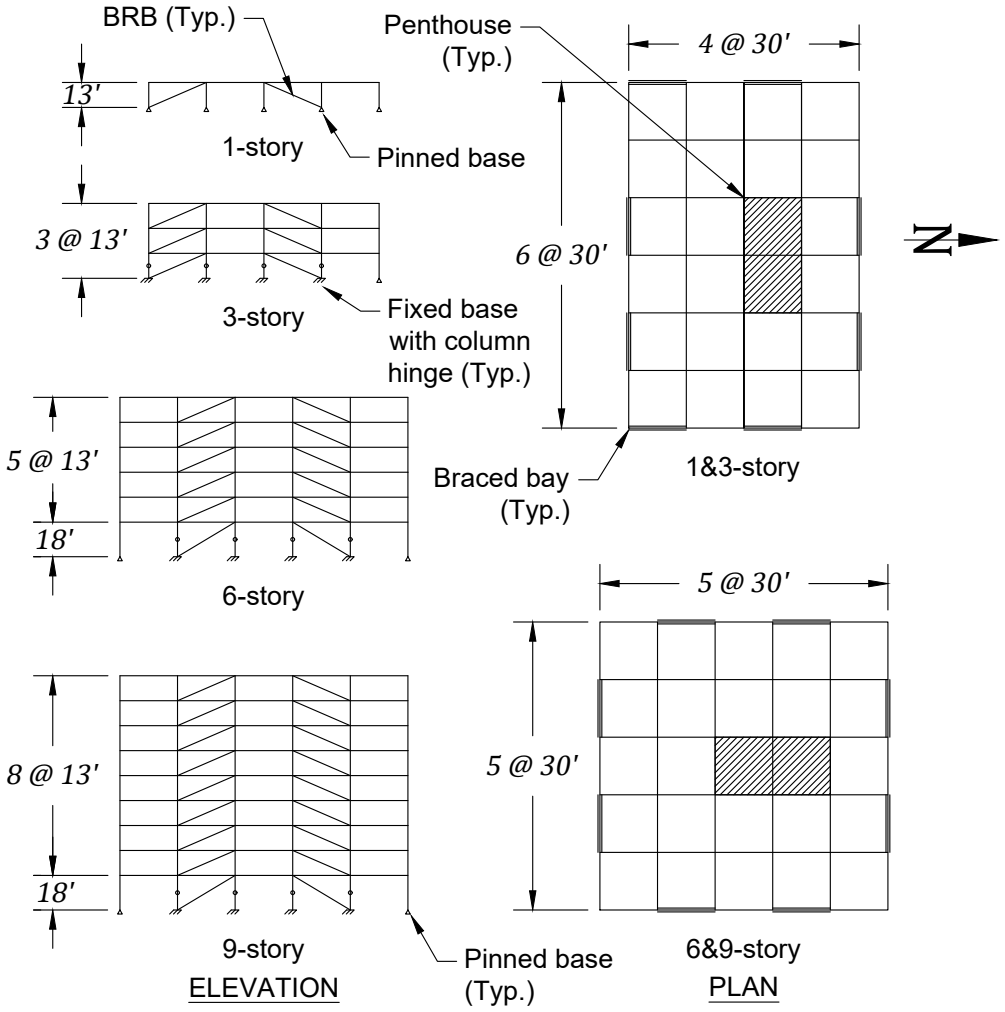

Figure 4.1: Floor plan and elevation for archetype buildings (LB brace configuration shown)

4.2 Design Requirements

In accordance with the P-695, designs for archetypes were developed in accordance with applicable design standards and documents. Design loading for the index archetypes was applied in accordance with *"Minimum Design Loads and Associated Criteria for Buildings and Other Structures, ASCE/SEI 7-16"*, hereafter referred to as ASCE 7-16 [33]. In particular, the Equivalent Lateral Force (ELF) procedure specified in ASCE 7 was used for seismic design. BRB design and resulting overstrength on the boundary frame was determined in accordance with *"Seismic Provisions for Structural Steel Buildings, AISC 341-16"*, hereafter referred to as AISC 341-16 [34]. Additional guidance for BRB design was obtained from *"Seismic Design of Steel Buckling-Restrained Braced Frames: A Guide for Practicing Engineers"* [25]. Demand on boundary frame members was determined based on the capacity-limited seismic effect from the BRBs as prescribed by AISC 341, and using load combinations as prescribed by the P-695 methodology. Finally, boundary frame member capacities were determined according to *"Specifications for Structural Steel Buildings, AISC 360-16"*, hereafter referred to as AISC 360 [35].

These design documents helped to inform the design requirements for the NZ-BRBF index archetype designs. These design requirements establish the information needed for sizing and detailing the system components, and set boundaries on the application of the proposed SFRS.

The BRBs in the NZ-BRBF system were sized to resist the entirety of the ELF loads per ASCE 7-16, and were detailed in accordance with strength requirements per AISC 341-16 for BRBFs. Supplemental yield requirements of 42 ksi $\pm$ 4 ksi were used for the steel core of the BRBs, as is common in practice [25]. Due to lack of coupon testing of the steel core, the axial yield strength of the core was calculated with the

minimum specified yield stress of 38 ksi, and the adjusted strength of the core for overstrength on boundary frame members was calculated with the maximum specified yield stress of 46 ksi.

Because brace detailing can vary significantly between manufacturers, a general BRB configuration was assumed, with brace detailing ratios as defined in Eqs. (3.1-7), (3.1-8) & (3.1-9). For this study, brace detailing ratios of $\lambda_A = 0.5$, $\lambda_B = 0.7$, and $\lambda_C = 0.85$ were used, as they resulted in realistic detailing dimensions, comparable to reported BRB dimensions [8], [36], [37]. For simplicity, brace detailing ratios were assumed to be kept the same between floors, and core areas were rounded up to the next 0.1 in^2.

In addition to the connection requirements in ASCE 341-16 for BRBFs, BRB connections were assumed to be pinned, with stiffened gusset plate connections sized to ensure that connection failure is precluded by brace rupture. Similarly, the shear plate in the NZ connection was assumed to be capacity designed per AISC 341-16, so shear-plate connection failure was not considered.

The boundary frame members were capacity designed for the adjusted strength of the BRBs, and the demands experienced from a nonlinear static pushover analysis at 4% roof drift, using the ELF lateral load distribution. Although flexural forces resulting from seismic drift may be neglected per AISC 341-16, the NZ-BRBF beam-column and BRB connections are novel and can cause significant moments in the beams and columns. Therefore, end moments created by the NZ beam-column connections were not neglected.

For the post-tensioning (PT) design, the same number of PT strands was used for every floor, and the initial stress was selected such that the PT remains elastic at a beam-column joint rotation angle of 0.04 rad.

4.3 Design Load Cases

The index archetype buildings were designed for the two design load cases as required by the P-695 methodology, as shown in Eqs. (4.3-1) & (4.3-2),

$$(1.2 + 0.2S_{DS})D + L + Q_E \tag{4.3-1}$$

$$(0.9 - 0.2S_{DS})D + Q_E \tag{4.3-2}$$

where S_{DS} is the short-period Design Basis Earthquake (DBE) spectral response value, D is the dead load including structural self-weight and superimposed dead loads, L is the live load (with appropriate reduction factors), and Q_E is the effect from horizontal seismic forces.

Because the BRBs do not contribute to dead and live-load lateral resistance, only Q_E was considered in the design of the BRBs, which were sized to resist the entirety of the equivalent lateral loads. The boundary frame members, however, resist both gravity loads and the capacity-limited seismic load effect from the BRBs, E_{cl}, as defined in AISC 341-16 [34]. Additionally, the forces in the boundary frame members differ for the direction of seismic forces. So, for the seismic ground motion values considered in this study, the following load combinations were used for design of the NZ-BRBF boundary frame:

$$1.4D + L \pm E_{cl} \tag{4.3-3}$$

$$0.7D \pm E_{cl} \tag{4.3-4}$$

4.4 Gravity Loads

Gravity loads on the NZ-BRBF system were taken directly from the SAC model building report. Dead load for each floor was assumed to be equal to the floor/roof seismic weight, as tabulated in Table 4.4, distributed evenly over the building layout, and a reduced live load of 20 psf was assumed for all floors and the roof. Gravity loads were distributed to the boundary frame and the P-Delta leaning column as illustrated in Figure 4.2.

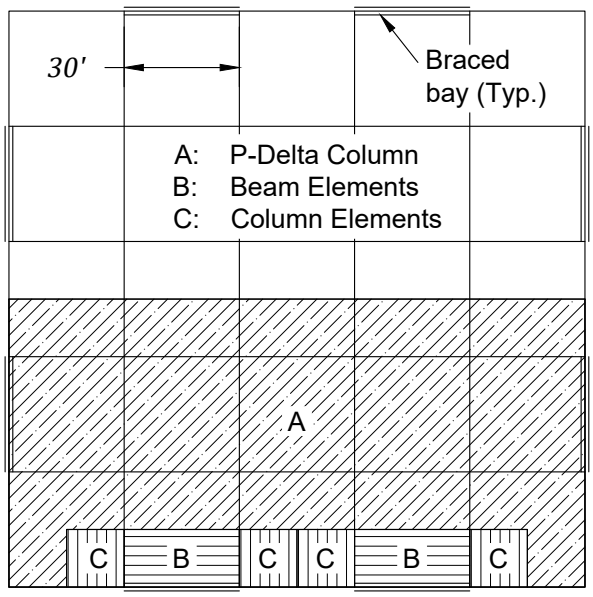

Figure 4.2: Gravity load tributary areas for 6 and 9-story archetypes

4.5 Seismic Design

Seismic design was performed in accordance with the ELF method, as it is consistent with previous P-695 studies on BRB frames [4]. Only the N-S direction was considered in this study, and lateral resistance from the gravity system was neglected. An R factor of 8 was assumed for this study, as it is the reported value in ASCE 7 for BRBFs, and the displacement modification factor C_d was assumed to be equal to R.

4.5.1 Seismic Ground Motion Values

The archetype buildings were assumed to be located in regions of high seismicity, represented by Seismic Design Category (SDC) D_{max} in the P-695. The mapped spectral accelerations and site coefficients are shown in Table 4.2. These parameters correspond to Maximum Considered Earthquake (MCE) spectral response values of $S_{MS} = 1.5g$ and $S_{M1} = 0.90g$, and to Design Basis Earthquake (DBE) spectral response values of $S_{DS} = 1.0g$ and $S_{D1} = 0.60g$.

Table 4.2: SDC D_{max} seismic parameters

Parameter	Value	Description
S_s	1.5	Mapped short-period spectral acceleration (g)
S_1	0.6	Mapped 1-second spectral acceleration (g)
F_a	1.0	Short-period site coefficient
F_v	1.5	Long-period site coefficient

4.5.2 Fundamental Period and Design Spectral Acceleration

The fundamental period for use in designing the index archetype buildings and anchoring ground motions was determined in accordance with the P-695 Methodology, using Eq. (4.5-1), where C_u is the coefficient for the upper limit on the calculated period, equal to 1.4 for SDC D_{max}, C_t and x are the approximate period coefficients, equal to 0.03 and 0.75 for buckling-restrained braced frames, and h_n is the structural height in feet.

$$T = C_u C_t h_n^x \tag{4.5-1}$$

The design spectral acceleration, S_a, was determined in accordance with ASCE 7-16, using the seismic ground motion values established in Table 4.2. The structural height, fundamental period, and design spectral acceleration for the four archetype building heights are shown in Table 4.3, and illustrated in Figure 4.3

Table 4.3: Fundamental period and design spectral acceleration

Stories	h_n (ft)	T (s)	S_a (g)
1	13	0.288	1.000
3	39	0.655	0.915
6	83	1.155	0.520
9	122	1.542	0.389

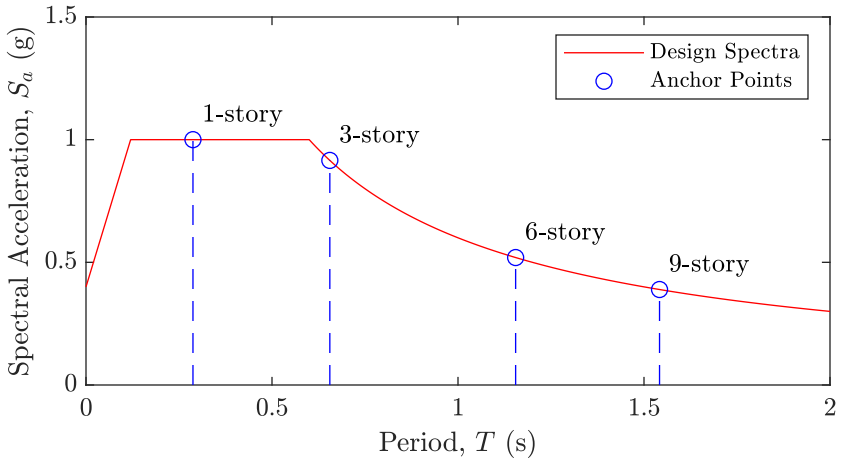

Figure 4.3: Design spectrum for archetype buildings

4.5.3 Seismic Mass and Base Shear

Seismic masses for each level of the archetype buildings were taken directly from the SAC model building report. These seismic masses include floor dead loads, cladding and parapet loads, the dead load of the penthouse on the roof level, and an assumed steel self-weight [31]. The corresponding level masses are summarized in Table 4.4. The total seismic weight, W, was determined by summing the level masses and mul-

Table 4.4: Seismic masses

Stories	Levels	Mass (kip-sec^2/ft)
1	1	70.9
3	1 - 2	65.53
	3	70.9
6	1	69.04
	2 - 5	67.86
	6	73.1
9	1	69.04
	2 - 8	67.86
	9	73.1

tiplying by gravity. The total base shear, V, was taken as the product of the total seismic weight and the seismic response coefficient, C_s, calculated in accordance with the provisions of ASCE 7-16. The total seismic weight, the seismic response coefficient, and the total base shear are summarized in Table 4.5.

Table 4.5: Total base shear

Stories	W (kips)	C_s	V (kips)
1	2281	0.125	285
3	6498	0.114	744
6	13307	0.065	864
9	19857	0.049	966

4.5.4 Base Shear Distribution and Brace Sizes

The total base shear was distributed evenly between the four braced bays, and was distributed to the floors in accordance with the provisions of ASCE 7-16. The story shear was then assumed to be fully resisted by the yielding core of the BRBs, assuming the minimum specified yield stress of 38 ksi and a strength reduction factor of 0.9 per AISC 341. The resulting story shear and yielding core sizes (rounded up to next 0.1 in^2) are summarized in Table 4.6

Table 4.6: Brace sizes

Stories	Level	Story shear (kips)	BRB core area (in^2)
1	1	71.3	2.3
3	1	185.9	6
	2	157.9	5.1
	3	98.9	3.2
6	1	216.0	7.4
	2	207.3	6.7
	3	189.7	6.1
	4	161.7	5.2
	5	122.1	3.9
	6	70.2	2.3
9	1	241.5	8.3
	2	238.4	7.6
	3	231.4	7.4
	4	219.5	7
	5	201.9	6.5
	6	177.8	5.7
	7	146.6	4.7
	8	107.6	3.5
	9	60.4	2

4.6 Adjusted Strength of BRBs

While the BRBs are sized to resist the entirety of the seismic forces at the minimum yield stress, the boundary frame must be designed to resist the maximum forces that could be developed in the BRBs, in order to ensure that the boundary frame remains essentially elastic. For this study, the adjusted strength of the BRBs was taken to be the maximum yield stress, 46 ksi, times the overstrength at the expected brace deformation.

In addition to using the maximum yield stress, the stress in tension and compression are modified by overstrength factors ω and β, defined as shown in Figure 4.4, where δ_y is the brace yield displacement and δ_m is the expected brace deformation, as required by AISC 341. These factors typically range in value from 1.3 to 1.5 for ω and 1.05 to 1.15 for β [25]. Therefore, in lieu of testing data, overstrength factors of $\omega = 1.4$ and $\beta = 1.1$ were selected for this study.

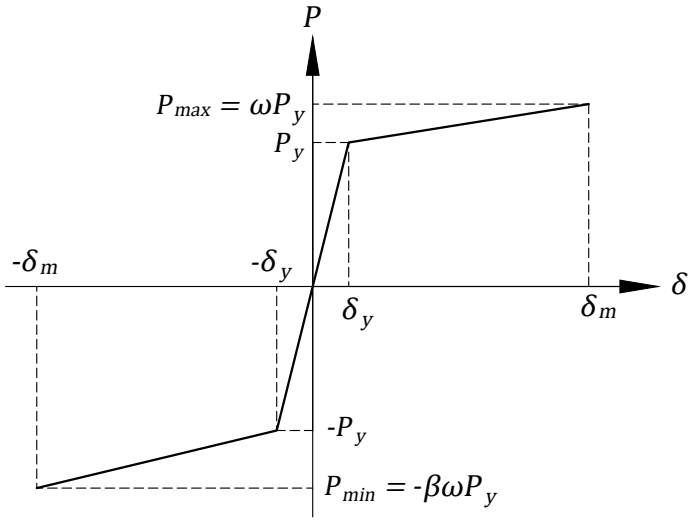

Figure 4.4: BRB force-displacement backbone curve

With the maximum yield stress of 46 ksi and overstrength factors of $\omega = 1.4$ and $\beta = 1.1$, the adjusted strengths in tension and compression are 64.4 ksi and -70.84 ksi, respectively. These overstrength stresses, multiplied by the BRB yielding core areas, give the overstrength brace forces that need to be resisted by the boundary frame.

4.7 Boundary Frame Design

The boundary frame members were capacity designed for the adjusted strength of the BRBs, the demands from an ELF lateral load pattern at 4% roof drift, and the gravity loads tributary to each frame. The PT strands were assumed to be 0.6 in (15.2 mm) diameter 270 grade, low-relaxation strands. Each PT strand was assumed to have an initial stress equal to 30% of yield stress, where the yield stress was taken to be equal to 90% of the ultimate stress [38]. Demand was determined from a finite element model of the NZ-BRBF system, presented in Chapter 5. The resulting member sizes are shown in Tables 4.7 & 4.8.

Table 4.7: Boundary frame member sizes

Archetype ID	Level	VBE (Column)	HBE (Beam)
1S-LB-14	1	W14X74	W21X93
1S-LB-22	1	W14X90	W21X101
3S-LB-14	1	W14X109	W24X146
	2	W14X109	W24X131
	3	W14X109	W21X101
3S-LB-22	1	W14X145	W24X207
	2	W14X145	W24X176
	3	W14X145	W24X131
3S-ZZ-14	1	W14X109	W24X176
	2	W14X109	W24X146
	3	W14X109	W21X101
3S-ZZ-22	1	W14X145	W24X207
	2	W14X145	W24X176
	3	W14X145	W24X131

Table 4.8: Boundary frame member sizes (continued)

Archetype ID	Level	VBE (Column)	HBE (Beam)
6S-LB-14	1	W14X283	W24X207
	2	W14X283	W24X176
	3	W14X283	W24X146
	4	W14X176	W21X122
	5	W14X176	W18X97
	6	W14X176	W18X76
6S-LB-22	1	W14X283	W24X250
	2	W14X283	W24X229
	3	W14X283	W24X192
	4	W14X176	W21X147
	5	W14X176	W18X106
	6	W14X176	W18X76
9S-LB-14	1	W14X550	W24X250
	2	W14X550	W24X207
	3	W14X550	W24X176
	4	W14X500	W24X162
	5	W14X500	W24X146
	6	W14X500	W21X132
	7	W14X145	W21X101
	8	W14X145	W18X76
	9	W14X145	W16X57
9S-LB-22	1	W14X550	W27X336
	2	W14X550	W27X307
	3	W14X550	W27X258
	4	W14X455	W24X192
	5	W14X455	W24X176
	6	W14X455	W21X147
	7	W14X132	W21X122
	8	W14X132	W18X86
	9	W14X132	W18X65

Chapter 5

Nonlinear Model Development

This chapter presents details of the nonlinear models used to design and analyze the NZ-BRB index archetype buildings. Nonlinear modeling and analysis was conducted with OpenSees, an open source finite-element software for earthquake engineering simulation [39]. OpenSees materials, elements, and other components used are italicized for emphasis.

5.1 General

In order to simplify analysis, each archetype building was idealized as a two-dimensional plane-frame model, in line with previous P-695 BRBF studies [4]. Two frames were modeled, with opposing direction braces, and a P-Δ leaning column was included to represent the P-Δ effects from the building's gravity columns. The P-Δ columns were modeled as *elasticBeamColumn* elements with large axial stiffness, small rotational stiffness, and a *PDelta* geometric transformation. For boundary conditions, the frame columns were fixed at the base with a moment-release at the first floor midpoint, and the first floor BRB were assumed to be pinned at the base. The foundation collector beam, shown in Figure 1.1, was not modeled, assuming it to be essentially rigid. The boundary conditions of the NZ-BRBF system and the P-Δ column configuration for a LB configuration frame are shown in Figure 5.1.

Frame configuration was based on the NewZ-BREAKSS top-flange rocking beam detail proposed by Dowden et al. (2014) [27], but with a few modifications. A schematic of the finite element model used is shown in Figure 5.2, where circles represent nodes, and lines represent elements or constraints, numbered according to their type.

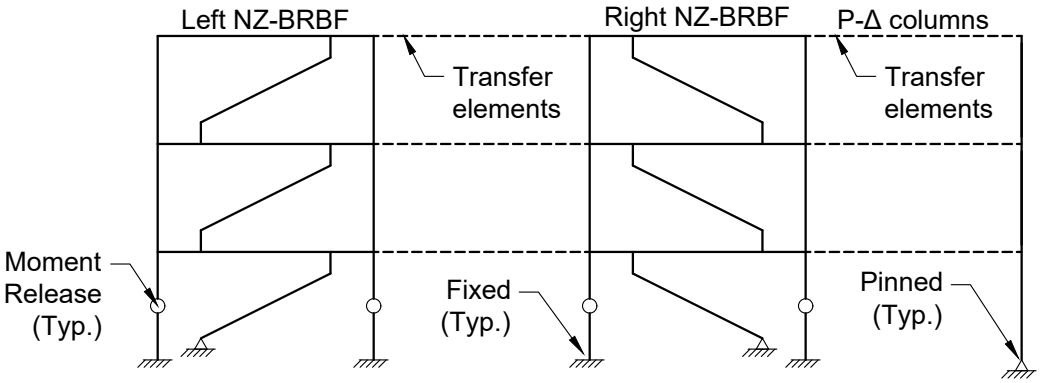

Figure 5.1: Boundary conditions and P-Δ column configuration

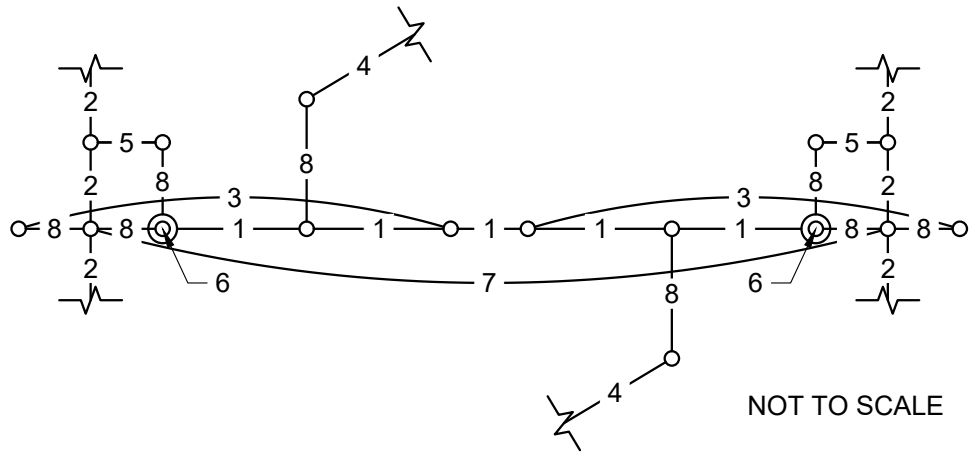

LEGEND:

1:	Horizontal boundary elements (HBE)	5:	Compression-only spring elements
2:	Vertical boundary elements (VBE)	6:	Shear plate elements
3:	Post-tensioning elements (PT)	7:	Rigid diaphragm element
4:	Buckling restrained braces (BRB)	8:	Rigid beam offset constraints

Figure 5.2: NZ-BRBF connectivity (LB configuration)

5.2 Boundary Frame Elements

The boundary frame elements were modeled with *forceBeamColumn* elements, using a *Linear* geometric transformation for the HBEs and, to capture second order effects, a *PDelta* geometric transformation for the VBEs.

Although the NZ-BRBF boundary frame was designed to remain essentially elastic, some yielding of the boundary frame members may occur, especially at collapse-level ground motions. Therefore, to capture the softening in the frame elements, fiber sections representing the steel wide-flange sections were used with a distributed plasticity Lobotto integration scheme with five integration points. The individual fibers in the fiber section were modeled with *Steel01* material with 2% kinematic strain hardening [13].

5.2.1 Validation of HBE Kinematic Equations

Figures 5.3, 5.4, & 5.5 compare the kinematic equations for axial, shear, and moment HBE force demands to the demand from the OpenSees numerical model subjected to a column rotation θ of 0.04 rad. The demand on the HBE was computed from the kinematic equations assuming the fully developed brace forces For brevity, only the 3-story archetypes with 22 strands are shown, and for the right-ward drift load case in Eq. (4.3-3). The results from the rigid OpenSees model are nearly identical to the rigid kinematic equations, and are larger in magnitude than the flexible OpenSees model results. While the archetypes were not designed directly from the kinematic equation demands, but rather the demand from a 4% roof drift static pushover analysis, these plots serve to validate both the kinematic equations and the numerical model.

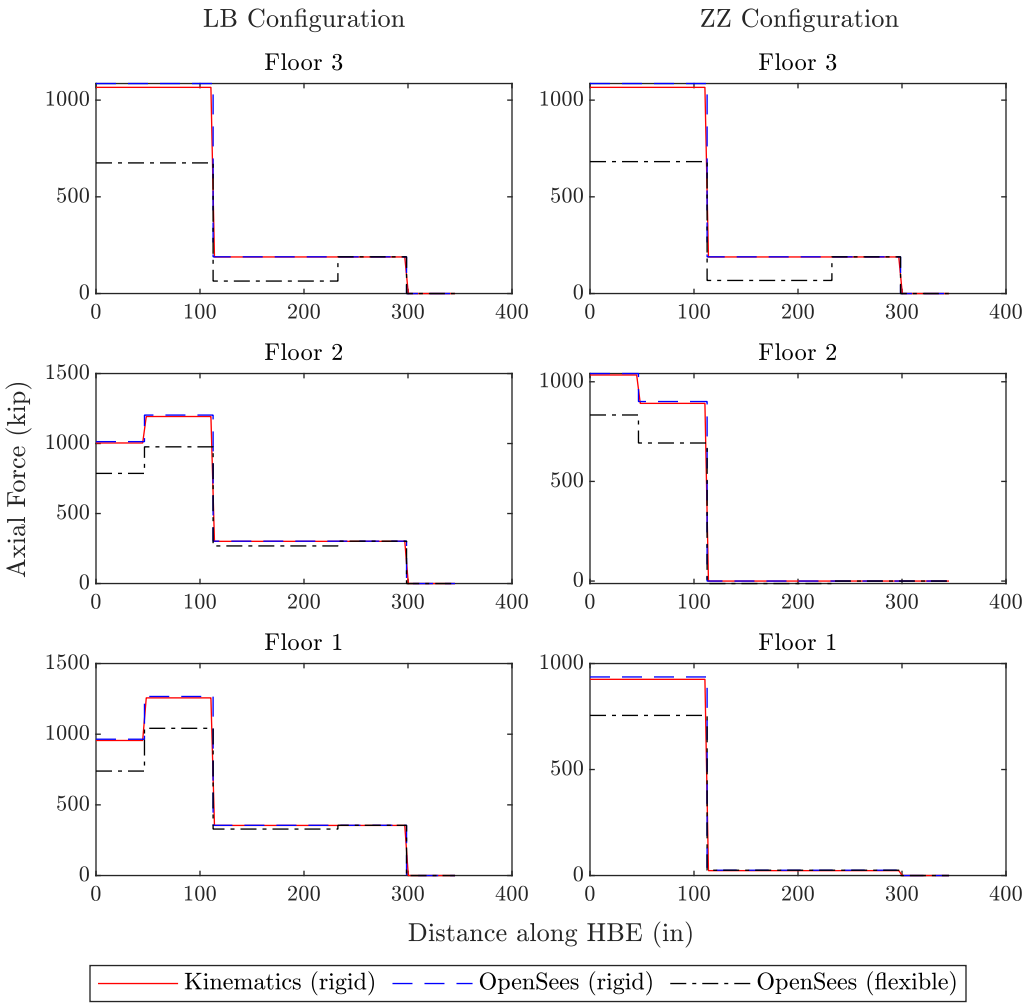

Figure 5.3: HBE axial force comparison

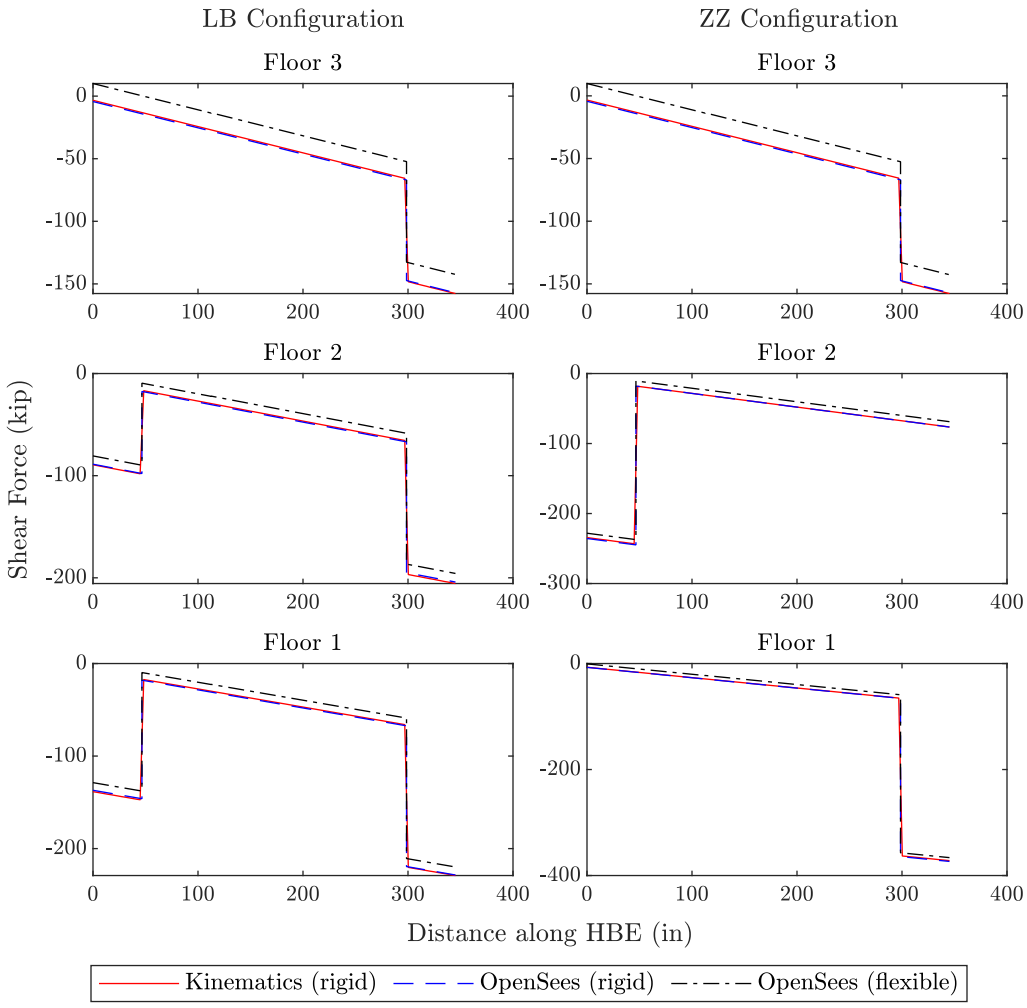

Figure 5.4: HBE shear force comparison

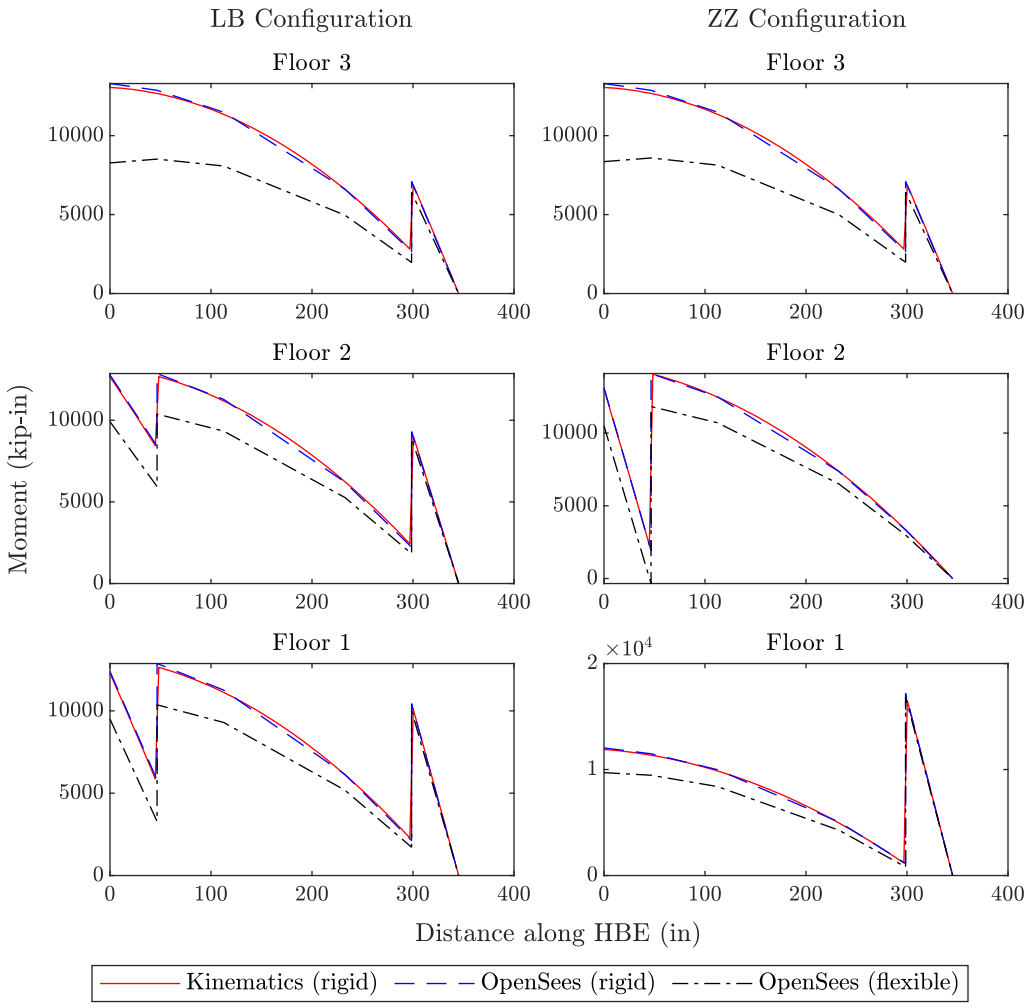

Figure 5.5: HBE moment comparison

5.3 Post-Tensioning (PT)

Post-tensioning (PT) elements were modeled as tension-only truss elements, connected to the HBE centerline directly and to the VBE via a rigid offset, and with an area equal to the number of strands times the area of each strand. The stress-strain response of the PT elements was modeled with an *ElasticPPGap* material, using an elastic modulus of 29000 ksi and a yield stress of 243 ksi, which is equal to 90% of the ultimate stress of the PT [38]. Although experimental tests have demonstrated that PT strands exhibit some strain hardening [40], the post-yield stiffness of the PT elements was conservatively assumed to be zero. No initial gap was used for the *ElasticPPGap* material, and the "damage" flag was enabled, allowing for gap growth if the PT yields. Finally, the *ElasticPPGap* material was wrapped with the *InitStressMaterial* uniaxial material wrapper to apply the initial PT stress.

5.3.1 Accounting for PT Loss

If the reacting structure is not infinitely rigid, the initial PT forces will cause the reacting structure to deform, in turn reducing the applied initial PT forces. Previous studies have accounted for this PT loss phenomenon by iteratively changing initial PT stress/strain until final stresses are within a tolerance of the target [17], or by developing an analytical equation for the required initial strain that incorporates the known stiffnesses of the reacting elements [1], [22]. This study proposes a new method, presented in Algorithm 1, to account for PT loss in the model, in which the initial stress/strain values are unchanged. The proposed method simply removes and restores the PT elements until the stress losses after an equilibrium analysis drop below an acceptable tolerance. This method works with truss elements in OpenSees, which are applied at the displaced location, rather than the initial location, of the end points.

Algorithm 1 Iterative method for applying post-tensioning elements

repeat
    remove and restore PT elements
    perform static equilibrium analysis
until stress losses are acceptable

5.4 Buckling Restrained Braces

The BRBs were modeled with *corotTruss* elements as single prismatic trusses representing the BRB components in series, with assumed detailing ratios of $\lambda_A = 0.5$, $\lambda_B = 0.7$, and $\lambda_C = 0.85$, which corresponds to a stiffness modifier f_{SM} of about 1.54. In order for the prismatic truss to have the same stiffness as the components in series, an effective area was used, computed with Eq. (3.1-11), and the elastic modulus was taken to the be the elastic modulus of the core material (29000 ksi). The yield stress of the BRB core material was assumed to be the same in tension and compression, and was taken to be the median specified yield stress of 42 ksi. However, in order for the prismatic truss with an effective area to have the same yield force as the components in series, an effective yield stress was used, computed with Eq. (3.1-13).

The main hysteretic response of the BRBs was modeled using the *SteelMPF* material, due to its simple implementation of asymmetric isotropic and kinematic strain hardening, which was used to calibrate the material to typical BRB backbone curves. Low-cycle fatigue and strain limits were included using the *Fatigue* material wrapper, and calibrated to published test data, adjusting for the geometry of the BRB. The resulting BRB model captures the stiffness, capacity, hardening, and failure behavior of typical BRBs.

5.4.1 SteelMPF Material

The main hysteresis of the BRB braces was modeled using the *SteelMPF* material in OpenSees [41]. This material uses a nonlinear hysteretic material model developed by Menegotto and Pinto 1973 [42], with isotropic strain hardening as proposed by Filippou et al. 1983 [43].

The isotropic hardening formulation in *SteelMPF* relates the expansion of the yield envelope to the minimum and maximum strains, as proposed by Filippou et al. 1983 [43]. Although *SteelMPF* accepts four isotropic hardening parameters (a_1, a_2, a_3, and a_4), this study assumes a_2 and a_4 to be equal to 1, and considers parameter a_1 to be the isotropic hardening ratio in compression, or a_c, and a_3 to be the isotropic hardening ratio in tension, or a_t. With this simplification, the adjusted yield stresses in compression and tension, $\sigma_{y,c}$ and $\sigma_{y,t}$, can be calculated according to Eqs. (5.4-1) and (5.4-2):

$$\sigma_{y,c} = -\sigma_{y,0}\left(1 + a_c\left(\frac{\varepsilon_{max}}{\varepsilon_y} - 1\right)\right) \leq -\sigma_{y,0} \tag{5.4-1}$$

$$\sigma_{y,t} = \sigma_{y,0}\left(1 + a_t\left(\frac{-\varepsilon_{min}}{\varepsilon_y} - 1\right)\right) \geq \sigma_{y,0} \tag{5.4-2}$$

where,

$\sigma_{y,c}$	=	Hardened yield stress in compression
$\sigma_{y,t}$	=	Hardened yield stress in tension
$\sigma_{y,0}$	=	Initial yield stress
a_c	=	Isotropic hardening ratio in compression
a_t	=	Isotropic hardening ratio in tension
ε_{max}	=	Maximum strain
ε_{min}	=	Minimum strain
ε_y	=	Initial yield strain

The kinematic hardening parameters, on the other hand, are simply the ratios of post-yield stiffness to elastic stiffness: b_t for tension and b_c for compression.

In lieu of test data, the isotropic and kinematic strain hardening parameters were chosen to match a typical BRB backbone curve, as shown in Figure 5.6, using Eqs. (5.4-3) and (5.4-4). The backbone curve defines the overstrength of the brace in tension and compression at the expected brace ductility, μ, which corresponds to the brace ductility at twice the design story drift [34]. Assuming a design story drift of 2%, the expected story drift is 4%. With this expected story drift, the expected brace ductility was about 17 for all the considered building configurations, calculated using Eq. (3.1-35). The overstrength at the expected brace ductility was then defined by overstrength factors ω and β. The values used for index archetype design, $\omega = 1.4$ and $\beta = 1.1$, were used, and isotropic and kinematic strain hardening parameters were selected to meet the target overstrength factors.

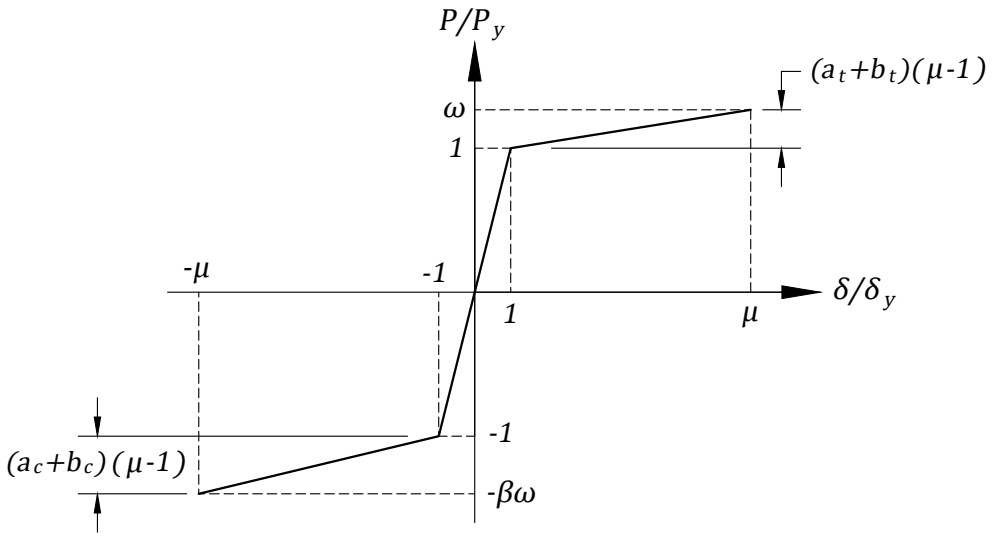

Figure 5.6: BRB hysteresis backbone overstrength factors

$$a_t + b_t = \frac{\omega - 1}{\mu - 1} \tag{5.4-3}$$

$$a_c + b_c = \frac{\beta\omega - 1}{\mu - 1} \tag{5.4-4}$$

However, because many combinations of isotropic and kinematic strain hardening parameters can result in the same overstrength factors, the relative proportions of isotropic and kinematic hardening were informed from BRB component testing [29]. Therefore, isotropic strain hardening was assumed to be 2.0% in both tension and compression, and kinematic hardening was assumed to be 0.5% in tension and 1.4% in compression. These parameters corresponded to $\omega \approx 1.4$ and $\beta \approx 1.1$ for all archetype configurations.

In addition to modeling the yield point and strain hardening, the *SteelMPF* material includes a Bauschinger effect transition from elastic to plastic, controlled by the parameters R_0, c_{R1}, and c_{R2}. Although the recommended values are 20, 0.95, & 0.15, these values were calibrated to reinforcing steel, not BRB components [42]. Therefore, in order to better represent the behavior of BRBs, values calibrated to BRB component tests were used instead: 25, 0.90, & 0.15 [29].

The resulting BRB material hysteresis is shown in Figure 5.7. This matches the specified BRB backbone, exhibits a combination of kinematic and isotropic hardening, and has a smooth transition from elastic to plastic. However, it does not have any degradation or strength limit. This is addressed by the use of the *Fatigue* wrapper material.

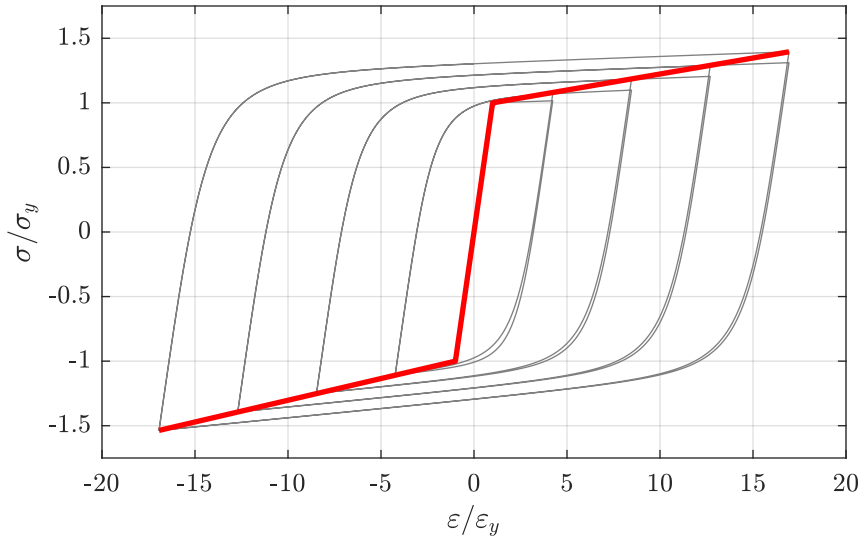

Figure 5.7: SteelMPF BRB hysteresis with backbone

5.4.2 Fatigue Material

Low cycle fatigue and strain limits were implemented in OpenSees using the *Fatigue* wrapper material. The default parameters for this material are $m = -0.458$ and $\varepsilon_0 = 0.191$. These values were calibrated with steel wide-flange sections, so they are not necessarily appropriate for BRBs [44]. Therefore, the slope of the Coffin-Manson curve, m, was kept at the default value, but the default value of strain at which one cycle will cause failure, ε_0, was converted from yielding core plastic strain to brace plastic strain, as shown in Eq. (5.4-5). For the ratio of core length to brace length $\lambda_C = 0.85$ this corresponds to $\varepsilon_0 = 0.16235$.

$$\varepsilon_0 = 0.191\lambda_C \tag{5.4-5}$$

In addition to the m and ε_0 parameters, a ductility limit was imposed on the BRBs with the "-max" and "-min" strain options for the *Fatigue* material. It was assumed that deformation levels greater than 30 times the yield deformation would lead to

failure of the braces, based on test results in the literature [5]. Therefore, a strain limit equal to 30 times the effective yield strain of the brace was used. With a brace detailing ratio λ_B of 0.7 and a stiffness modifier f_{SM} of 1.54, yield stress of 42 ksi and elastic modulus of 29000 ksi, this corresponds, using Eqs. (3.1-13) & (3.1-14), to a maximum effective brace strain of about 4%.

It is important to note that this is only an effective brace strain limit, and is not directly comparable to the yielding core strain limit. Because plastic strain are concentrated in the yielding core, and because the yielding core is shorter than the entire brace, the yielding core strain limit will be larger than the effective brace strain limit. Specifically, with the detailing ratios and material properties used in this study, the strain limit of the yielding core material $(\varepsilon_{yz})_{max}$ is approximately 4.7% for a maximum brace ductility of 30.

This approximate yielding core strain limit was calculated using Eq. (3.1-23), with the simplifying assumption that elastic strain contributions due to strain hardening are small. With this simplifying assumption, ε_y^* can be substituted for $\frac{\sigma_{brb}^*}{E_{brb}}$, and $30\varepsilon_y^*$ can be substituted for ε_{brb}^*, as shown in Eq. (5.4-6). Then, substituting Eq. (3.1-14) for ε_y^* and simplifying, the $(\varepsilon_{yz})_{max}$ can be expressed in terms of only the brace detailing ratios and yielding core material properties, as shown in Eq. (5.4-7). Finally, substituting the brace detailing ratios and material properties used for this study, the approximate yielding core strain limit is approximated as shown in Eq. (5.4-8).

$$(\varepsilon_{yz})_{max} \approx f_{SM}\lambda_B\varepsilon_y^* + \frac{1}{\lambda_C}(30\varepsilon_y^* - \varepsilon_y^*) \tag{5.4-6}$$

$$(\varepsilon_{yz})_{max} \approx \varepsilon_y\left(1 + \frac{29}{\lambda_B\lambda_C f_{SM}}\right) \tag{5.4-7}$$

$$(\varepsilon_{yz})_{max} \approx \frac{42 \text{ ksi}}{29000 \text{ ksi}}\left(1 + \frac{29}{0.7 \times 0.85 \times 1.54}\right) \approx 0.047 \tag{5.4-8}$$

5.5 NewZ-BREAKSS (NZ) Connection

The NZ connection model shown in Figure 5.2 consists of the top-flange rocking point offset from the HBE, and the slotted shear plate offset from the VBE. To represent the top-flange rocking point, a compression-only *truss* element was used, connected to the VBE centerline directly and to the HBE via a rigid offset. To represent the shear plate, a *zeroLength* element with a rigid force-deformation response in the vertical direction was used, connected to the HBE centerline directly and to the VBE via a rigid offset. Note that a rigid zero-length element was used in lieu of an equal degree-of-freedom constraint for the shear plate to avoid chained multi-point constraints.

5.6 Rigid Diaphragm Element

Seismic forces are typically applied to a frame model as point loads or point mass at the frame workpoints. This is a modeling assumption which typically does not make much of a difference for traditional braced frames. However, with the NZ-BRBF system, the beam-column connection is compression-only, so it cannot transfer the seismic forces in tension. Therefore, in order to apply seismic forces at the frame workpoints, the columns were restrained to have the effectively the same lateral displacement through the use of a rigid *truss* element. This additional element represents

a rigid diaphragm or similar mechanism, and, as a result of the unique kinematics of the NZ-BRBF system, effectively transfers all lateral forces to the opening joint side of the frame. In reality, load paths can vary with diaphragm and frame configuration, but this modeling assumption was adopted for its simplicity and for representing a worst-case load-path, as it maximizes the end-moment on the HBE.

5.7 Rigid Offsets (Multi-Point Constraints)

Rigid offsets in the NZ-BRB model were modeled with *rigidLink beam* multi-point constraints, and the *Transformation* constraint handler was used to condense out the constrained degrees-of-freedom. In order to avoid issues from over-constraining or chained multi-point constraints, all rigid offsets were oriented away from the element they were offset from.

5.8 Gravity Loads

Gravity loads tributary to the HBE were applied as element loads on the HBE, and additional gravity loads tributary to the frame were applied as point loads to the frame work-points. Gravity loads carried by the gravity system but tributary to the lateral frame for second-order effects were applied to a P-Δ leaning column.

For design of the boundary frame, the applicable load combinations in Eqs. (4.3-3) & (4.3-4) were used. For nonlinear static and nonlinear dynamic analysis however, the applicable gravity load combination specified for P-695 analysis was used instead:

$$1.05D + 0.25L \tag{5.8-1}$$

where D is the dead load and L is the live load of the structure. The nonlinear analysis load combinations differ from the design load combinations because while the archetype buildings must be designed according to code, the nonlinear analyses should capture the expected (median) behavior [3].

Chapter 6

Nonlinear Static (Pushover) and Eigenvalue Analysis

This chapter presents the results of the nonlinear static (pushover) and eigenvalue analysis results for the NZ-BRBF index archetype models, as specified in the P-695. The results of the nonlinear static and eigenvalue analyses serve to validate the numerical model, especially for first-mode behavior. Additionally, the nonlinear static results are used to calculate the overstrength and period-based ductility, which are used in the performance evaluation of the proposed SFRS.

6.1 Eigenvalue Results

After applying gravity loads with the load combination in Eq. (5.8-1) and applying the seismic masses to the frame workpoints, eigenvalue analyses were conducted on the index archetype models in OpenSees. Table 6.1 reports the fundamental period T, calculated using Eq. (4.5-1), the first mode period T_1 calculated from the eigenvalue analysis, and the coefficient C_0 relating MDOF roof displacement to equivalent SDOF displacement. The coefficient C_0, used later to calculate the period-based ductility μ_T, was calculated according to Eq. (6.1-1), where m_x is the mass at level x, $\phi_{1,x}$ is the lateral first-mode eigenvector value at level x, and n is the number of levels.

$$C_0 = \phi_{1,n} \frac{\sum_{x=1}^{n} m_x \phi_{1,x}}{\sum_{x=1}^{n} m_x \phi_{1,x}^2} \tag{6.1-1}$$

Table 6.1: First mode period T_1 and coefficient C_0

Archetype	T (sec)	T_1 (sec)	C_0
1S-LB-14	0.29	0.56	1.00
1S-LB-22	0.29	0.55	1.00
3S-LB-14	0.66	0.83	1.27
3S-LB-22	0.66	0.80	1.27
3S-ZZ-14	0.66	0.82	1.27
3S-ZZ-22	0.66	0.77	1.28
6S-LB-14	1.15	1.50	1.37
6S-LB-22	1.15	1.47	1.37
9S-LB-14	1.54	2.05	1.41
9S-LB-22	1.54	2.01	1.42

6.2 Lateral Load Distribution

Nonlinear static analysis was performed on the index archetype models in OpenSees with the *DisplacementControl* integrator, using the roof level lateral displacement as the controlling degree-of-freedom. Lateral loads were applied to the model in proportion to a lateral load distribution factor C_{vx}, as computed in Eq. (6.2-1), where m_x is the mass at level x, and $\phi_{1,x}$ is the first-mode eigenvector value at level x, and n is the number of stories.

$$C_{vx} = \frac{m_x \phi_{1,x}}{\sum_{i=1}^{n} m_i \phi_{1,i}} \tag{6.2-1}$$

The resulting lateral load distributions for each index archetype model are shown in Figures 6.1, 6.2, and 6.3.

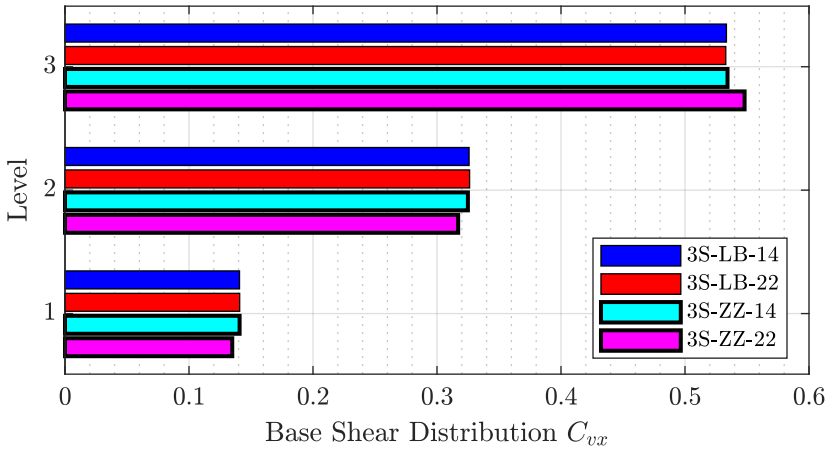

Figure 6.1: Nonlinear static lateral load distribution for 3-story archetypes

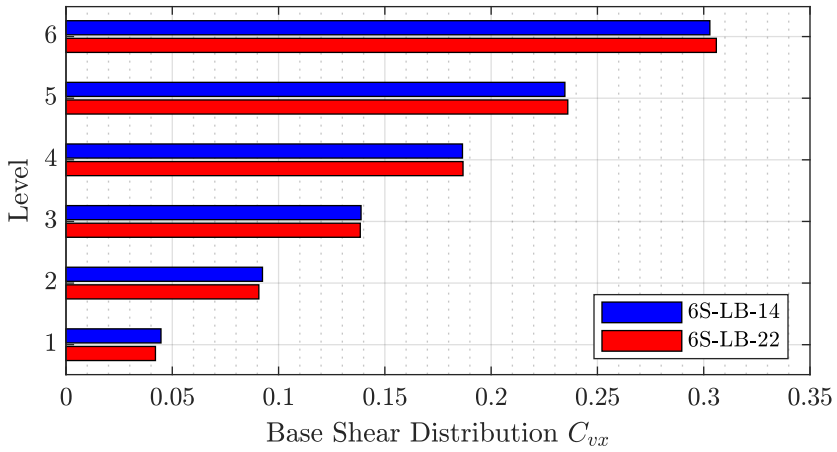

Figure 6.2: Nonlinear static lateral load distribution for 6-story archetypes

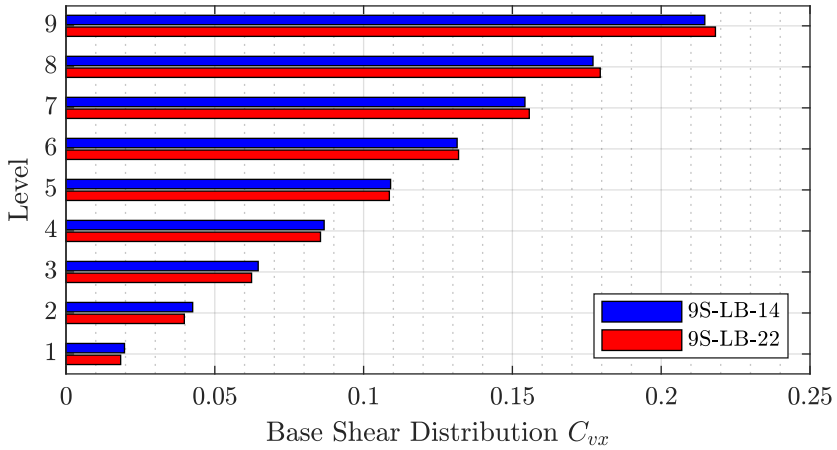

Figure 6.3: Nonlinear static lateral load distribution for 9-story archetypes

6.3 Roof Drift vs. Base Shear

The index archetypes were subjected to a displacement controlled monotonic pushover analysis in OpenSees, and the resulting roof drift vs. base shear plots were used for determining maximum base shear and ultimate roof displacement. For the pushover analyses, the maximum brace ductility limit $\mu_{max} > 30$ was ignored for assessment of maximum base shear, but was enforced in post-processing to determine the "ultimate" roof displacement δ_u. This was done to provide a conservative upper bound on overstrength, while also not overestimating the system ductility.

6.3.1 1-Story Archetypes

The roof drift vs. base shear plots for the 1-story archetypes are shown in Figure 6.4. Note the bilinear post-yield stiffness, which is a result of the unique NZ boundary frame kinematics.

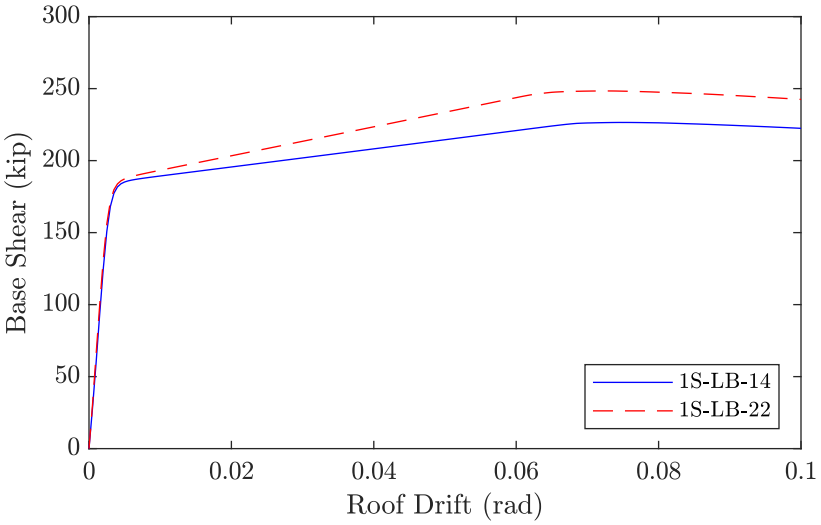

Figure 6.4: Pushover curves for 1-story archetypes

6.3.2 3-Story Archetypes

The roof drift vs. base shear plots for the 3-story archetypes are shown in Figure 6.5. There is little difference between the two brace configurations for base shear response, and the base shear response does not degrade significantly.

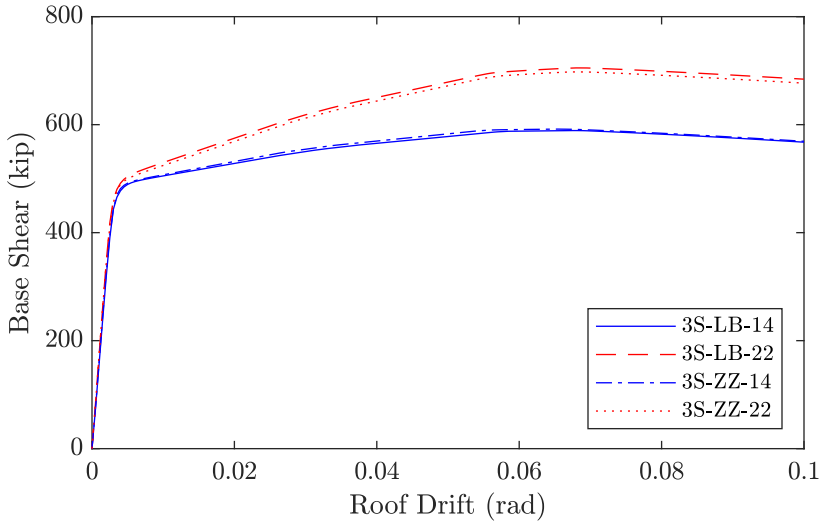

Figure 6.5: Pushover curves for 3-story archetypes

6.3.3 6-Story Archetypes

The roof drift vs base shear plots for the 6-story archetypes are shown in Figure 6.6. Unlike the 3-story archetypes, which did not exhibit substantial base shear degradation, the 6-story archetypes exhibited modest base shear degradation, with the 14 strand archetype degrading more.

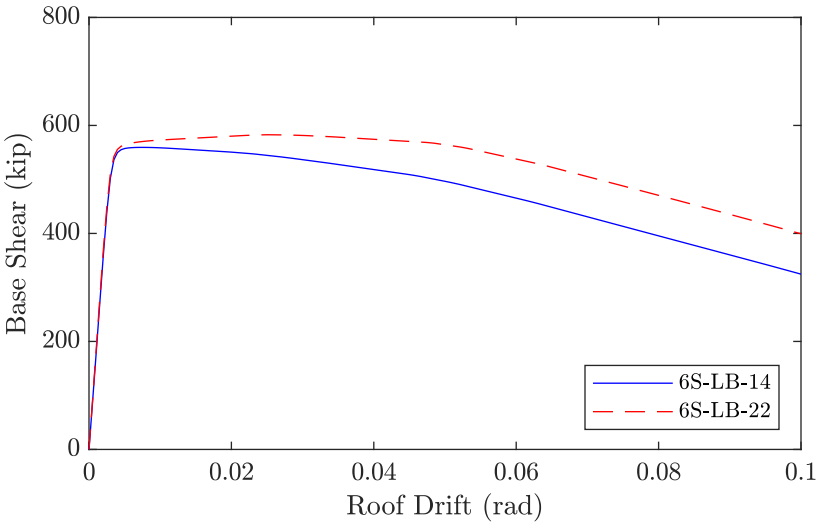

Figure 6.6: Pushover curves for 6-story archetypes

6.3.4 9-Story Archetypes

The roof drift vs. base shear plots for the 6-story archetypes are shown in Figure 6.7. Similar to the 6-story archetype results, the archetype with more PT strands had reduced base shear degradation.

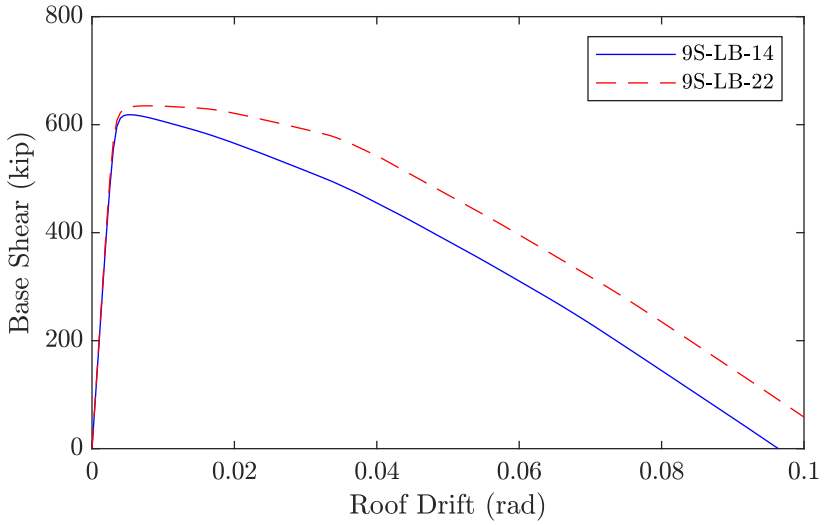

Figure 6.7: Pushover curves for 9-story archetypes

6.4 Determination of Overstrength and Period-based Ductility

Following the P-695 methodology, index archetype overstrength Ω was calculated according to Eq. (6.4-1) as the ratio of maximum base shear V_{max} to design base shear V.

$$\Omega = \frac{V_{max}}{V} \tag{6.4-1}$$

The system overstrength Ω_O was then determined as the largest index archetype Ω, rounded up to the nearest half increment (0.5).

Period based ductility μ_T, which is used by the P-695 methodology to adjust collapse capacity, was calculated as the ratio of ultimate roof displacement δ_u to the effective yield roof drift displacement $\delta_{y,eff}$, as shown in Eq. (6.4-2).

$$\mu_T = \frac{\delta_u}{\delta_{y,eff}} \tag{6.4-2}$$

Ultimate roof displacement was taken as either the displacement where brace ductility μ_{max} exceeded 30, or where the base shear dropped below 80% of V_{max}, whichever occurred first.

The effective yield roof displacement $\delta_{y,eff}$ is calculated according to Eq. 6.4-3, where C_0 is the coefficient calculated according to Eq. (6.1-1), W is the building weight tributary to the frame and the P-Δ leaning column, g is gravitational acceleration, T is the fundamental period calculated according to Eq. (4.5-1), and T_1 is the first mode period of the index archetype model as computed from an eigenvalue analysis.

$$\delta_{y,eff} = C_0 \frac{V_{max}}{W} \left(\frac{g}{4\pi^2}\right) (\max(T, T_1))^2 \tag{6.4-3}$$

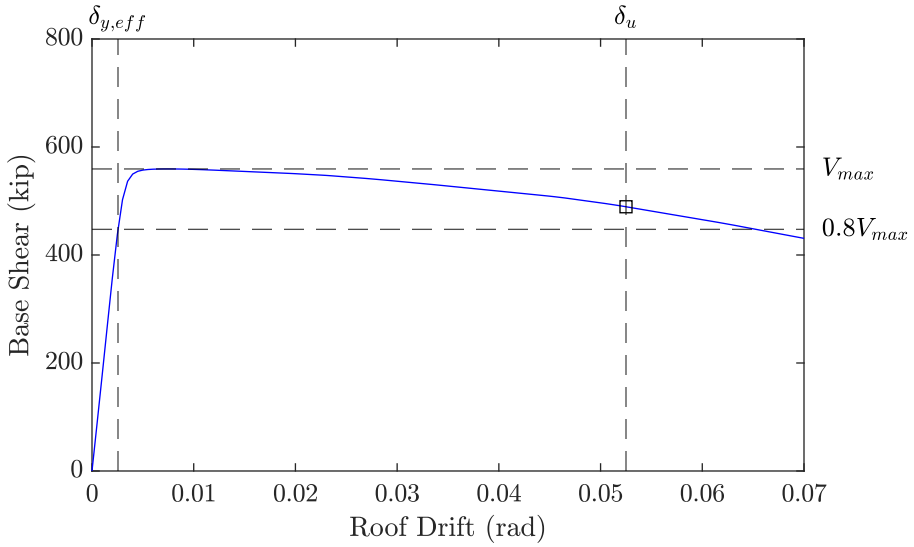

Figure 6.8: Pushover for index archetype 6S-LB-14, with labels

To illustrate the significance of the quantities maximum base shear, ultimate displacement, and effective yield roof displacement, the roof drift vs. base shear plot for index archetype 6S-LB-14 is labeled with the corresponding quantities in Figure 6.8. Note that for this archetype, the ultimate displacement is not taken as the point where the base shear degrades below 80% of V_{max}. Instead, the ultimate displacement for this archetype is taken as point where the brace ductility μ_{max} exceeded 30. For most index archetype models, the brace ductility limit $\mu_{max} > 30$ was reached prior to the 80% V_{max} threshold. Therefore, if component testing data supported a higher brace ductility limit, the resulting ultimate roof displacement values could be higher, and in turn, the seismic performance evaluation could be more favorable. However, in the absence of a comprehensive experimental testing program, the ductility limit of 30 was used to be comparable to existing studies [5]. This limitation in the study is reflected in the test data quality ratings for the performance evaluation of the system.

The nonlinear static analysis results for all index archetypes are tabulated in Table 6.2. The largest index archetype overstrength was 1.90, so an appropriate value for system

Table 6.2: Nonlinear static analysis results

Archetype	V (kips)	V_{max} (kip)	Ω	δ_u (in)	$\delta_{y,eff}$ (in)	μ_T
1S-LB-14	142.57	226.51	1.59	11.47	0.62	18.55
1S-LB-22	142.57	248.39	1.74	11.54	0.64	18.03
3S-LB-14	371.75	589.05	1.58	28.55	1.55	18.43
3S-LB-22	371.75	705.07	1.90	28.31	1.72	16.48
3S-ZZ-14	371.75	591.77	1.59	28.55	1.52	18.83
3S-ZZ-22	371.75	697.63	1.88	28.31	1.60	17.66
6S-LB-14	432.06	559.34	1.29	52.79	2.55	20.73
6S-LB-22	432.06	582.76	1.35	53.78	2.56	21.04
9S-LB-14	482.97	618.33	1.28	49.04	3.62	13.55
9S-LB-22	482.97	634.89	1.31	62.95	3.57	17.65

overstrength Ω_O is 2.0. For all archetypes, more PT resulted in larger maximum base shear. More PT also generally increased the ultimate displacement and effective yield displacement, although not for all archetypes. The brace configuration did not have much of an effect, with the LB and ZZ configuration archetypes having similar system overstrengths and period-based ductilities.

6.5 Story Drift Ratios

To help gauge system behavior, the story drift ratios for multi-story index archetype models are presented for design base shear V, the maximum base shear V_{max}, and at the ultimate roof displacement δ_u.

For all multi-story archetypes, the story drift profiles were typical of a single-curvature displacement profile, with the exception that the first floor drift demand was about 50% of the second floor drift demand, due to the mid-height column hinge detail. The archetypes with 22 strands generally had increased drift capacity, and the brace configuration parameter had little effect, which aligns with the results tabulated in Table 6.2.

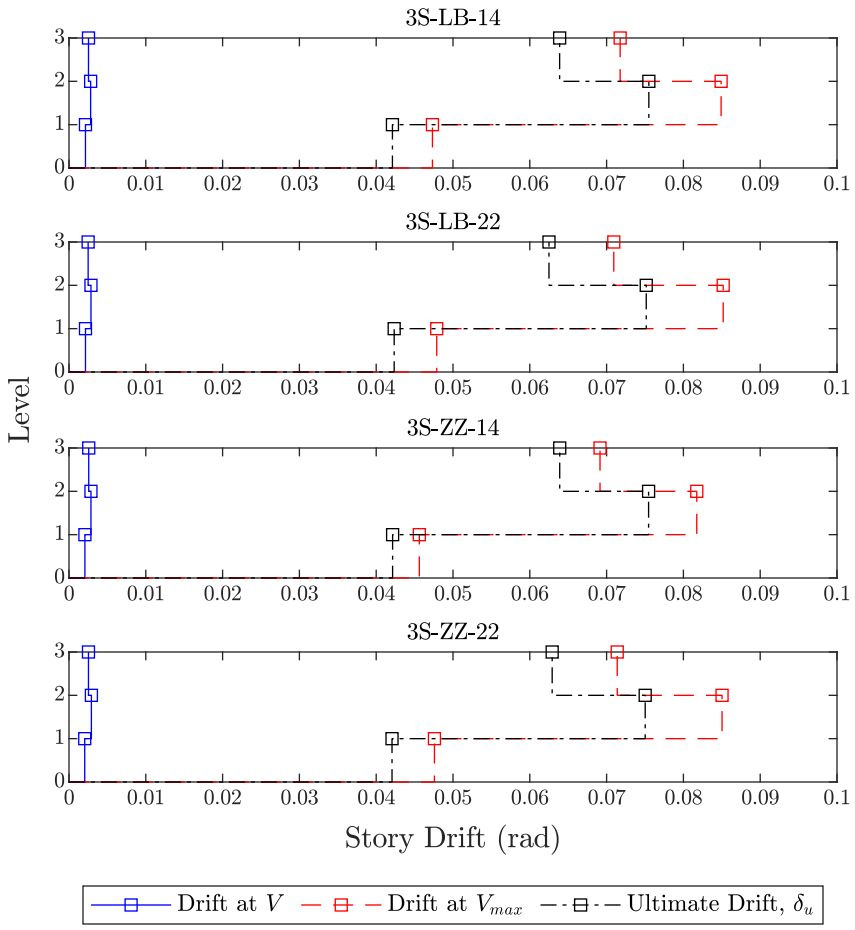

Figure 6.9: Pushover story drift profiles for 3-story archetypes

It is important to note that the 3-story archetype story drift profile plots in Figure 6.9 show that the story drift at maximum base shear is larger than the story drift at ultimate roof displacement. This is because for the 3-story archetypes, the brace ductility limit was reached prior to maximum base shear. Therefore, the story drifts at maximum base shear for the 3-story archetypes should not be taken as a realistic estimate of story drift demands, because they are beyond the brace ductility limits.

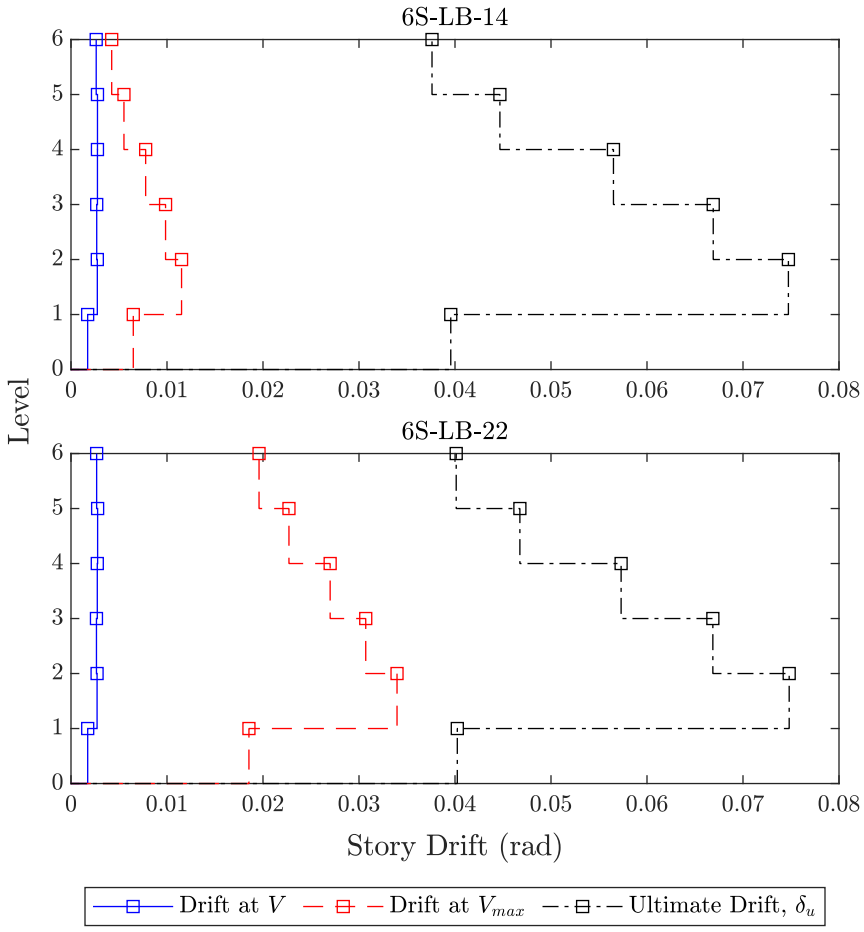

Figure 6.10: Pushover story drift profiles for 6-story archetypes

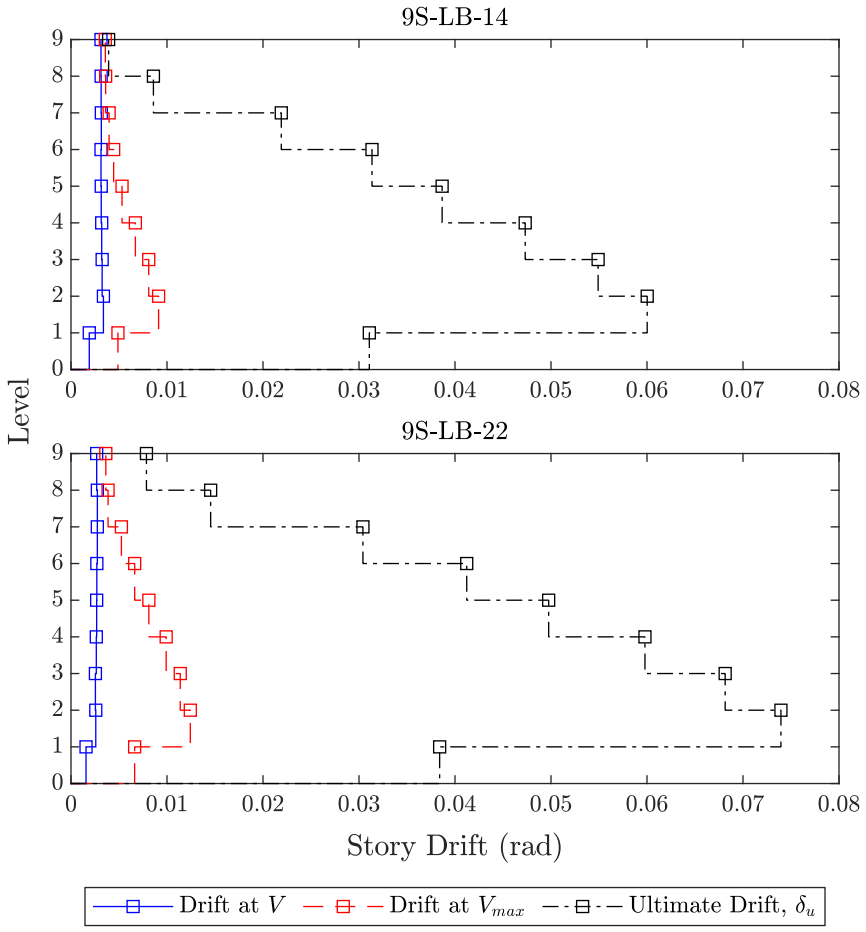

Figure 6.11: Pushover story drift profiles for 9-story archetypes

Chapter 7

Nonlinear Dynamic Analysis

This chapter presents the results of the nonlinear dynamic analyses for the NZ-BRBF index archetype models, using the P-695 Far Field Set ground motion suite, and subjected to Design Basis Earthquake (DBE) and Maximum Considered Earthquake (MCE) intensities. The resulting structural responses are used to gauge system behavior and compare against other BRBF systems.

7.1 Ground Motion Suite

Nonlinear response history analyses were conducted with the P-695 far field ground motion suite. The P-695 far-field set was developed for collapse assessment of buildings, and consist of 22 component pairs of horizontal ground motions from 14 different strong-motion earthquake events. In particular, the far-field set are ground motions from sites located greater than or equal to 10 km from fault rupture. Both horizontal components from each ground motion are used, for a total of 44 ground motion acceleration records, sufficient for meaningful statistical analysis. Most of the P-695 records were acquired from the PEER NGA-West2 database [45], but the Cape Mendicino record was obtained from the CESMD database [46], [47] (for the reason that this record was missing in the PEER database). Table 7.1 summarizes some details about the individual ground motions, and Figure 7.1 shows the unscaled acceleration response spectra of the ground motion suite.

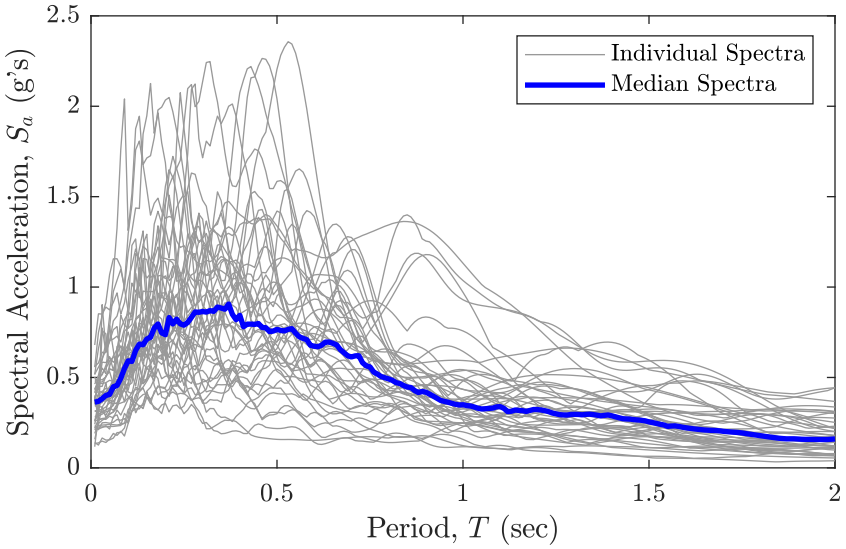

Figure 7.1: Response spectra for unscaled ground motion suite

Table 7.1: P-695 ground motion suite

ID	RSN	Earthquake	Station	Year	Mag.	Duration (sec)
1	953	Northridge	Beverly Hills - Mulhol	1994	6.7	29.98
2	960	Northridge	Canyon Country-WLC	1994	6.7	19.98
3	1602	Duzce, Turkey	Bolu	1999	7.1	55.89
4	1787	Hector Mine	Hector	1999	7.1	45.30
5	169	Imperial Valley	Delta	1979	6.5	100.14
6	174	Imperial Valley	El Centro Array #11	1979	6.5	39.07
7	1111	Kobe, Japan	Nishi-Akashi	1995	6.9	40.95
8	1116	Kobe, Japan	Shin-Osaka	1995	6.9	40.95
9	1158	Kocaeli, Turkey	Duzce	1999	7.5	27.18
10	1148	Kocaeli, Turkey	Arcelik	1999	7.5	30.00
11	900	Landers	Yermo Fire Station	1992	7.3	43.98
12	848	Landers	Coolwater	1992	7.3	28.00
13	752	Loma Prieta	Capitola	1989	6.9	39.99
14	767	Loma Prieta	Gilroy Array #3	1989	6.9	39.98
15	1633	Manjil, Iran	Abbar	1990	7.4	53.50
16	721	Superstition Hills	El Centro Imp. Co.	1987	6.5	59.99
17	725	Superstition Hills	Poe Road (temp)	1987	6.5	22.29
18	829	Cape Mendocino	Rio Dell Overpass	1992	7.0	59.98
19	1244	Chi-Chi, Taiwan	CHY101	1999	7.6	90.00
20	1485	Chi-Chi, Taiwan	TCU045	1999	7.6	90.00
21	68	San Fernando	LA - Hollywood Stor FF	1971	6.6	79.44
22	125	Friuli, Italy	Tolmezzo	1976	6.5	36.38

7.1.1 Ground Motion Normalization

In order to reduce record-to-record variability (e.g., due to event magnitude, distance to source, site conditions, etc.) between records without significantly affecting the overall record-to-record variability, the P-695 Far Field record set was normalized by peak ground velocity (PGV) using the PGV_{PEER} values reported in the PEER NGA database. The normalization factor for each ground motion is calculated as the median PGV_{PEER} of the ground motion suite divided by the i^{th} ground motion PGV_{PEER}. These normalization factors (NF) are published in the P-695. However,

the published ground motion normalization factors were based off of an outdated version of the PEER ground motion database. While the P-695 does claim that the published normalization factors should be valid for the current database version, this statement was made in regard to version 7.3 versus version 6.0 of the PEER NGA-West database. Since then, the NGA-West database has been replaced by the NGA-West2 database [45]. This next-generation of the database uses different attenuation functions for processing raw ground motion data, potentially leading to differences in the records compared to those used in the NGA-West database [48].

Therefore, to maintain the methodology while using updated ground motion records, new normalization factors (NF) based on NGA-West2 PGV values were computed, with the exception of ground motion 18, or RSN 829, which was not included in the NGA-West2 database. This missing ground motion was imputed with the matching record from the CESMD database and the older PGV value from the NGA-West database [49], [50]. Comparison of ground motion properties reported in the P-695 and those computed with the new ground motions are shown in Table 7.2 and Figure 7.2.

On average, the new normalization factors increased by 5%. The largest change was with record 8, which increased by 35%. Using the new normalization factors, each ground motion was amplitude scaled using their corresponding normalization factors. Computed response spectra and the median response spectra are shown in Figure 7.3.

Table 7.2: Ground motion normalization factor comparison

	PGV_{PEER} (cm/s)		Normalization Factor	
ID	Old	New	Old	New
1	57.2	59.81	0.65	0.68
2	44.8	45.16	0.83	0.90
3	59.2	62.90	0.63	0.64
4	34.1	34.78	1.09	1.17
5	28.4	26.95	1.31	1.50
6	36.7	40.77	1.01	0.99
7	36	39.49	1.03	1.03
8	33.9	27.11	1.1	1.49
9	54.1	56.11	0.69	0.72
10	27.4	31.14	1.36	1.30
11	37.7	40.26	0.99	1.01
12	32.4	33.22	1.15	1.22
13	34.2	38.85	1.09	1.04
14	42.3	43.52	0.88	0.93
15	47.3	49.48	0.79	0.82
16	42.8	43.67	0.87	0.93
17	31.7	33.89	1.17	1.20
18	45.4	47.95*	0.82	0.84
19	90.7	91.28	0.41	0.44
20	38.8	45.96	0.96	0.88
21	17.8	20.47	2.1	1.98
22	25.9	24.78	1.44	1.63

*Value from NGA-West database

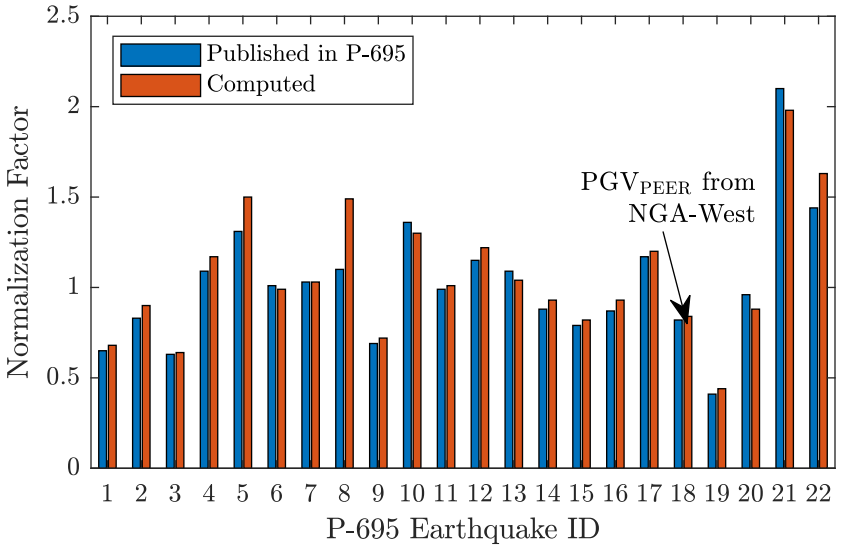

Figure 7.2: Comparison of normalization factors for the P-695 Far-Field record set

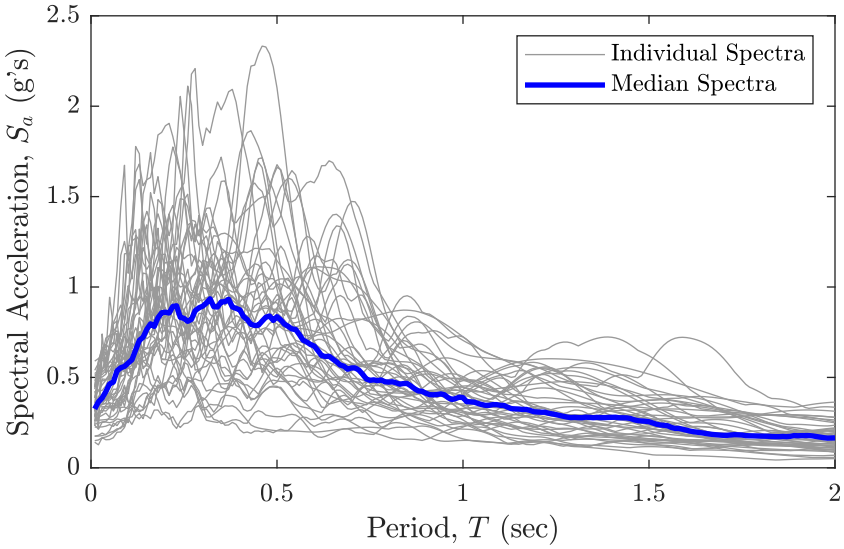

Figure 7.3: Response spectra for normalized ground motion suite

7.1.2 Ground Motion Scaling

The P-695 evaluates collapse performance relative to the Maximum Considered Earthquake (MCE) spectra, i.e. the Risk-Targeted Maximum Considered Earthquake (MCE_R) spectra as it is referred to in the ASCE 7 [33]. The target spectra is shown in Figure 7.4.

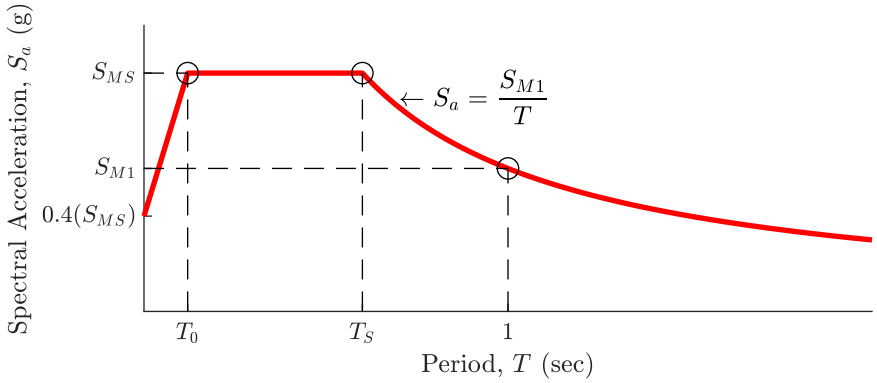

Figure 7.4: MCE target spectra

This target spectra is calibrated to a target conditional probability of collapse (e.g. 10% probability of collapse for typical structures, given an MCE level ground motion), so comparison of collapse fragility curves from an IDA can be used to directly evaluate the MCE target probability of collapse.

In order to assess the seismic collapse capacity of a system, the ground motions used must represent collapse-level earthquakes. However, strong ground motion data is limited, so, instead, ground motion records are typically amplitude scaled. Amplitude scaling introduces bias, overestimating the nonlinear structural responses and collapse probabilities [51], [52]. This is because the spectral shape of strong ground motions is usually peaked at the period of interest. Therefore, if a ground motion with a trough

at the period of interest is scaled up to match a target spectral value, unrealistic spectral responses may result at the other periods.

In part, the P-695 methodology handles amplitude scaling bias by anchoring the ground motion suite median response spectra (versus anchoring individual ground motion response spectra) to the target response spectra at a fundamental building period of interest. In this way, a more natural variation in spectral shape is retained. To illustrate this for a fundamental period of one second, the ground motion suite is anchored to a target response spectra individually and collectively (based on median spectra) in Figure 7.5 and Figure 7.6, respectively. When anchoring the median response spectra, the spectral values of the suite are scattered around the target spectral value at the period of interest, rather than the "pinching" effect characteristic of anchoring each ground motion individually. For this study, the P-695 methodology was followed and the median response spectra was used for anchoring the ground motion suite.

The target MCE spectral intensity S_{MT}, the median spectral intensity $\hat{S}_{NT}$, and the corresponding scale factor SF_{MT} used for anchoring the normalized ground motion suite to the MCE level intensity are tabulated in Table 7.3 for each building height.

Table 7.3: Scale factors used for anchoring the normalized ground motion suite to MCE target spectra

Stories	T (sec)	S_{MT} (g)	$\hat{S}_{NT}$ (g)	SF_{MT}
1	0.288	1.500	0.881	1.702
3	0.655	1.373	0.594	2.311
6	1.155	0.780	0.324	2.408
9	1.542	0.584	0.235	2.488

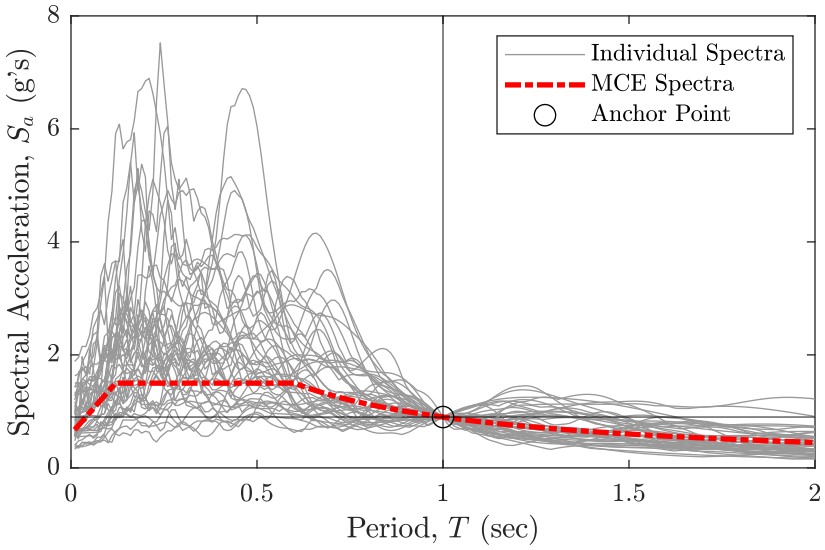

Figure 7.5: Anchoring ground motions individually

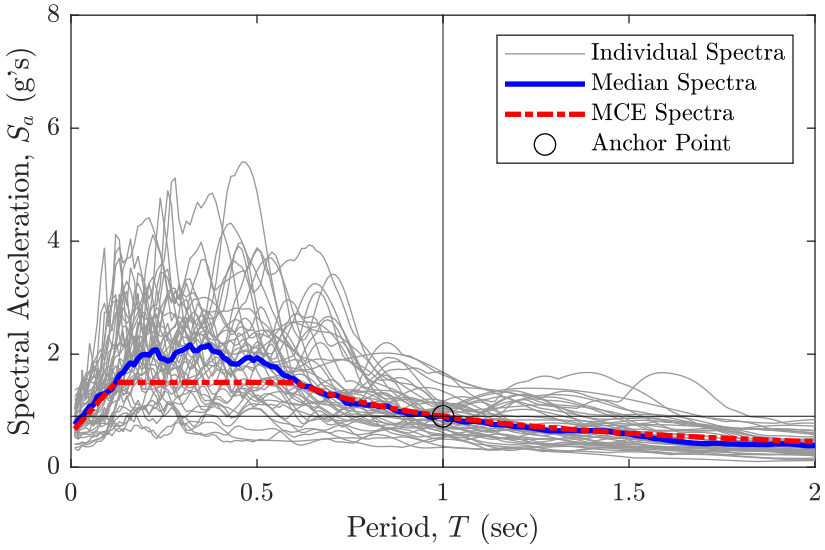

Figure 7.6: Anchoring ground motions collectively

7.2 Damping

Damping is the measure of energy dissipation in a dynamic system. In seismic design, the majority of the energy dissipation is designed to be due to hysteretic loops caused by yielding or friction elements. But, energy is also dissipated in the elastic region of the structural response, albeit to a lesser extent. This elastic energy dissipation is complex, caused by a variety of physical phenomena. So, while damping due to yielding is easily accounted for by hysteretic material models, mathematically equivalent viscous damping is usually used in lieu of modeling the complex physical sources of damping [53]. As a result, the governing equation of motion includes a velocity component with a damping coefficient, or, in MDOF systems, a damping matrix. Because there is no physical analogue to the damping ratio terms, the damping matrix is usually constructed as some combination of the mass and stiffness matrices. Mass-proportional damping tends to under-damp higher modes and stiffness-proportional damping tends to over-damp higher modes, while Rayleigh damping uses a linear combination of the mass and stiffness matrices with coefficients that ensure reasonable damping ratios at significant modes of interest [54]. Because of its flexibility in assigning damping to multiple modes, Rayleigh damping is commonly used, and is used in this study.

Equivalent viscous damping of steel structures has been measured experimentally and found to range from about 2-5% of critical, with taller structures typically having smaller damping ratios [55]. Previous analytical investigations of BRB systems have typically used Rayleigh damping of 2-5%, anchored to the first few modes of the structure [5], [37], [56], [57]. While damping up to 5% of critical has been used, increased damping has been shown to significantly reduce the nonlinear response [57].

Therefore, a critical damping ratio of 2% was adopted for this study. For models with only one mode of vibration, this was applied as stiffness proportional damping. Otherwise, Rayleigh damping was applied, anchored to the first and second modes.

7.2.1 Addressing Issues with Rayleigh Damping

Because Rayleigh damping has no real physical basis, unrealistic damping forces can result in some situations. For example, the use of the initial stiffness matrix in Rayleigh damping can result in spurious damping forces when the structure yields or undergoes drastic changes in stiffness, such as with contact or gap elements [58]. To address this, the tangential stiffness matrix can be used instead [59]. Then, when elements yield, the damping forces will decrease. However, tangential stiffness Rayleigh damping is an *ad hoc* approach, and can lead to unrealistic damping forces or convergence issues [58]. For example, in the case of negative post-yield stiffness, negative damping terms can result, and elements with significant discontinuities in stiffness can cause convergence issues. Therefore, elements posing problems with tangential stiffness damping should either be excluded from the damping matrix or have initial stiffness damping [4], [57]. Additionally, numerical stability issues can arise with using tangential stiffness damping with the Newmark integrator [59]. As an alternative, the Hilber-Hughes-Taylor (HHT) integrator can be used, which introduces a small amount of numerical damping [60]. Use of the HHT integrator with $\alpha = 0.9$ was found to be effective in accommodating the use of tangential stiffness damping without introducing a significant amount of numerical damping.

Therefore, the tangential stiffness matrix was used instead of the initial stiffness matrix, an HHT integrator with $\alpha = 0.9$ was used for the numerical solution, and damping was only applied to the BRB, PT and boundary frame elements, using the *region* command in OpenSees.

7.3 Nonlinear Response History Analyses (NRHA)

Nonlinear response history analyses (NRHAs) were conducted in OpenSees [39]. Each NRHA was padded with 30 seconds of free vibration, chosen to be consistent with other studies where residual displacement is a quantity of interest [13], [61], [62], and the actual residual displacements were determined by static equilibrium analysis after the 30 seconds of free vibration.

The time-step used for the NRHAs was taken to be the same as the ground motion record time step. Out of the 44 ground motion records, the largest time step was 0.02 seconds, which was determined to be sufficiently small for the significant modes of the index archetype models.

7.3.1 Collapse Criteria

In order to determine collapse in an NRHA, collapse criteria must be established. These collapse criteria can be simulated or non-simulated. Simulated collapse criteria utilize strength degradation within the numerical model, while non-simulated criteria impose limits on structural responses.

The P-695 methodology requires that all collapse mechanisms be either precluded by design requirements and assumptions, modeled directly to contribute to simulated collapse, or accounted for by non-simulated collapse criteria. Generally, simulated collapse is preferred, but some non-simulated collapse criteria are useful for imposing

realistic limits on the analysis. For the NZ-BRBF system, the main collapse mechanisms considered were brace failure, loss of post-tensioning, plastic hinging in the frame, and global instability due to P-Delta effects.

Brace failure was assumed to be limited to brace rupture due to fatigue or ultimate strain, and was modeled directly in *OpenSees* with the *Fatigue* material model and a ductility limit of 30. Connection failure was assumed to be precluded by the design requirements. Without proper connection detailing, BRB connections can fail at drift levels as low as 2%, but with proper detailing, such as stocky gusset plates and pinned connections, BRBs can achieve their component capacity [63]. Because the NZ-BRBF design requirements specify stiffened gusset plates and pinned connections, failure of the connections was not considered.

Loss of post-tensioning (PT) was assumed to be due to PT elongation, and was accounted for directly by modeling PT elements with the *ElasticPPGap* material model with the *damage* option turned on.

Potential plastic hinging in the frame was accounted for by using nonlinear beam column elements in the beams and columns, with the *Steel01* material model. Degradation was not considered, because the boundary frame is designed to be essentially elastic and the columns are pinned at the first floor midpoint.

Global instability due to P-Delta effects was accounted for by using a P-Delta leaning column with tributary gravity loads, and by imposing a non-simulated collapse criteria of 10% interstory drift. This non-simulated collapse condition was determined based on previous studies on steel frames [4], [30], [64], and drift capacity of wide-flange columns [65]. Although actual failure may occur at a smaller interstory drift, collapse capacity is not sensitive to large non-simulated collapse drift values, because dynamic instability occurs at large drifts [3].

7.3.2 Analysis Algorithm

When subjecting nonlinear finite element models to collapse-level ground motions, the numerical solution often fails to pass convergence tests. While one could decrease the time-step for the entire model to achieve convergence, this is a naive, computationally wasteful approach. A more sophisticated approach is to write an adaptive algorithm that only increases computational effort when non-convergence is encountered. This study uses a recursive bisection approach to handle non-convergence, roughly as is shown in Algorithm 2. For the collapse study, an ε value of 1e-6 seconds was deemed sufficiently small to handle issues with non-convergence, and if the minimum step size was reached and the analysis step still failed, the model was assumed to have experienced simulated collapse.

Algorithm 2 Convergence Handler for Dynamic Analyses

```
procedure AnalyzeStep(dt,ε)
    ok = return code of one analysis step with time step dt
    if ok ≠ 0 and dt ≥ 2ε then
        ok =AnalyzeStep(dt/2,ε)
        if ok = 0 then
            ok =AnalyzeStep(dt/2,ε)
        end if
    end if
    return ok
end procedure
```

7.4 DBE and MCE Intensity Results

As a baseline, each model was subjected to the P-695 Far Field set anchored to the Design Basis Earthquake (DBE) and Maximum Considered Earthquake (MCE) intensities, where the DBE intensity is 2/3 of the MCE intensity [33]. The results highlight the effects of the design parameters on system response, and can be used to compare directly against other BRBF systems.

7.4.1 Collapse Cases

The number of ground motions that resulted in collapse at the DBE and MCE level ground motions are reported in Table 7.4. In general, the 22 strand archetypes collapsed less than the 14 strand archetypes, and the brace configuration had no effect. It would appear that in general, the target reliability of 10% collapse probability at MCE intensity is met, although the archetypes 1S-LB-14, 6S-LB-14, and 9S-LB-14 are suspect, with 5 out of 44 analyses resulting in collapse. This of course is not how to determine if the target reliability is met according to the P-695 methodology, but it is a good early indicator of whether the selected R factor is appropriate.

Table 7.4: Collapse counts at DBE and MCE intensities

	Count		Percentage	
Archetype ID	DBE	MCE	DBE	MCE
1S-LB-14	0	5	0.0%	11.4%
1S-LB-22	0	3	0.0%	6.8%
3S-LB-14	0	2	0.0%	4.5%
3S-LB-22	0	1	0.0%	2.3%
3S-ZZ-14	0	2	0.0%	4.5%
3S-ZZ-22	0	1	0.0%	2.3%
6S-LB-14	2	5	4.5%	11.4%
6S-LB-22	1	3	2.3%	6.8%
9S-LB-14	2	5	4.5%	11.4%
9S-LB-22	1	3	2.3%	6.8%

7.4.2 Peak and Residual Roof and Story Drift Demands

The mean and mean plus standard deviation peak and residual roof and story drift demands are summarized in Tables 7.5 & 7.6. Analyses resulting in collapsed (simulated or non-simulated) were truncated from the statistical analysis.

While difficult to compare directly, the NZ-BRBF system was observed to have similar structural responses to those of conventional BRBF systems. For example, Fahnestock et al. 2007 investigated a 4-story BRBF model with moment releases at the beam-column connections. This model was subjected to a suite of ground motions scaled to the MCE level intensity, and exhibited a mean peak story drift of 3.3% and a mean residual story drift of 1.2% [66]. These results are comparable to the MCE level intensity results for index archetype model 3S-LB-14, which exhibited a mean peak story drift of 3.1% and a mean residual story drift of 1.4%. The index archetype model 3S-LB-22, however, did not have similar drift responses, suggesting that the 14-strand models in particular are akin to BRBFs with non-moment-resisting beam-column connections.

While the 14-strand models were observed to be comparable to non-moment-resisting BRBFs, the 22-strand models were observed to be comparable to BRBFs modeled with fixed beam-column connections. For example, the study by Sabelli et al. 2003 investigated a 3-story BRBF model with fixed beam-column connections. The 3-story BRBF model designed for an R-factor of 8 and subjected to a 10% in 50 year hazard level (equivalent to DBE intensity) exhibited a mean peak story drift of 1.4% and a mean residual story drift of 0.5% [10]. These results are comparable to the DBE level intensity results for index archetype model 3S-LB-22, which exhibited a mean peak story drift of 1.8% and a mean residual story drift of 0.4%.

Therefore, it was observed that, in general, the 14-strand models behaved like non-moment-resisting BRBFs, while the 22-strand models behaved more like BRBFs with fixed beam-column connections. This is not surprising, as increasing the number of PT strands increases the stiffness of the beam-column connection. It was also observed that, in general, by increasing the number of PT strands from 14 to 22, both the peak and residual drift responses were reduced, with the residual drift responses being reduced the most significantly. Specifically, the peak drift responses were reduced on average by about 8%, and the residual drift responses were reduced on average by about 30%. This suggests that the PT boundary frame helps to reduce residual drift. Because residual drift is a strong indicator of the repairability of a building post-event [14], this also suggests that the PT boundary frame helps increase seismic resiliency. The reduction in mean peak and residual drift responses for each building height is illustrated in Figures 7.7 & 7.8.

Table 7.5: Roof drift mean (μ) and mean plus standard deviation ($\mu+\sigma$) dynamic analysis results

	DBE				MCE			
	Peak		Residual		Peak		Residual	
Archetype ID	μ	$\mu+\sigma$	μ	$\mu+\sigma$	μ	$\mu+\sigma$	μ	$\mu+\sigma$
1S-LB-14	0.022	0.035	0.013	0.026	0.036	0.052	0.024	0.040
1S-LB-22	0.020	0.031	0.009	0.018	0.033	0.047	0.016	0.028
3S-LB-14	0.015	0.023	0.006	0.012	0.024	0.035	0.011	0.021
3S-LB-22	0.014	0.020	0.003	0.006	0.021	0.031	0.005	0.010
3S-ZZ-14	0.015	0.023	0.006	0.011	0.023	0.034	0.011	0.020
3S-ZZ-22	0.014	0.020	0.003	0.006	0.021	0.031	0.005	0.010
6S-LB-14	0.013	0.020	0.008	0.016	0.020	0.030	0.015	0.026
6S-LB-22	0.013	0.022	0.007	0.016	0.019	0.028	0.011	0.021
9S-LB-14	0.011	0.016	0.006	0.013	0.019	0.029	0.016	0.027
9S-LB-22	0.011	0.017	0.006	0.012	0.017	0.025	0.011	0.021

Table 7.6: Story drift mean (μ) and mean plus standard deviation ($\mu+\sigma$) dynamic analysis results

	DBE				MCE			
	Peak		Residual		Peak		Residual	
Archetype ID	μ	$\mu+\sigma$	μ	$\mu+\sigma$	μ	$\mu+\sigma$	μ	$\mu+\sigma$
1S-LB-14	0.022	0.035	0.013	0.026	0.036	0.052	0.024	0.040
1S-LB-22	0.020	0.031	0.009	0.018	0.033	0.047	0.016	0.028
3S-LB-14	0.020	0.031	0.008	0.015	0.031	0.045	0.014	0.026
3S-LB-22	0.018	0.026	0.004	0.008	0.029	0.041	0.007	0.013
3S-ZZ-14	0.020	0.030	0.007	0.014	0.031	0.044	0.013	0.024
3S-ZZ-22	0.018	0.026	0.004	0.007	0.029	0.041	0.007	0.013
6S-LB-14	0.020	0.030	0.011	0.022	0.031	0.043	0.021	0.035
6S-LB-22	0.020	0.032	0.010	0.022	0.030	0.042	0.016	0.029
9S-LB-14	0.020	0.027	0.011	0.020	0.033	0.047	0.025	0.043
9S-LB-22	0.020	0.026	0.009	0.018	0.029	0.040	0.018	0.031

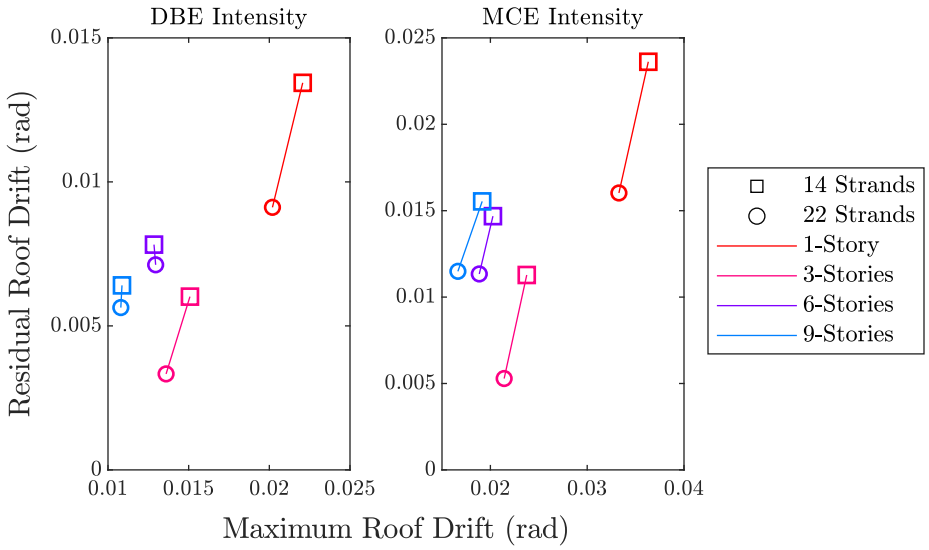

Figure 7.7: Effect of number of PT strands on mean roof drift response

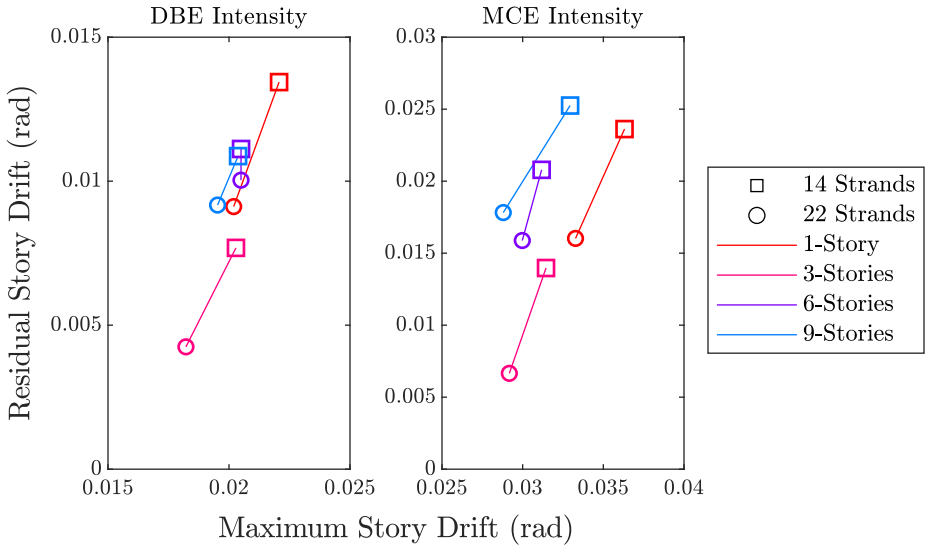

Figure 7.8: Effect of number of PT strands on mean story drift response

7.4.3 Global and Local Response at Collapse

The archetype 6S-LB-14 collapsed subjected to the first horizontal component of ground motion 10, amplitude scaled to MCE intensity. The displaced shape of the finite element model at collapse is shown in Figure 7.9, and the story drift is plotted in Figure 7.10. No significant soft-story effect was observed, although the majority of the drift demand was concentrated in the second and third levels.

At collapse, BRBs in levels 1 through 4 all exceeded the strain limit corresponding to a brace ductility μ_{max} of 30. This can be observed in the BRB hysteresis plots in Figure 7.11, and the fatigue material cumulative damage in Figure 7.12. Note that the braces in level 2 failed first, then level 3, then level 1, and finally level 4.

The PT stress response in respect to analysis time is shown in Figure 7.13. Only the PT from the left frame are shown, as the results from the right frame are nearly identical. All PT strands start at the same stress level, 30% of F_y, and oscillate back and forth until about $t = 17$ seconds. At that point, the column angles in levels 1 through 3 exceed the softening point θ_{pto} and the right PT goes slack. Shortly after, when the BRB in level 2 fails, the PT in levels 1 & 2 yield. The structure does not immediately collapse after this, suggesting that some minor yielding of the PT is not detrimental. However, when the BRBs on levels 1, 3 & 4 fail, the PT in levels 1-3 yield and collapse follows immediately. This suggests that while the PT provides some redundancy for the case when one brace fails, it does not provide sufficient redundancy to safeguard against collapse when multiple braces fail.

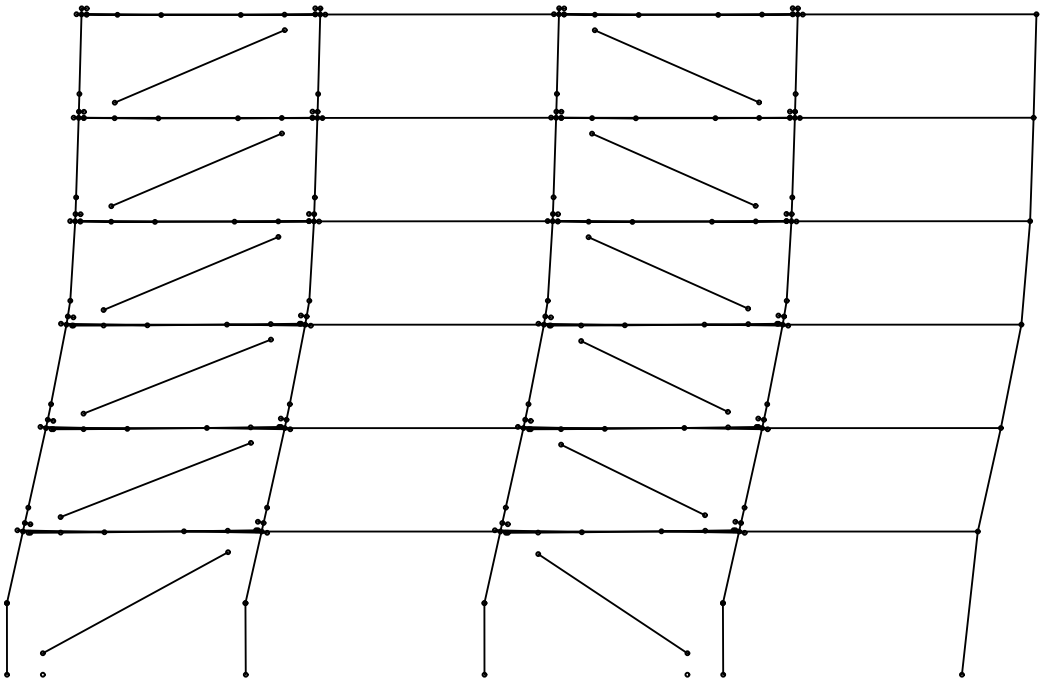

Figure 7.9: Displaced shape at collapse for archetype 6S-LB-14

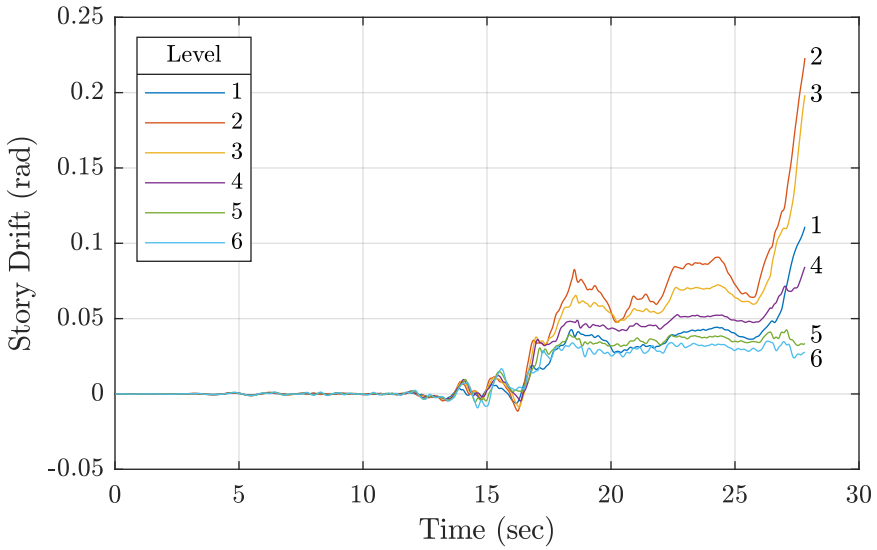

Figure 7.10: Story drift plot for archetype 6S-LB-14 subjected to collapse-level ground motion

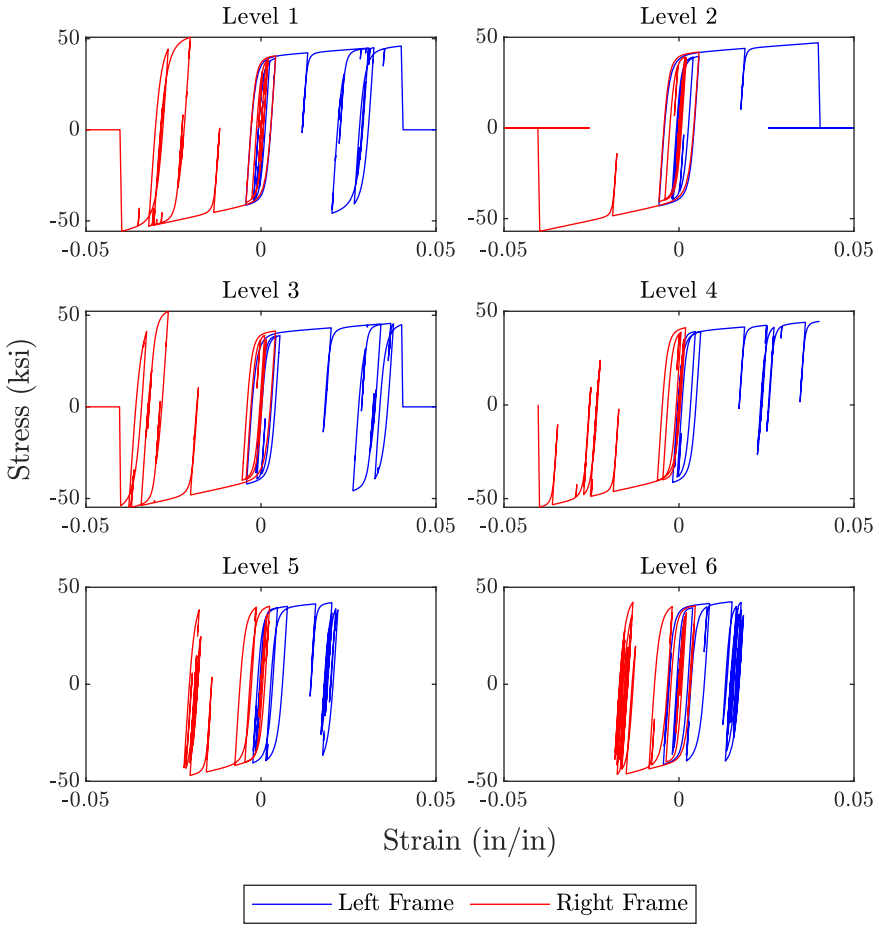

Figure 7.11: BRB hysteresis plot for archetype 6S-LB-14 subjected to collapse-level ground motion

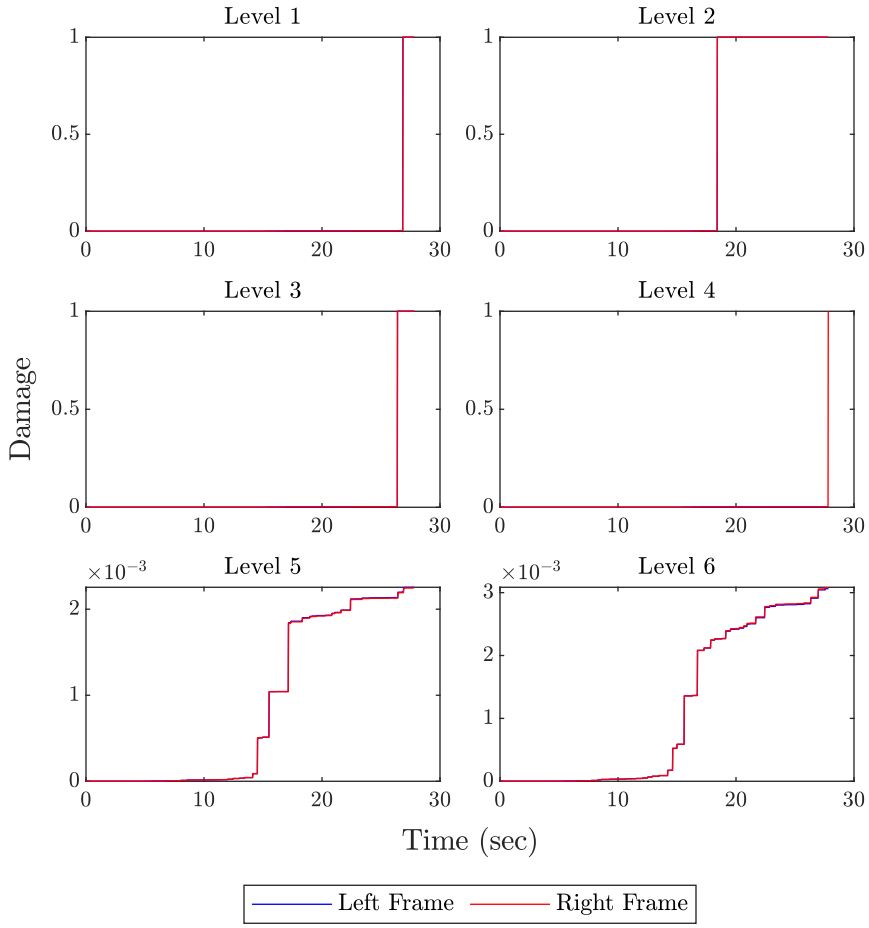

Figure 7.12: BRB damage for archetype 6S-LB-14 subjected to collapse-level ground motion

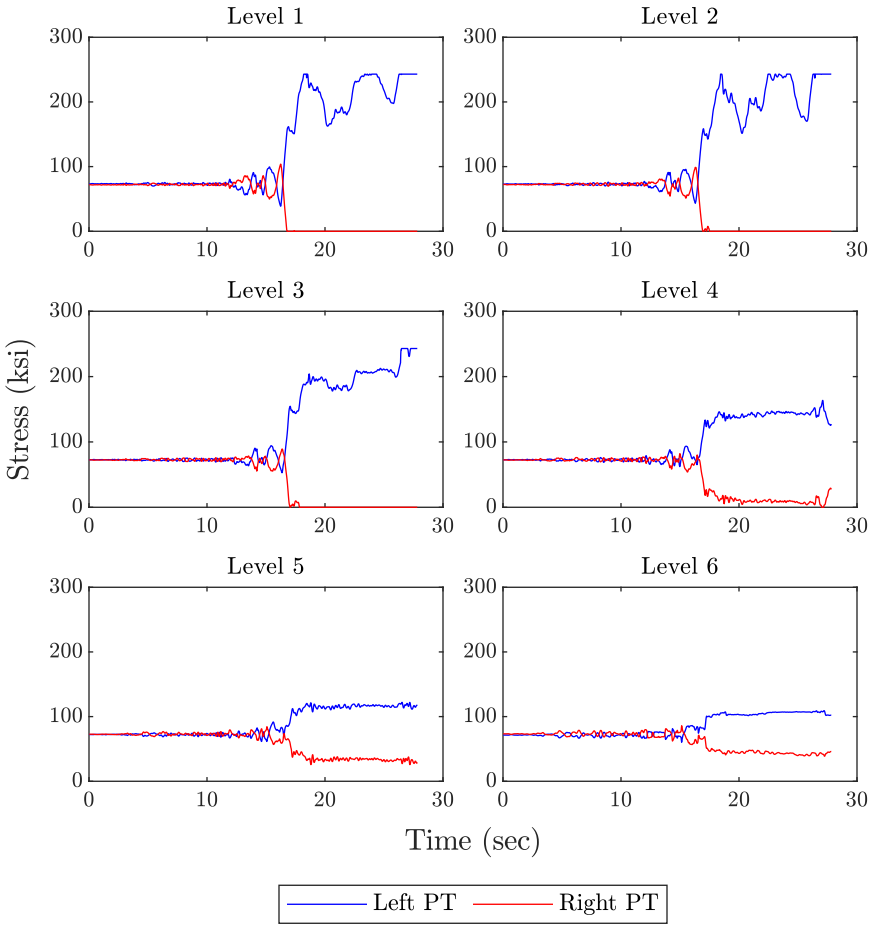

Figure 7.13: PT stress for archetype 6S-LB-14 subjected to collapse-level ground motion

7.5 Summary

This chapter established the ground motion suite used in this study, how damping was applied to the models, how collapse was determined, and the dynamic analysis results for the DBE and MCE level intensities.

Collapse at MCE level intensity was observed to be precluded by brace failure in multiple floors. Failure of a single brace did not lead to immediate collapse, and a characteristic soft-story collapse mechanism did not form, suggesting that the design of the boundary frame provided some level of redundancy. This is further confirmed by the fact that the number of collapse cases was significantly reduced by increasing the number of PT strands from 14 to 22.

For ground motions not resulting in collapse, it was also observed that the 22-strand models exhibited smaller residual drift responses than the 14-strand models. In particular, increasing the number of PT strands from 14 to 22 decreased residual drift on average by 30%. Because residual drift is a common indicator of the repairability of a structure, this further suggests that the NZ-BRBF system may be easier to repair after a seismic event than conventional BRBFs. So, not only does the number of PT strands have a significant impact on the collapse behavior of the system, it also has a significant impact on the repairability of the system post-event.

Chapter 8

Incremental Dynamic Analysis

In order to assess the collapse capacity of the system, Incremental Dynamic Analyses (IDAs) were conducted on the index archetype models, as prescribed by the P-695 methodology. The IDA method consists of incrementally scaling the ground motion intensity until collapse is reached [67]. The resulting damage measure (DM) vs intensity measure (IM) curves show the nonlinear transition from elastic to plastic to collapse.

8.1 Intensity Measure and Collapse Margin Ratio

In accordance with the P-695 methodology, the ground motion intensity measure used was S_T, the median spectral intensity of the scaled, normalized ground motion suite, measured at the fundamental period of the structure. This intensity measure can be expressed as the product of the scale factor SF and the median spectral intensity of the unscaled normalized ground motion suite $\hat{S}_{NT}$, as is shown in Eq. (8.1-1).

$$S_T = SF \times \hat{S}_{NT} \tag{8.1-1}$$

Therefore, the scale factor SF can be used as a proxy intensity measure for the purposes of running the IDAs, because it can be converted to S_T in post-processing. This is useful because it does not require rescaling the ground motion suite for every archetype model.

After the collapse intensity measures are calculated for each ground motion, the collapse margin ratio CMR is calculated as the ratio of the median collapse intensity measure $\hat{S}_{CT}$ and the MCE-level intensity S_{MT}, as is shown in Eq. (8.1-2). This ratio is used to quantify the collapse capacity of the system [3].

$$\text{CMR} = \frac{\hat{S}_{CT}}{S_{MT}} \tag{8.1-2}$$

Alternatively, the collapse margin ratio can be defined by using the median collapse scale factor $\widehat{\text{CSF}}$, as shown in Eq. (8.1-3). This alternative calculation is valid because the suite was anchored and scaled collectively, rather than individually, as illustrated in Figures 7.5 & 7.6.

$$\text{CMR} = \widehat{\text{CSF}} \times \frac{\hat{S}_{NT}}{S_{MT}} \tag{8.1-3}$$

8.2 Damage Measures

A damage measure is typically a structural response quantity that becomes very large at collapse. This is typically a displacement-based quantity rather than a force-based quantity, because forces in a structure are typically capped at the yield capacity of

the system. This study uses peak interstory drift as the main damage measure, as is consistent with other IDA and P-695 studies [4], [30], [68].

8.3 IDA Algorithm

The individual IDAs for each ground motion were traced using a modified version of the hunt-fill algorithm proposed by Vamvatsikos and Cornell [67]. The "hunt-fill" algorithm seeks to achieve a specified precision ε_h on the capacity point (the "hunt" precision), and a specified precision ε_f between points below the capacity point (the "fill" precision). Using this approach, each IDA can be in one of 5 stages: initialization (0), hunt-up (1), bracketing (2), fill-in (3) and finalization (4), which are determined as described below:

0: No points exist.
1: Points are added but collapse has not been reached yet.
2: Collapse has been reached but the gap between the minimum collapse intensity and the estimated capacity (the point immediately below the minimum collapse) is greater than ε_h.
3: Hunt precision is met but gaps exist below the estimated capacity that are greater than ε_f.
4: Both hunt and fill precision requirements are met.

To account for structural resurrections, if a collapse is reached during the fill-in stage (3), the algorithm reverts to the bracketing stage (2).

Then, based on the stage, the next intensity is calculated as follows:

0: Return the user-defined initial intensity.

1: Increment the intensity according to the user-specified hunt-up rule.
2: Bisect the gap between minimum collapse and estimated capacity.
3: Bisect (or trisect if trisection meets the fill precision) the largest gap below the estimated capacity.
4: The IDA is complete.

This approach was implemented in OpenSees using object oriented programming in Tcl [69], where each ground motion IDA curve was represented by a separate TclOO object, containing only the intensity measure and damage measure data. The IDA objects were implemented in such a way that they do not actually run the individual IDA analyses, they simply process the IDA curves and determine the next intensity measures to run. For example, querying the next intensity measure does not change the internal state of the IDA object: it will continue to return the same value until another point is added to the IDA object. This approach to running IDAs is flexible, allowing for running IDAs in series on one processor, running multiple IDAs in parallel on multiple processors, or, simply, post-processing existing IDA data.

8.3.1 IDA Parallelization

The hunt-fill IDA algorithm is an inherently serial algorithm, where analysis runs have to be performed in sequence. For a P-695 study, which require running 44 IDAs on each index archetype model, parallelization is essential. There are two types of parallelization: inter-record parallelization and intra-record parallelization. Inter-record parallelization is quite straight-forward, only requiring that each IDA is performed on a separate processor. However, if one has access to a computer with more cores than IDA curves, inter-record parallelization will not be able to fully utilize all available cores. In this case, intra-record parallelization can be leveraged, where

multiple points on one IDA curve are run in parallel. For this study, intra-record parallelization was only leveraged for the fill-in stage of the IDA algorithm.

Both inter and intra-record parallelization were implemented for the IDAs using OpenSeesMP, the multiple-interpreter parallel version of OpenSees [70]. Each IDA run was assigned a unique integer job tag, which was delegated dynamically to worker processes from the main process with the OpenSeesMP *send* and *recv* commands. Each worker then executed the job within a separate OpenSees interpreter with the Tcl *exec* command.

8.3.2 Partial IDA Refinement

For the purpose of performance evaluation, the P-695 only requires determination of median collapse intensity for the entire Far Field record set, and permits running a simplified IDA procedure. Previous studies have interpreted this to mean that the entire P-695 record suite is scaled up at the same factor until 50% of the ground motions result in collapse [4], [5]. However, there are multiple issues with this approach. First of all, because there are 44 ground motions, there are a range of scale factors, between the 22nd and 23rd highest collapse intensity ground motions, that will result 50% of the ground motions to result in collapse. This could result in an overestimation of the median collapse intensity if the selected intensity was at the higher end of the range. This issue has been recognized in previous studies, which advise, conservatively, to find the lowest intensity that causes 50% collapse [71].

More importantly, the idea that if 50% of ground motions result in collapse represents the median collapse intensity is fundamentally flawed, due to the existence of structural resurrections. Because of the possibility of structural resurrections, where

a structure can collapse at one intensity, and seemingly "resurrect" at a higher intensity, a structure may be non-collapsing at one intensity and collapse at a lower intensity. The actual collapse capacity of a ground motion must then be taken as the lowest collapse point. Therefore, there may be multiple ranges of intensities that will result in 50% collapse, and the actual median collapse intensity may not even lie within one of the ranges, as is illustrated in Figure 8.1.

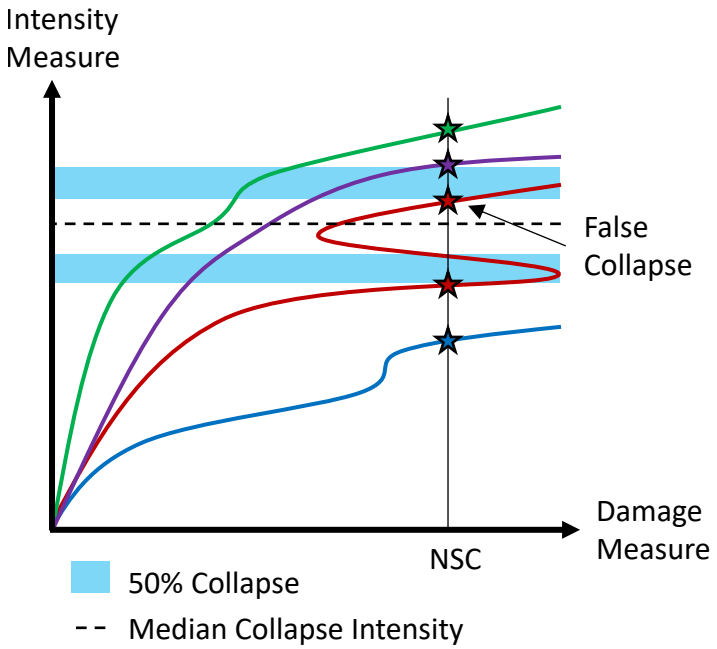

Figure 8.1: Visual proof that 50% collapse is not equal to median collapse intensity

A more robust approach is to selectively refine IDA curves based on their estimated collapse capacity in relation to the estimated median collapse intensity. For example, ground motions that collapse well below the median collapse intensity do not need to be investigated for structural resurrections, as a smaller collapse intensity for those ground motions would not affect the median collapse intensity [72]. Conversely, ground motions that converge well above the median collapse intensity do not need

to be in the hunt-up or bracketing stage of the IDA algorithm, but should be investigated for structural resurrection in case the true collapse intensity lies below the estimated median collapse intensity.

In order to take advantage of these efficiencies, the following approach is proposed for a suite of N ground motions: Order the ground motions in respect to increasing estimated capacity, where the estimated capacity is taken as the intensity measure immediately below the minimum collapse intensity or, if collapse has not been reached, simply the largest analyzed intensity, or, if no analyses are complete, zero. For an even number of ground motions, let A be the estimated collapse capacity of ground motion $N/2$, and let B be the estimated collapse capacity of ground motion $N/2+1$. In this case, the estimated median collapse capacity is equal to $(A+B)/2$. For an odd number of ground motions, let A and B be equal to the estimated capacity of ground motion $(N+1)/2$. In this case, the estimated median collapse capacity is equal to A and B. Then, because the estimated collapse capacity is between intensities A and B, the IDA algorithm can be modified for each ground motion based on the following rules:

1. Both estimated capacity and minimum collapse are below A: No more analyses are required, because bracketing and fill-in would not change the median capacity intensity.

2. Estimated capacity is below A, minimum collapse is above A: In this case, it is possible that the actual capacity of this ground motion could be above A, so bracketing is required, but fill-in stage is not needed, because a structural resurrection would not affect the median collapse capacity for this case.

3. Estimated capacity is equal to A or B: This ground motion is one of the key ground motions that determines the median collapse capacity, so full refinement is necessary.

4. Estimated capacity is above B: Hunting and bracketing are not required, but curve should be filled in below B to capture potential structural resurrections, which could change the order of the ground motion estimated capacities in a way that affects the median collapse capacity.

With this approach, all ground motions begin at an estimated capacity of zero, so A and B are also equal to zero, so all ground motions require full refinement. As collapse is reached for some ground motions, A and B shift towards the median collapse capacity. Finally, given adequate hunt-fill precision values, A and B converge around the median collapse intensity.

This approach was used to significantly reduce the number of analysis runs required to determine the median collapse capacity while also considering structural resurrections. To demonstrate the efficiency and accuracy of the partial IDA method presented in this study, the collapse study was run both by fully developing the IDA curves for each ground motion and also by employing the proposed strategy. The hunt-up method used for both methods was geometric, starting at a scale factor of 1.0 and doubling until collapse was reached, and hunt-fill precision values of $\varepsilon_h = 0.05$ and $\varepsilon_f = 0.5$ were used for refining the IDA curves. The runs required for a full IDA vs a partial IDA for each index archetype model are shown in Table 8.1. Both methods came to the same value for median collapse capacity, but the partial IDA strategy required significantly fewer analysis runs.

To show the effect of ignoring structural resurrections, the same analyses were conducted with $\varepsilon_f = \infty$, which effectively bypassed the fill-in stage of the hunt-fill algorithm. The results without fill-in are shown in Table 8.2. As with the results for $\varepsilon_f = 0.5$, there was no difference between the full and partial IDA methods for the median collapse, except for the fact that the number of runs varied. However, the difference in the number of runs was negligible. Therefore, in the case where structural

resurrections are ignored, this study suggests that there is little, if any, advantage in using the partial IDA method. The partial IDA method, therefore, is only advantageous if there is a significant advantage to considering structural resurrections. For this system subjected to the the Far Field set, the median collapse scale factor $\widehat{\text{CSF}}$ was overestimated by at most 3.3% by ignoring structural resurrections.

For systems with a higher occurrence of structural resurrections, such as rocking systems, ignoring structural resurrections may have a larger impact on the results [73]. In these situations, it would be more important to consider structural resurrections, and thus the partial IDA approach could be used to great effect to reduce the number of required runs.

Table 8.1: Full vs. partial IDA, $\varepsilon_h = 0.05$ and $\varepsilon_f = 0.5$

	Full IDA		Partial IDA		Difference	
Archetype ID	# of runs	$\widehat{\text{CSF}}$	# of runs	$\widehat{\text{CSF}}$	# of runs	$\widehat{\text{CSF}}$
1S-LB-14	531	3.031	339	3.031	-36%	0%
1S-LB-22	539	3.281	345	3.281	-36%	0%
3S-LB-14	702	4.766	451	4.766	-36%	0%
3S-LB-22	742	5.203	499	5.203	-33%	0%
3S-ZZ-14	719	4.750	475	4.750	-34%	0%
3S-ZZ-22	758	5.266	494	5.266	-35%	0%
6S-LB-14	661	4.156	414	4.156	-37%	0%
6S-LB-22	726	4.828	437	4.828	-40%	0%
9S-LB-14	643	3.781	331	3.781	-49%	0%
9S-LB-22	699	4.609	419	4.609	-40%	0%

Table 8.2: Full vs. partial IDA, $\varepsilon_h = 0.05$ and $\varepsilon_f = \infty$

	Full IDA		Partial IDA		Difference	
Archetype ID	# of runs	$\widehat{\text{CSF}}$	# of runs	$\widehat{\text{CSF}}$	# of runs	$\widehat{\text{CSF}}$
1S-LB-14	249	3.031	253	3.031	2%	0%
1S-LB-22	261	3.281	258	3.281	-1%	0%
3S-LB-14	315	4.781	310	4.781	-2%	0%
3S-LB-22	319	5.219	316	5.219	-1%	0%
3S-ZZ-14	308	4.828	305	4.828	-1%	0%
3S-ZZ-22	321	5.344	323	5.344	1%	0%
6S-LB-14	277	4.156	275	4.156	-1%	0%
6S-LB-22	281	4.922	281	4.922	0%	0%
9S-LB-14	240	3.906	205	3.906	-15%	0%
9S-LB-22	276	4.609	275	4.609	0%	0%

8.4 IDA Results

IDAs were conducted on each of the index archetype models with the Far Field record suite, using partial IDA refinement and not ignoring structural resurrections. An example IDA plot is shown in Figure 8.2 for archetype 6S-LB-14, with collapse points omitted. Note that since the partial IDA refinement method was used, IDA curves well below the median collapse point were not refined.

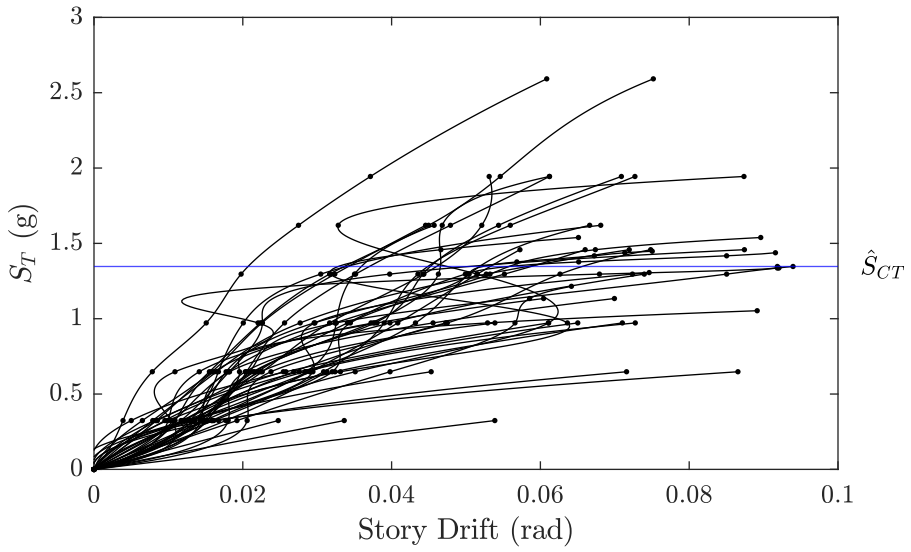

Figure 8.2: IDA plot for index archetype 6S-LB-14, using partial IDA refinement

The median collapse scale factor, spectral intensity, and collapse margin ratio for each index archetype are tabulated in Table 8.3. These results are used for the performance evaluation of the system in the following chapter.

Table 8.3: IDA collapse study results

Archetype ID	S_{MT}	$\hat{S}_{NT}$	$\widehat{\text{CSF}}$	$\hat{S}_{CT}$	CMR
1S-LB-14	1.500	0.881	3.031	2.670	1.780
1S-LB-22	1.500	0.881	3.281	2.890	1.926
3S-LB-14	1.373	0.593	4.766	2.827	2.059
3S-LB-22	1.373	0.593	5.203	3.087	2.248
3S-ZZ-14	1.373	0.593	4.750	2.818	2.052
3S-ZZ-22	1.373	0.593	5.266	3.124	2.275
6S-LB-14	0.779	0.324	4.156	1.347	1.728
6S-LB-22	0.779	0.324	4.828	1.564	2.007
9S-LB-14	0.584	0.235	3.781	0.887	1.520
9S-LB-22	0.584	0.235	4.609	1.081	1.853

8.4.1 Effect of Design Parameters on Collapse Capacity

The index archetype models with a ZZ brace configuration had slightly higher collapse capacity than their LB configuration counterparts. For this reason, only the LB configuration was investigated for the 6 and 9 story building heights.

The index archetype models with 22 strands of PT out-performed the models with 14 strands. In specific, the collapse capacity of the 22 strand models was 8% higher for 1-story archetypes, 10% higher for 3-story archetypes, 18% higher for 6-story archetypes, and 22% higher for 9-story archetypes. This suggests that the PT boundary frame helps increase seismic stability, especially for taller structures.

Chapter 9

Performance Evaluation

This chapter presents the results of the performance evaluation of the NZ-BRBF system for the purpose of determining whether the target reliability is met with the proposed seismic performance factors (SPFs). The performance evaluation is carried out by comparing the IDA results to acceptable values based on the target reliability, system properties, and qualitative uncertainty factors. The results suggest that the NZ-BRBF system can be designed with the following SPFs: a response modification coefficient, or R factor, of 8.0, a system overstrength Ω_O of 2.0, and a deflection amplification factor C_d of 8.0.

9.1 Quality Ratings

In accordance with the P-695 methodology, collapse performance was evaluated with assumed fragility curves, adjusted for uncertainty in the study. The fragility curves are assumed to follow lognormal cumulative probability distribution curves, with the median taken as the median collapse point, and the standard deviation a combination

of four total uncertainty factors, or lognormal standard deviations: the record-to-record uncertainty, β_{RTR}, the design requirements uncertainty, β_{DR}, the test data uncertainty, β_{TD}, and the modeling uncertainty, β_{MDL}.

For the design requirements, test data, and modeling uncertainties, quality ratings are assumed from two related subjective criteria, using the matrix in Table 9.1. Both subjective criteria are assigned a value from "Low" to "High". The combination of "Low" and "Low" is not allowed for any quality rating. The resulting subjective quality ratings correspond to uncertainty values: "Superior" corresponds to $\beta = 0.10$, "Good" corresponds to $\beta = 0.20$, "Fair" corresponds to $\beta = 0.35$, and "Poor" corresponds to $\beta = 0.50$.

Table 9.1: Quality rating matrix

	High	**Medium**	**Low**
High	Superior	Good	Fair
Medium	Good	Fair	Poor
Low	Fair	Poor	-

9.1.1 Record-to-Record Uncertainty

Record-to-record uncertainty, β_{RTR}, is calculated based on the period-based ductility μ_T of the structure, shown in Eq. (9.1-1) (Eq. 7-2 in P-695).

$$\beta_{RTR} = 0.1 + 0.1\mu_T \leq 0.40 \tag{9.1-1}$$

Because the period-based ductility values are greater than 3 for all index archetypes, β_{RTR} is fixed at 0.4.

9.1.2 Quality Rating of Design Requirements

The quality rating for design requirements was determined from a subjective evaluation of the completeness, robustness, and confidence in basis of design requirements. Completeness and robustness was assumed to be "Medium", because most of the important design and quality assurance issues are addressed. However, as it is a new system, some failure modes may not be addressed. Confidence in the basis of design requirements was assumed to be "High", because the system is essentially a type of BRBF, and the AISC 341 and ASCE 7 requirements for BRBFs were followed. As a result, the overall quality rating is "Good", corresponding to a β_{DR} of 0.2.

9.1.3 Quality Rating of Test Data

The quality rating for design requirements was determined from a subjective evaluation of the completeness, robustness, and confidence in test results. Completeness and robustness was assumed to be "Medium", because no experimental testing of the NZ-BRB frame was conducted. However, material models for the BRBs were used with recommended parameters as determined from experimental results [29], and the NewZ-BREAKSS boundary frame has been experimentally verified [23], [27]. Confidence was also assumed to be "Medium", resulting in an overall quality rating of "Fair", corresponding to a β_{TD} of 0.35.

9.1.4 Quality Rating of Index Archetype Models

The quality rating for design requirements was determined from a subjective evaluation of the representation of collapse characteristics, and the accuracy and robustness of the models. Representation was assumed to be "Medium", because the design

space covers a reasonable range of building heights and configurations, and most critical failure modes are addressed. Accuracy was assumed to be "Medium", because most collapse conditions are explicitly modeled, with the exception of the brace ductility limit and 10% story drift limit. Therefore, a quality rating of "Fair" was assumed, corresponding to a β_{MDL} of 0.35.

9.1.5 Total System Collapse Uncertainty

Assuming the individual uncertainty components are statistically independent, the total uncertainty is taken as the norm of four total uncertainty factors, shown in Eq. (9.1-2) (Eq. 7-5 in P-695).

$$\beta_{TOT} = \sqrt{\beta_{RTR}^2 + \beta_{DR}^2 + \beta_{TD}^2 + \beta_{MDL}^2} \tag{9.1-2}$$

Using this equation and the uncertainty component values previously established, the total system uncertainty for each index archetype is equal to 0.67.

9.2 Spectral Shape Factor (SSF) and Adjusted Collapse Margin Ratio (ACMR)

Although some amplitude scaling bias was addressed by normalizing the ground motion suite to PGV_{PEER} and anchoring the suite with the median spectra, there still exists some bias based on the frequency content of the ground motion suite. That is, the frequency content of actual MCE-level ground motions are distinctly different than spectra of less rare (or more frequent earthquake events). The P-695 methodology addresses this by adjusting the collapse capacity of the system with a spectral shape factor (SSF), which is a function of fundamental period T and period-based

ductility μ_T, determined according to Table 7-1b in the P-695 [3]. This adjusted collapse margin ratio (ACMR), calculated according to Eq. (9.2-1), better represents the collapse capacity of the system [3].

$$\text{ACMR} = \text{SSF} \times \text{CMR} \tag{9.2-1}$$

In order to determine if an index archetype passes the evaluation, it must have an ACMR value greater than the acceptable ACMR for the target reliability. For a collapse probability of 10% at the MCE level intensity, and a total system uncertainty of 0.67, the acceptable ACMR ($\text{ACMR}_{10\%}$) is 2.35, according to Table 7.3 in the P-695 [3]. The computed ACMR values and whether the index archetypes pass the performance evaluation are tabulated in Table 9.2. All index archetypes pass the performance evaluation for an R of 8.

Table 9.2: Performance evaluation

Archetype ID	T (sec)	μ_T	SSF	CMR	ACMR	$\text{ACMR}_{10\%}$	Pass?
1S-LB-14	0.288	18.547	1.330	1.780	2.367	2.355	OK
1S-LB-22	0.288	18.032	1.330	1.926	2.562	2.355	OK
3S-LB-14	0.655	18.427	1.371	2.059	2.823	2.355	OK
3S-LB-22	0.655	16.479	1.371	2.248	3.083	2.355	OK
3S-ZZ-14	0.655	18.833	1.371	2.052	2.814	2.355	OK
3S-ZZ-22	0.655	17.656	1.371	2.275	3.120	2.355	OK
6S-LB-14	1.155	20.732	1.506	1.728	2.603	2.355	OK
6S-LB-22	1.155	21.045	1.506	2.007	3.024	2.355	OK
9S-LB-14	1.542	13.546	1.610	1.520	2.447	2.355	OK
9S-LB-22	1.542	17.647	1.610	1.853	2.983	2.355	OK

9.3 Proposed Seismic Performance Factors

The NZ-BRBF system was designed with an assumed seismic response modification factor, or R factor, of 8, and passed the performance evaluation for the target reliability. Therefore, an R factor of 8 is proposed for the NZ-BRBF system. The deflection amplification factor C_d was taken to be equal to R for design, and in absence of experimental data supporting a smaller value, a C_d value of 8 is proposed. The system overstrength Ω_O was determined from archetype overstrength values from nonlinear static analyses. Rounding the largest archetype overstrength to the next half-increment, an Ω_O value of 2.0 is proposed.

Chapter 10

Summary and Conclusions

The low post-yield stiffness of Buckling Restrained Braced Frame (BRBF) systems leaves them susceptible to large residual drifts. Because residual drift is a strong indicator of the economic viability of repair [14], this means that demolition is likely to be more economical than repair for BRBFs after a seismic event. In order to increase the resiliency of BRBFs, researchers have proposed various methods to reduce the residual drift response of BRBFs. This study proposed combining a BRBF with the recently proposed NewZ-BREAKSS (NZ) boundary frame [2] as a way to simultaneously concentrate all damage to the Buckling Restrained Braces (BRBs) and possibly decrease residual drifts. This is accomplished with a top-flange rocking beam-column connection and a pinned column detail, where the pin is located at the first floor column midpoint for multi-story structures.

The proposed NZ-BRBF system was evaluated using the FEMA P-695 methodology [3] to establish appropriate seismic performance factors (SPFs) for seismic design according to ASCE 7 [33]. The results indicated that the NZ-BRBF system can be

designed with a response modification coefficient R of 8.0, a deflection amplification factor C_d of 8.0, and a system overstrength Ω_O of 2.0.

Before determining system SPFs, first the mechanical behavior of the proposed SFRS was investigated by developing and comparing kinematic equations and numerical models of the system. Then, using the developed kinematic equations and numerical models, a range of index archetype models were designed with an assumed R-factor of 8.0 and using typical design requirements for BRBFs. These index archetype models were then used to evaluate the seismic performance of the system by conducting nonlinear static and dynamic analyses. In particular, collapse capacities of each index archetype model were determined by Incremental Dynamic Analysis (IDA), an analysis method in which nonlinear dynamic analyses are conducted on a model in increasing intensity until collapse is reached.

Because IDAs are computationally expensive and because the P-695 methodology only requires the median collapse capacity, a new partial IDA approach was developed that greatly reduced the number of analyses required, while also not ignoring structural resurrections. This new IDA approach was documented and validated by comparing the results to a full IDA. Both the full and partial IDA analyses converged on the same median collapse capacity, with the partial IDA method requiring about 40% less nonlinear dynamic analyses.

Finally, using the results from the nonlinear static and dynamic analyses, the seismic performance of the system was quantified in an adjusted collapse margin ratio (ACMR), which was compared against an acceptable ACMR based on total system uncertainty. The results suggested that the initial assumed R-factor was acceptable; the NZ-BRBF system can be designed with an R-factor of 8.0.

In addition to determining the system SPFs, the effects of the brace configuration and number of post-tensioning (PT) strands on the system were investigated. Seismic design, nonlinear static analysis, and nonlinear dynamic analysis established that brace configuration has little effect on the behavior of the NZ-BRBF system. However, the index archetype models with a ZZ brace configuration did have slightly larger collapse capacity than those with an LB configuration, so the ZZ configuration was only explored for the 3-story building height. Unlike the brace configuration parameter, the number of PT strands per floor had a significant impact on the response of the system. While both the 14 and 22 strand archetypes passed the performance evaluation, the index archetypes with 22 strands of PT outperformed the archetypes with 14 strands in collapse capacity and residual drift response: increasing the number of PT strands from 14 to 22 increased the collapse capacity and decreased the residual drift response.

In summary, the NZ-BRBF system was observed to exhibit similar structural response to conventional BRBFs and can be designed with the same R-factor. The main difference is in the boundary frame detailing, which provides secondary stiffness while still concentrating all damage to the BRBs. This secondary stiffness is beneficial for structural redundancy and reducing residual drift, which should facilitate rapid recovery after a design event.

10.1 Recommendations for Future Research

This study is a preliminary investigation of the NZ-BRBF system. As such, it is limited in its scope, and much remains to investigate. Some possible topics of future work are as follows:

- This study was a preliminary P-695 evaluation of the NZ-BRBF system, with a relatively small number of index archetype models, no experimental program, and lack of external peer review. Further study is necessary to fully validate the system SPFs and design requirements.
- The number of PT strands was observed to have a significant impact on the performance of the NZ-BRBF frame. However, only two levels of PT were investigated, 14 and 22 strands, so results should not be extrapolated. Further research is required to fully understand the effect of the number of PT strands on the response of the NZ-BRBF system, and to develop a rational design basis.
- Although experimental tests have been done on BRBs, BRBFs, and the NewZ-BREAKSS boundary frame, no assembly tests have been conducted on the NZ-BRBF system. An experimental program, including component and assembly tests, would help to validate the numerical modeling and identify any unforeseen modes of failure.
- Although the NZ-BRBF system is not self-centering, the boundary frame is detailed such that the damage is concentrated in the BRBs, and thus should be relatively easy to repair. This hypothesis is informed from shake table tests of the SC-SPSW system, which utilized the same NewZ-BREAKSS boundary frame. However, shake table tests with a NZ-BRBF assembly, including post-event repair, are needed to confirm this.
- The NZ-BRBF system includes a unique column pin detail, where the pin is located half-way up the column. This was included because it was observed to

increase system redundancy while preventing the formation of a plastic hinge at the column base. A comparative study of the NZ-BRBF frame with a conventional pinned base would be helpful to demonstrate the advantage of the unique detail, and possibly show its potential for use in other SFRSs.

- The detailing of the NZ-BRBF provides elastic secondary stiffness, which may be helpful in resisting cascading events such as mainshock-aftershock and mainshock-service wind scenarios. A study investigating the response of the NZ-BRBF to these events in comparison to conventional non-moment-resisting and moment-resisting BRBFs may shed some light in this area.
- The NZ-BRBF frame uses conventional BRBs as the bracing elements, and as such is not self-centering. Therefore, repair would likely require replacement of the BRBs to center the building. Alternatively, if special self-centering braces were used instead of conventional BRBs, the structural system could be fully seismically resilient, requiring no repair after a design event.

Bibliography

[1] D. M. Dowden and M. Bruneau, "Kinematics of Self-Centering Steel Plate Shear Walls with NewZ-BREAKSS Post-Tensioned Rocking Connection," *Engineering Journal-American Institute Of Steel Construction*, vol. 53, no. 3, pp. 117–135, 2016, ISSN: 0013-8029.

[2] D. M. Dowden and M. Bruneau, "NewZ-BREAKSS: Post-tensioned rocking connection detail free of beam growth," *Engineering Journal(Chicago)*, vol. 48, no. 2, pp. 153–158, 2011, ISSN: 0013-8029.

[3] FEMA, *Quantification of Building Seismic Performance Factors, FEMA P-695*. Washington, D. C.: Federal Emergency Management Agency, 2009.

[4] NEHRP, "Evaluation of the FEMA P-695 Methodology for Quantification of Building Seismic Performance Factors," Tech. Rep. NIST GCR 10-917-8, 2010.

[5] S. Zaruma, "Seismic stability of buckling-restrained braced frames," M.S. thesis, University of Illinois at Urbana-Champaign, 2017.

[6] A. Kheyroddin and N. Mashhadiali, "Response modification factor of concentrically braced frames with hexagonal pattern of braces," *Journal of Constructional Steel Research*, vol. 148, pp. 658–668, 2018, ISSN: 0143-974X. DOI: 10.1016/j.jcsr.2018.06.024.

[7] A. Wada, M. Iwata, and A. Watanabe, "Properties of brace encased in concrete-filled steel tube," *IABSE reports*, vol. 60, p. 493, 1990. DOI: 10.5169/seals-46530.

[8] R. Tremblay, P. Bolduc, R. Neville, and R. DeVall, "Seismic testing and performance of buckling-restrained bracing systems," *Canadian Journal of Civil Engineering*, vol. 33, no. 2, pp. 183–198, Feb 2006 2017-11-08, ISSN: 03151468.

[9] C. Black, N. Makris, and I. Aiken, "Component Testing, Stability Analysis and Characterization of Buckling-Restrained Unbonded BracesTM," Pacific Earthquake Engineering Research Center, Berkeley, CA, PEER Report 2002/08, 2002.

[10] R. Sabelli, S. Mahin, and C. Chang, "Seismic demands on steel braced frame buildings with buckling-restrained braces," *Engineering Structures*, vol. 25, no. 5, pp. 655–666, 2003, ISSN: 0141-0296.

[11] ASCE, *Minimum Design Loads for Buildings and Other Structures, ASCE/SEI 7-05*. Reston, VA: American Society of Civil Engineers, 2005.

[12] AISC, *Seismic Provisions for Structural Steel Buildings, AISC 341-05*. Chicago, IL: American Institute of Steel Construction, 2005.

[13] J. Erochko, C. Christopoulos, R. Tremblay, and H. Choi, "Residual Drift Response of SMRFs and BRB Frames in Steel Buildings Designed according to ASCE 7-05," *Journal of Structural Engineering*, vol. 137, no. 5, pp. 589–599, 2011. DOI: 10.1061/(ASCE)ST.1943-541X.0000296.

[14] Y. Iwata, H. Sugimoto, and H. Kuwamura, "Reparability Limit of Steel Structural Buildings Based on the Actual Data of the Hyogoken-Nanbu Earthquake," *Journal of Structural and Construction Engineering*, no. 588, pp. 165–172, 2005, ISSN: 1340-4202.

[15] J. McCormick, H. Aburano, M. Ikenaga, and M. Nakashima, "Permissible Residual Deformation Levels for Building Structures Considering Both Safety and

Human Elements," in *Proceedings of the 14th World Conference on Earthquake Engineering*, J. McCormick, Ed., Beijing, China, 2008.

[16] C. Christopoulos, R. Tremblay, H. Kim, and M. Lacerte, "Self-Centering Energy Dissipative Bracing System for the Seismic Resistance of Structures: Development and Validation," *Journal of Structural Engineering*, vol. 134, no. 1, pp. 96–107, 2008, ISSN: 0733-9445. DOI: 10.1061/(ASCE)0733-9445(2008)134:1(96).

[17] M. R. Eatherton, L. A. Fahnestock, and D. J. Miller, "Computational study of self-centering buckling-restrained braced frame seismic performance," *Earthquake Engineering and Structural Dynamics*, vol. 43, no. 13, pp. 1897–1914, 2014, ISSN: 0098-8847. DOI: 10.1002/eqe.2428.

[18] K. Atasever, S. Inanaga, T. Takeuchi, Y. Terazawa, and O. C. Celik, "Experimental and numerical studies on buckling restrained braces with posttensioned carbon fiber composite cables," *Earthquake Engineering and Structural Dynamics*, 2020, ISSN: 0098-8847. DOI: 10.1002/eqe.3321.

[19] Q. Xie, Z. Zhou, and S.-P. Meng, "Experimental investigation of the hysteretic performance of self-centering buckling-restrained braces with friction fuses," *Engineering Structures*, vol. 203, p. 109 865, Jan. 2020, ISSN: 0141-0296. DOI: 10.1016/j.engstruct.2019.109865.

[20] S. Kiggins and C.-M. Uang, "Reducing residual drift of buckling-restrained braced frames as a dual system," *Engineering Structures*, vol. 28, no. 11, pp. 1525–1532, 2006, ISSN: 0141-0296.

[21] L. Tian and C. Qiu, "Controlling Residual Drift in BRBFs by Combining SC-CBFs in Parallel," *Journal of performance of constructed facilities*, vol. 32, no. 4, p. 4 018 047, 2018, ISSN: 0887-3828. DOI: 10.1061/(ASCE)CF.1943-5509.0001191.

[22] C. Christopoulos, A. Filiatrault, C.-M. Uang, and B. Folz, "Posttensioned Energy Dissipating Connections for Moment-Resisting Steel Frames," *Journal of Structural Engineering*, vol. 128, no. 9, pp. 1111–1120, 2002, ISSN: 0733-9445. DOI: 10.1061/(ASCE)0733-9445(2002)128:9(1111).

[23] D. M. Dowden, P. M. Clayton, C.-H. Li, *et al.*, "Full-Scale Pseudodynamic Testing of Self-Centering Steel Plate Shear Walls," *Journal of Structural Engineering*, vol. 142, no. 1, 2016, ISSN: 0733-9445. DOI: 10.1061/(ASCE)ST.1943-541X.0001367.

[24] K. Robinson, "Specifying Buckling-Restrained Brace Systems," *Modern Steel Construction*, vol. 49, no. 11, pp. 57–57, 2009, ISSN: 0026-8445.

[25] NIST, "Seismic design of steel buckling-restrained braced frames: A guide for practicing engineers," Gaithersburg, MD, NEHRP Seismic Design Technical Brief No. 11, Produced by the Applied Technology Council and the Consortium of Universities for Research in Earthquake Engineering for the National Institute of Standards and Technology, GCR 15-917-34, 2015.

[26] L. Fahnestock, R. Sause, J. Ricles, and L.-W. Lu, "Ductility demands on buckling-restrained braced frames under earthquake loading," *Earthquake Engineering and Engineering Vibration*, vol. 2, no. 2, pp. 255–268, 2003, ISSN: 1671-3664. DOI: 10.1007/s11803-003-0009-5.

[27] D. M. Dowden and M. Bruneau, "Analytical and Experimental Investigation of Self-Centering Steel Plate Shear Walls," MCEER, Buffalo, NY, Tech. Rep., 2014.

[28] A. Kamali Yazdi and A. Shooshtari, "The stiffness matrix of cracked finite elements: Introducing shortcomings in applying stiffness approach and proposing a solution," *Engineering Fracture Mechanics*, vol. 191, pp. 412–425, 2018, ISSN: 0013-7944. DOI: 10.1016/j.engfracmech.2017.12.020.

[29] Á. Zsarnóczay, "Experimental and Numerical Investigation of Buckling Restrained Braced Frames for Eurocode Conform Design Procedure Development," Ph.D. dissertation, Budapest University of Technology and Economics, 2013.

[30] O. Atlayan, "Hybrid Steel Frames," Ph.D. dissertation, Virginia Technological University, 2013.

[31] FEMA, *State of the Art Report on Systems Performance of Steel Moment Frames Subject to Earthquake Ground Shaking, FEMA 355C*. Washington, D.C.: Federal Emergency Management Agency, 2000.

[32] H. Pham, "Performance-based assessments of buckling-restrained braced steel frames retrofitted by self-centering shape memory alloy braces," M.S. thesis, Georgia Institute of Technology, Aug. 2013.

[33] ASCE, *Minimum Design Loads and Associated Criteria for Buildings and Other Structures, ASCE/SEI 7-16*. Reston, Virginia: American Society of Civil Engineers, 2016.

[34] AISC, *Seismic Provisions for Structural Steel Buildings, ANSI/AISC 341-16*. Chicago, IL: American Institute of Steel Construction, 2016.

[35] AISC, *Specifications for Structural Steel Buildings, ANSI/AISC 360-16*. Chicago, IL: American Institute of Steel Construction, 2016.

[36] S. Merritt, C.-M. Uang, and G. Benzoni, "Subassemblage Testing of Star Seismic Buckling Restrained Braces," University of California, San Diego, La Jolla, California, Structural Systems Research Project TR-2003/04, 2003.

[37] L. A. Fahnestock, R. Sause, and J. M. Ricles, "Analytical and Large-scale Experimental Studies of Earthquake-resistant Buckling Restrained Braced Frame Systems," Lehigh University, Bethlehem, PA, ATLSS Reports 06-01, 2006.

[38] ASTM, "Standard specification for steel strand, uncoated seven-wire for prestressed concrete," *ASTM Standard A416*, 2006.

[39] F. McKenna, M. H. Scott, and G. L. Fenves, "Nonlinear Finite-Element Analysis Software Architecture Using Object Composition," *Journal of Computing in Civil Engineering*, vol. 24, no. 1, pp. 95–107, 2010, ISSN: 0887-3801. DOI: 10.1061/(ASCE)CP.1943-5487.0000002.

[40] R. K. Devalapura and M. K. Tadros, "Stress-Strain Modeling of 270 ksi Low-Relaxation Prestressing Strands," *PCI Journal*, vol. 37, no. 2, pp. 100–106, Mar. 1992.

[41] K. Kolozvari, K. Orakcal, and J. Wallace, "Shear-flexure interaction modeling for reinforced concrete structural walls and columns under reversed cyclic loading," University of California, Berkeley, Berkeley, CA, PEER Report 2015/12, 2015.

[42] M. Menegotto and P. E. Pinto, "Method of analysis of cyclically loaded RC plane frames including changes in geometry and non-elastic behavior of elements under normal force and bending," in *Proceedings of the IABSE Symposium on Resistance and Ultimate Deformability of Structures Acted on by Well Defined Repeated Loads*, vol. 11, 1973, pp. 15–22.

[43] F. C. Filippou, E. P. Popov, and V. V. Bertero, "Effects of bond deterioration on hysteretic behavior of reinforced concrete joints," Earthquake Engineering Research Institute, Tech. Rep. UCB/EERC-83/19, 1983.

[44] P. Uriz and S. A. Mahin, "Toward Earthquake-Resistant Design of Concentrically Braced Steel-Frame Structures," Pacific Earthquake Engineering Research Center, Berkeley, CA, PEER Report 2008/08, 2008.

[45] PEER, *NGA-West2 Ground Motion Database*, https://ngawest2.berkeley.edu/, 2013.

[46] A. Shakal, "CSMIP strong-motion records from the Petrolia, California earthquakes of April 25-26, 1992," California Department of Conservation, Sacramento, CA, Tech. Rep. OSMS 92-05, 1992.

[47] CESMD, *Center for Engineering Strong Motion Data*, https://www.strongmotioncenter.org/, 2019.

[48] T. Ancheta, R. Darragh, J. Stewart, *et al.*, "NGA-West2 Database," *Earthquake Spectra*, vol. 30, no. 3, pp. 989–1005, 2014, ISSN: 8755-2930.

[49] H. Haddadi, A. Shakal, C. Stephens, *et al.*, "Center for Engineering Strong-Motion Data (CESMD)," in *Proceedings of the 14th World Conference on Earthquake Engineering, Beijing, October*, 2008, pp. 12–17.

[50] B. Chiou, R. Darragh, N. Gregor, and W. Silva, "NGA project strong-motion database," *Earthquake Spectra*, vol. 24, no. 1, pp. 23–44, 2008, ISSN: 8755-2930.

[51] N. Luco and P. Bazzurro, "Does amplitude scaling of ground motion records result in biased nonlinear structural drift responses?" *Earthquake Engineering and Structural Dynamics*, vol. 36, no. 13, pp. 1813–1835, 2007, ISSN: 0098-8847. DOI: 10.1002/eqe.695.

[52] H. Dávalos and E. Miranda, "Evaluation of the Scaling Factor Bias Influence on the Probability of Collapse Using Sa(T1) as the Intensity Measure," *Earthquake Spectra*, vol. 35, no. 2, pp. 679–702, 2019. DOI: 10.1193/011018eqs007m.

[53] ATC, "Modeling and acceptance criteria for seismic design and analysis of tall buildings," PEER/ATC Report 72-1, 2010.

[54] A. K. Chopra, *Dynamics of Structures: Theory and Applications to Earthquake Engineering*, 5th Edition. Englewood Cliffs, N.J.: Prentice Hall, 2017.

[55] W. P. Fritz, N. P. Jones, and T. Igusa, "Predictive Models for the Median and Variability of Building Period and Damping," *Journal of Structural Engineering*, vol. 135, no. 5, pp. 576–586, 2009. DOI: 10.1061/(ASCE)0733-9445(2009)135:5(576).

[56] N. Hoveidae, "Numerical Investigation of Seismic Response of Hybrid Buckling Restrained Braced Frames," *Periodica Polytechnica. Civil Engineering*, vol. 63, no. 1, pp. 130–140, 2019, ISSN: 05536626. DOI: 10.3311/PPci.12040.

[57] R. Tremblay, M. Lacerte, and C. Christopoulos, "Seismic Response of Multistory Buildings with Self-Centering Energy Dissipative Steel Braces," *Journal of Structural Engineering*, vol. 134, no. 1, pp. 108–120, 2008, ISSN: 0733-9445. DOI: 10.1061/(ASCE)0733-9445(2008)134:1(108).

[58] J. F. Hall, "Problems encountered from the use (or misuse) of Rayleigh damping," *Earthquake Engineering and Structural Dynamics*, vol. 35, no. 5, pp. 525–545, 2006, ISSN: 0098-8847. DOI: 10.1002/eqe.541.

[59] F. Charney, "Unintended Consequences of Modeling Damping in Structures," *Journal of Structural Engineering*, no. 4, pp. 581–592, 2008, ISSN: 0733-9445.

[60] H. M. Hilber, T. J. R. Hughes, and R. L. Taylor, "Improved numerical dissipation for time integration algorithms in structural dynamics," *Earthquake Engineering and Structural Dynamics*, vol. 5, no. 3, pp. 283–292, 1977, ISSN: 0098-8847.

[61] E. Xiong, Z. Yan, T. Li, and L. Yang, "Research on residual drift response of steel frames under strong earthquakes," *Journal of Vibroengineering*, vol. 19, no. 6, pp. 4365–4377, 2017, ISSN: 1392-8716. DOI: 10.21595/jve.2017.18202.

[62] S. Amiri and E. Bojórquez, "Residual displacement ratios of structures under mainshock-aftershock sequences," *Soil Dynamics and Earthquake Engineering*, vol. 121, pp. 179–193, Jun. 2019, ISSN: 0267-7261. DOI: 10.1016/j.soildyn.2019.03.021.

[63] L. Fahnestock, J. Ricles, and R. Sause, "Experimental Evaluation of a Large-Scale Buckling-Restrained Braced Frame," *Journal of Structural Engineering*, vol. 133, no. 9, pp. 1205–1214, 2007, ISSN: 0733-9445.

[64] FEMA, *Recommended Seismic Design Criteria for New Steel Moment-Frame Buildings, FEMA 350*. Washington, D.C.: Federal Emergency Management Agency, 2000.

[65] J. Newell and C.-M. Uang, "Cyclic Behavior of Steel Wide-Flange Columns Subjected to Large Drift," *Journal of Structural Engineering*, vol. 134, no. 8, J. Newell, Ed., pp. 1334–1342, 2008, ISSN: 0733-9445. DOI: 10.1061/(ASCE)0733-9445(2008)134:8(1334).

[66] L. Fahnestock, R. Sause, and J. Ricles, "Seismic Response and Performance of Buckling-Restrained Braced Frames," *Journal of Structural Engineering*, no. 9, pp. 1195–1204, 2007, ISSN: 0733-9445.

[67] D. Vamvatsikos and C. A. Cornell, "Incremental dynamic analysis," *Earthquake Engineering and Structural Dynamics*, vol. 31, no. 3, pp. 491–514, 2002, ISSN: 0098-8847.

[68] D. Vamvatsikos, F. Jalayer, and C. Cornell, "Application of incremental dynamic analysis to an RC-structure," in *Proceedings of the FIB Symposium on Concrete Structures in Seismic Regions*, D. Vamvatsikos, Ed., 2003, pp. 75–86.

[69] J. K. Ousterhout, *Tcl: An Embeddable Command Language*. University of California, Berkeley, Computer Science Division, 1989.

[70] F. McKenna and G. L. Fenves, "Using the OpenSees interpreter on parallel computers," University of California, Berkeley, Berkeley, CA, NEESit Report TN-2007-16, 2008.

[71] A. Liel and H. Tuwair, "A Practical Approach for Assessing Structural Resistance to Earthquake-Induced Collapse," in *Structures Congress 2010: 19th Analysis and Computation Specialty Conference*, 2010, pp. 58–69, ISBN: 0-7844-1131-X. DOI: 10.1061/41131(370)6.

[72] A. Hardyniec and F. Charney, "A new efficient method for determining the collapse margin ratio using parallel computing," *Computers & structures*, vol. 148, pp. 14–25, 2015, ISSN: 0045-7949. DOI: 10.1016/j.compstruc.2014.11.003.

[73] C. G. Lachanas and D. Vamvatsikos, "Rocking incremental dynamic analysis," *Earthquake engineering & structural dynamics*, vol. 51, no. 3, pp. 688–703, 2022, ISSN: 0098-8847. DOI: 10.1002/eqe.3586.